UNIVERSITY OF CALIFORNIA
SANTA CRUZ

The Effects of Sea Level Rise and Extreme Precipitation on Emerging Groundwater and Contaminant Migration

A dissertation submitted in partial satisfaction of the requirements for the degree of

DOCTOR OF PHILOSOPHY

in

EARTH AND PLANETARY SCIENCE

by

James Alan Jacobs

June 2025

The Dissertation of James Alan Jacobs is approved:

Professor Adina Paytan, Chair

Professor Gary Griggs

Professor Kristina Hill

Peter Biehl
Vice Provost and Dean of Graduate Studies

Table of Contents

List of Figures

List of Tables

Abstract

The Effects of Sea Level Rise and Extreme
Precipitation on Emerging Groundwater and Contaminant Migration

By

James Alan Jacobs

Climate change is reshaping coastal hydrology, with sea level rise (SLR) and more frequent extreme weather events intensifying the risk of flooding and shallow groundwater emergence in urbanized lowland regions. In the San Francisco Bay Area, these changes threaten to mobilize subsurface contaminants, many of which remain in place from historic industrial activity, posing renewed risks to environmental health and safety. As aging infrastructure with associated trenches are increasingly exposed to rising groundwater and intensifying storm surges, accurately predicting surface flooding, emerging groundwater, subsurface water dynamics and contaminant transport becomes critical. This dissertation addresses this challenge through an integrated, three-part analysis of hydrologic response, geochemical indicators, and site vulnerability assessment tools tailored to coastal conditions.

The San Francisco Bay Area faces mounting risks from sea level rise, a consequence of climate change that threatens to exacerbate both coastal flooding and the emergence of shallow groundwater. These hydrologic shifts can mobilize legacy contaminants buried in coastal sediments and artificial fill, heightening the potential for human exposure, particularly to volatile organic compounds that pose vapor intrusion and groundwater contamination risks. This dissertation

presents an integrated, three-part investigation into the physical and geochemical processes driving groundwater emergence and contaminant mobilization under sea level rise and extreme climate events, with a focus on practical tools for risk assessment and site prioritization.

In Chapter Two, field monitoring across 16 wells in three representative low-lying communities, Manzanita, Tamalpais Valley, and Atchison Village over Water Year 2023 was used to quantify the response of groundwater levels to highest astronomical tides and atmospheric river events. Results show that sewer trenches and preferential flow paths amplify groundwater rise, particularly in artificial fill and near the coast, underscoring the critical role of subsurface infrastructure in flood dynamics.

Chapter Three explores the geochemical signatures of groundwater, surface water, and emerging water sources using stable isotopes ($\delta^{18}O$, $\delta^{2}H$), major ions, and geochemical ratios. These data were used to distinguish between rainwater, tap water, saltwater, and true groundwater discharge. Mixing models and ternary diagrams showed distinct chemical profiles for water samples influenced by subsurface mobilization processes versus those from surface flooding from marine overtopping or rainwater ponding, enabling a more accurate identification of emerging groundwater.

Building on these physical and chemical insights, Chapter Four introduces a rapid, cost-effective, multi-tiered indexing framework to prioritize contaminated sites vulnerable to climate-driven hydrologic change. The core of the framework is a modified DRASTIC index, which assesses hydrogeologic vulnerability. To capture additional risk factors, three supplemental indices were developed: the Site Characteristics Index, Contaminant Characteristics Index, and Inundation Vulnerability Index. These Supplementary Indices integrate site-specific data on geologic permeability, contaminant mobility, and flood susceptibility. Fourteen sites with volatile organic compound contamination—specifically chlorinated solvents such as trichloroethylene and tetrachloroethylene, and shallow groundwater were evaluated as sea level rise and groundwater rise vulnerability, with index scores standardized using z-score transformation. Bivariate correlations and composite rankings, based on both predefined and data-driven weights, identified sites at highest risk. A strong correlation between the two weighting approaches confirms the strength of the method.

Collectively, the findings of the research demonstrate that groundwater emergence and contaminant transport are intensifying hazards in coastal settings affected by sea level rise. The integrated framework developed in this study provides a scalable, evidence-based tool for prioritizing investigation and mitigation at contaminated sites, supporting proactive climate adaptation and public health protection strategies in vulnerable urban areas.

Together, these chapters provide a unified framework for diagnosing, interpreting, and prioritizing groundwater-related risks in coastal contaminated sites. By combining field-based hydrologic monitoring, geochemical source tracing, and index-based site ranking, this study offers a replicable approach for identifying areas most susceptible to contaminant mobilization under future sea level and climate scenarios. The findings underscore the importance of incorporating subsurface processes into regional adaptation planning and provide a science-based foundation for directing limited resources toward the most at-risk locations. As sea level rise accelerates, these methods offer timely insights to guide sustainable land use, infrastructure resilience, and flood mitigation in vulnerable coastal communities.

Dedication

To Olivia,

Relentlessly challenging my hypotheses

Acknowledgments

I am deeply grateful to Dr. Adina Paytan for her openness in mentoring an unconventional student and for her willingness to guide the direction of this dissertation. I also extend my sincere thanks to the faculty and staff at the University of California, Santa Cruz, for fostering an inclusive and welcoming environment for research and scholarship. My interest in hydrogeology draws from decades of professional field practice, while my engagement with wastewater systems grew through community service, first as a publicly elected board member of a sewer collection agency, and later as a commissioner for a local wastewater treatment plant. This research lies at the intersection of those two passions, investigating how sewer utility trenches influence groundwater response to sea level rise and extreme events.

I thank my dissertation committee, Professors Adina Paytan, Gary Griggs, and Kristina Hill, for their thoughtful feedback, guidance, and support throughout this process. I am also grateful to Professor Andy Fisher, whose questions during my PhD qualifying exam sharpened my understanding of hydrogeologic systems. The students and postdoctoral researchers in the Paytan Biogeochemistry Lab have offered invaluable support during research updates and lab discussions, and I thank them for their collegiality and insight.

The hydrogeologic portion of this research was supported by NOAA California Sea Grant (82606) and the California Ocean Protection Council Proposition 68 Grant (C0875020). Additional fieldwork support was provided by the J. Casey Moore Fund through the Earth and Planetary Sciences Department at UC Santa Cruz and the William Siok Graduate Scholarship from the American

Institute of Professional Geologists. I gratefully acknowledge equipment and analytical services donated by corporate sponsors including Enviro-Tech Services, Solinst Canada Ltd., Precision Enviro-Tech Laboratory, Clearwater Group, and SmartCover. I also thank individual donors Mehmet Pehlivan, Stephen Baker, Ian Eyeington, and William Aley. Thanks go to the technical reviewers of the early chapters, John Karachewski, Tom Mohr, Lida Davar, Stephen Baker, and Olivia Jacobs, for their valuable feedback. I also thank Jacob Aman, who expertly drafted several of the figures.

The Sausalito Marin City Sanitary District (SMCSD) allowed the installation of monitoring wells on their easements, and I am especially grateful to those who permitted monitoring wells or sampling on their private property, including Jeff Hancock, Jimmy Piper, April Post, Kitty Edwinson, Lissa McKee, Kim Rago, Ellis McCauley, Allen Shaff, Estella Gutierrez, and Tanya Conde of the Holiday Inn Express. I am sincerely thankful for the letters of support submitted for my NOAA grant application by Mark Grushayev, General Manager of the Sewerage Agency of Southern Marin; Bob Wiebe, emeritus professor of geology at Franklin & Marshall College; Sarah Calderon, Workforce Development Director at Groundwork Richmond; Lorien Fono, Executive Director of the Bay Area Clean Water Agencies (BACWA); Tara Ayres and Breana George, Board Presidents of the Atchison Village Mutual Homes Corporation; Barbara Postel, Atchison Village volunteer; Janis Hashe, Coordinator of Friends of Richard J. Boyd Park; C. Juliana Gonzalez, Executive Director of The Watershed Project; Cheryl Maier, President of Friends of the Richmond Greenway; Oscar Garcia, President of the Iron Triangle Neighborhood Council; Allan Jensen, President of the Board of

Trustees of the Richmond Friends of Recreation; Heather Abrams, General Manager of the Tamalpais Community Services District; Marin County Supervisor (District 3) Stephanie Moulton-Peters; Tom Leatherman, General Superintendent of Rosie the Riveter/World War II Home Front National Historical Park; and Mayor Tom Butt of the City of Richmond. Special thanks to the volunteers who assisted in the field, including Barbara Postel, Olivia Jacobs, and Kevin Pope. Additional gratitude is due to members of the Paytan Lab for their collaboration.

The geochemistry phase of this research was partially funded by NOAA California Sea Grant (82606). I thank Jonathan Le of Precision Enviro-Tech Laboratory for conducting an extensive set of ion geochemical analyses, as well as Colin Carney and Dyke Andreasen of the UCSC Stable Isotope Lab for their work on water isotopes. Brian Dreyer of the UCSC Institute of Marine Sciences Analytical Lab provided expertise in ICP-OES analyses. I am deeply appreciative of the Paytan Biogeochemistry Lab and the mentorship I received throughout the research process. The portion of the study focused on sea level rise and groundwater-driven contaminant mobilization was supported by the California Ocean Protection Council Proposition 68 Grant (#C0875020), "Characterizing Toxic Waste Sites in the San Francisco Bay Region and Their Exposure to Future Sea Level Rise and Groundwater Flooding." I extend special thanks to Greenaction for Health and Environmental Justice, and to the many local participants whose knowledge and engagement informed this work. I also appreciate the contributions of the State Water Resources Control Board (SWRCB) and the Department of Toxic Substances Control (DTSC), whose staff participated in multiple meetings with the OPC Prop 68 team to discuss the implications of sea level rise and subsurface contamination.

Finally, and most personally, I thank my wife of 41 years, Olivia Jacobs, and our two sons, Ross and Elliott. Your belief in me, especially during moments of doubt, has meant everything. Thank you from the bottom of my heart.

1 Introduction

In coastal urban environments, sea level rise and extreme events are not only increasing surface flood hazards but also driving the upward emergence of groundwater, an underrecognized threat that is often amplified by subsurface preferential flow pathways such as utility trenches and buried infrastructure.

Portions of many American coastal cities, including San Francisco, California; Boston, Massachusetts; New York City, New York; Miami, Florida; Seattle, Washington; New Orleans, Louisiana; and Charleston, South Carolina have been developed on low-lying land that consisted of tidal flats and wetlands (Sweet et al., 2017 and 2022). To accommodate urban expansion, these landscapes were artificially raised using imported fill, often over compressible, clay-rich bay mud. As climate change accelerates sea level rise (SLR) and intensifies extreme weather events, these communities are increasingly vulnerable to a variety of flood hazards, including storm surge, rainfall-driven runoff, and tidal inundation. However, an often overlooked but equally serious threat is the emergence of groundwater, a phenomenon where rising water tables reach or breach the land surface, often in tandem with storm or tidal events.

Emerging groundwater is an underappreciated consequence of sea level rise. Unlike surface flooding, which is more visible and better monitored, groundwater emergence occurs from below and can be difficult to detect without dedicated subsurface observation. Yet it poses major risks to infrastructure, especially in communities underlain by shallow water tables and artificial fill.

Rising groundwater can infiltrate stormwater and wastewater systems, overwhelm sump pumps and basements, and degrade roads, foundations, and utility corridors. Furthermore, groundwater emergence increases the likelihood of mobilizing buried contaminants, legacy pollutants trapped in the vadose zone or shallow saturated zone that may be flushed upward during extreme tides or precipitation events.

Preferential flow pathways (PFPs)—including utility trenches, sewer lines, and storm drains—are increasingly recognized as important amplifiers of these hazards. These subsurface conduits often cut through artificial fill and act as unintentional hydrologic shortcuts, allowing saline water, stormwater, or wastewater to travel laterally and vertically through the subsurface (Anderson et al., 2018; Rotzoll and Fletcher, 2012; Rozell, 2020; Taherkhani et al., 2020). In doing so, they may promote not only groundwater emergence but also the spread of contaminants, increasing the risk of human exposure and environmental degradation.

Coastal flood processes in shoreline communities (Table I.1) span a wide range of time scales and magnitudes. These include high-intensity, short-duration events such as atmospheric rivers (ARs) and highest astronomical tides (HATs), as well as chronic drivers like sea level rise and land subsidence. Groundwater rise—whether temporary or sustained—is increasingly observed as a key component of compound flooding, particularly in urban coastal environments.

The role of PFPs in accelerating groundwater movement and exacerbating flood impacts has been documented across a variety of coastal settings. In the San Francisco Bay region, these pathways are especially important in areas built atop reclaimed wetlands and bay fill. For example, at sites like Manzanita, Tamalpais Valley, and Atchison Village, infrastructure corridors appear to mediate subsurface water movement, influencing both groundwater emergence and contaminant dispersion (e.g., Befus et al., 2020; Hoover et al., 2017; Plane et al., 2019a; Hill et al., 2023). Similarly, case studies from Ontario, Canada demonstrate how PFPs contribute to basement flooding and hydraulic connectivity across urbanized subsurface networks (Senior et al., 2016).

Before widespread development, the San Francisco Bay region supported roughly 1,400 km^2 of freshwater wetlands and 800 km^2 of salt marsh (Atwater et al., 1979). Today, less than 125 km^2 of undiked wetlands remain, reflecting a 95% reduction. Most urban expansion occurred atop Young Bay Mud, a Holocene-aged, organic-rich clay deposit known for low shear strength, high compressibility, and poor drainage (AEG, 2018). These materials create ideal conditions for shallow water tables, limited vertical drainage, and high susceptibility to both flooding and contaminant mobilization.

Although numerous government agencies have published sea level rise projections for the San Francisco Bay Area (e.g., NOAA, USGS, NASA, FEMA), there remains a critical gap in field-based observations that quantify groundwater emergence and subsurface water dynamics at the neighborhood scale. This research focuses on three low-lying communities developed atop fill and bay mud: Manzanita and Tamalpais Valley in Marin County, and Atchison Village in Richmond, Contra Costa County. Manzanita, in particular, is representative of flood-prone transit-oriented development located directly on the shoreline.

This dissertation comprises three integrated projects that collectively investigate how preferential flow pathways influence coastal groundwater dynamics, flood emergence, and contaminant risk:

Project 1 (Chapter 2): Uses data loggers in monitoring wells to quantify groundwater rise during extreme precipitation and tide events. Comparisons are made between wells inside and outside of trenches to determine their amplification role.

Project 2 (Chapter 3): Uses geochemical and isotopic tracers, including stable water isotopes and major ions, to identify the sources of emerging groundwater and to distinguish between end members and mixed water types.

Project 3 (Chapter 4): Develops a groundwater vulnerability and site prioritization tool for contaminated areas at risk of groundwater emergence and SLR-driven mobilization. This tool is informed by field data and developed in collaboration with an OPC Prop 68-funded regional working group of academics, agencies, and community partners.

Together, these projects provide new insight into the underrecognized problem of emerging groundwater, the role of PFPs in amplifying flood and buried contaminant risks, and the implications for infrastructure, public health, and coastal planning. This work aims to inform local-scale adaptation strategies that address both visible surface flooding and the hidden hazards rising from below.

2 Amplified Groundwater Response to Extreme Events in Sewer Trenches in Coastal Artificial Fill and Alluvial Deposits, San Francisco Bay Area, California

Abstract

Rising sea levels and extreme hydrologic events increase groundwater inundation risks for coastal communities in the San Francisco Bay Area. This study analyzed groundwater responses to the highest astronomical tide and to atmospheric river events at three historically flood-prone sites: Manzanita and Tamalpais Valley, built on artificial fill, and Atchison Village, situated on poorly draining alluvial deposits. Data were collected from 16 groundwater monitoring wells at 15-minute intervals during Water Year 2023, recording water level, salinity, and temperature. The dataset captured up to 15 highest tide events (exceeding 2.2 m above mean sea level) and 15 extreme rainfall events (each with over 19.5 cm of precipitation). During highest tides, tidal influence at the coastal site extended 1.5 times farther laterally in trench wells (85 m) than in non-trench wells (57 m). Vertical groundwater rise was also amplified,

with trench wells showing 1.6 times greater response during highest tides and 1.7 times greater response during extreme storms. Inland sites exhibited negligible response (0.00 to 0.01 m) to tidal forcing. To assess regional groundwater emergence risk, this study projected conditions at 30 sites, including 23 with subsurface contamination, based on observed groundwater responses, sea level rise, land subsidence, and extreme storm events. Results indicate a substantial increase in groundwater emergence risk by 2050, particularly in trenches within artificially filled areas of the San Francisco Bay Area.

2.1 Introduction

Coastal communities in the San Francisco Bay Area face increasing risks of groundwater inundation due to rising sea levels and extreme rain events. Sea level rise (SLR) not only leads to marine flooding through overtopping but also causes groundwater to rise, potentially reaching or exceeding the surface. The effect of this phenomenon is greatest during the highest astronomical tide (HAT) events (commonly known as king tides) and extreme rain events linked to atmospheric rivers (AR). Flooding during such events significantly threatens infrastructure, public health, and ecosystems (LAO, 2020; Hill et al., 2023). Groundwater inundation can contribute to compound flooding when SLR coincides with other flood-generating processes, such as AR events, HAT, storm surges, and land subsidence. Marine overtopping is increasingly observed globally; however, other contributing flood factors remain under-measured. The impact of global trends in mean SLR and associated scenarios in the region are well recognized (Hauer et al., 2016; Sweet et al., 2017; Beckley et al., 2021; The

Ocean Protection Council, 2024; Thompson et al., 2024). However, while these assessments comprehensively address spatial and temporal flooding scales, they do not account for seawater-groundwater interactions, an essential driver of coastal flood dynamics. This gap underscores the need for integrated research that encompasses all flood-generating processes to enhance predictive models and inform effective mitigation strategies.

Coastal infrastructure faces mounting challenges from compound flooding impacts, including rising groundwater tables and increased vulnerability to flooding, particularly in areas with artificial fill. SLR contributes to elevated water tables, leading to groundwater flooding and heightened social and ecological vulnerabilities (Rotzoll and Fletcher, 2012). Compound flooding, resulting from a combination of direct marine overtopping, stormwater backflow, and groundwater emergence, poses significant public health risks through sanitary sewer and septic system overflows (Habel et al., 2017, 2019). Long-term SLR projections forecast cumulative impacts on septic and sewer systems (Habel et al., 2024).

Research indicates that integrating multiple flood drivers, such as SLR, storm surges, and tidal effects, nearly doubles the estimated land at risk compared to models that consider only flooding due to seawater overtopping (Anderson et al., 2018). Urban stormwater systems are increasingly vulnerable to groundwater rise during extreme weather events (Rozell, 2020), emphasizing the need to incorporate groundwater inundation into coastal resilience planning (Rozell, 2021). Specifically, flood risks are exacerbated through storm surges and rising groundwater, highlighting the necessity for integrated mitigation strategies

(Taherkhani et al., 2020).

Rising groundwater during extreme events reduces sewage system capacity, leading to sanitary sewer overflows and infrastructure damage (Hoover et al., 2017; Plane et al., 2019). Areas with perched groundwater zones face additional risks, including trench infiltration, foundation destabilization, mobilization of buried hazardous contaminants, and increased surface water accumulation (Befus et al., 2019). Low-lying regions on artificial fill are particularly at risk, experiencing groundwater inundation even before coastal defenses are overtopped (May et al., 2020, 2022).

The complexity of compound flooding (**Figure 2.1**) arises when multiple flood drivers converge, amplifying risks. In the San Francisco Bay area, seawater-groundwater interactions are particularly pronounced in regions with artificial fill and poorly draining alluvial sediments, exacerbating flood hazards, infrastructure vulnerabilities, saltwater intrusion, and groundwater inundation (CCSF, 2016; Jiao and Post, 2019; USACE, 2024; Wang et al., 2025). Many of the current flooding challenges, including lowland flooding, groundwater emergence, and land subsidence, can be traced back to the historical development practices in the San Francisco Bay area. Before 1850, the San Francisco Bay Area contained approximately 1,400 km^2 of freshwater wetlands and 800 km^2 of salt marshes (**Figure 2.2a** and **2.2b**). Today, only about 125 km^2 of undiked wetlands remain, representing a 95% loss of critical tidal and freshwater ecosystems (Atwater et al., 1977; 1979). The composition and extent of artificial fill and underlying native sediments in the region have been described by Trask and Rolston (1951), Hitchcock et al. (2008), and AEG (2018). Artificial fill exhibits

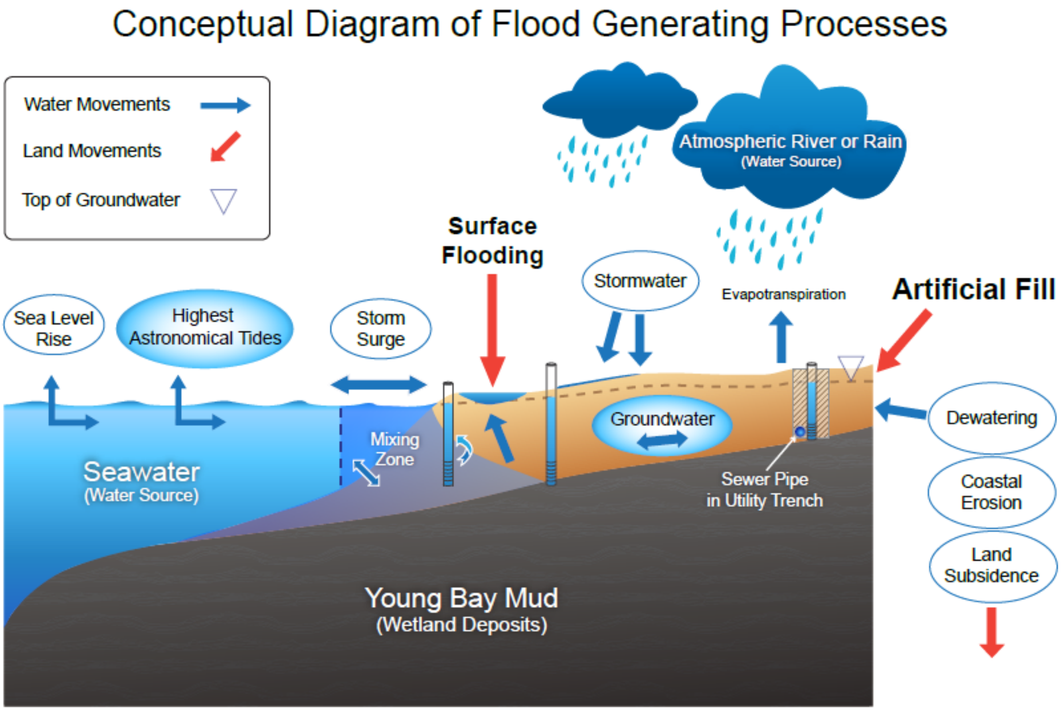

Figure 2.1: Generalized conceptual diagram, not to scale, showing water sources and flood generating processes contributing to coastal flooding and groundwater rise.

highly variable hydraulic conductivity: coarse-grained materials such as sand and gravel allow rapid groundwater flow, whereas fine-grained clays and silts act as aquitards, impeding vertical and lateral flow (Heath, 1983; 2004).

The economic impact of SLR and storm surge protection along the San Francisco Bay shoreline is projected to range from $81 billion to $147 billion by 2050, with potential costs of inaction exceeding $230 billion (BCDC, 2023). Effective adaptation strategies require detailed groundwater data to support hydrogeologic and engineering assessments, informing sustainable resilience planning (SFEI, 2019; Hummell et al., 2020). Groundwater inundation poses risks to infrastructure by degrading structural components and creating zones of variable permeability. Trenches and subsurface structures can enhance vertical and lateral water movement, increasing the risk of groundwater emergence and hazardous and toxic contaminant migration (Hill et al., 2023). In poorly drained areas, including wetlands and mudflats, Preferential Flow Pathways (PFPs) including roadway base course, trenches, French drains, leaky pipelines and storm drains (**Table 2.1**) can facilitate significant water movement, potentially raising public health risks from exposure to buried hazardous and toxic contamination and sanitary sewer overflows.

This study addresses the hidden threat of groundwater inundation (also termed groundwater emergence or flooding) in coastal urban areas, particularly in regions built on artificial fill or poorly drained alluvial deposits by monitoring groundwater responses to HAT and AR events. This information could be incorporated into predictive models and supports the development of adaptive infrastructure strategies and informs public health protections, ultimately advancing comprehensive flood mitigation and coastal management efforts.

Table 2.1: Structural and Environmental Features Acting as Preferential Flow Pathways (PFPs) in Artificial Fill and Shallow Subsurface Deposits

PFP Type	Feature Descriptions
Utility Trenches	Trenches containing water, sewer, and stormwater pipes; electrical and communication conduits; gas and oil pipelines; often lined with bedding gravel or sand that enhances flow. Includes access points such as manholes and pump stations.
Building Structural Foundations	Footings, slabs, pile foundations, retaining walls, and foundation drains that can channel water vertically or laterally; may include fill settlement zones around the structure.
Drainage Systems	French drains, curtain drains, infiltration trenches, and subdrainage pipes; designed to collect and redirect shallow groundwater or stormwater, often with permeable gravel backfill.
Stormdrains and Culverts	Stormwater infrastructure including street catch basins, manholes, culverts beneath roads or railways, and outfalls; typically connected to other utility corridors.
Landscaping Features	Irrigation lines, planter boxes, bioswales, permeable pavements, gravel-filled trenches, and paver systems that allow infiltration and concentrated subsurface flow.
Excavations and Pits	Construction excavation sites, borrow pits, soil stockpiles, or partially backfilled areas; can act as depressions or conduits for infiltration and perched water.
Underground Storage Tanks and Vaults	Fuel or chemical tanks, utility vaults, containment structures; leaks or surrounding gravel backfill can create vertical preferential flow zones.
Transportation Infrastructure	Road embankments, railway beds, bridge footings, and aggregate road bases (e.g., Class II base rock); highly permeable zones often connected to culverts or drains.
Soil Heterogeneity and Voids	Variability in artificial fill composition (e.g., lenses of sand, gravel, rubble, bricks, concrete debris); loosely compacted zones or organic-rich fill that form conduits.
Natural Geologic Features	Buried stream channels, paleochannels, native soil inclusions, and fault zones that intersect artificial fill layers; may be reactivated by infiltration or rising groundwater.
Vegetation Root Channels	Root systems of trees, shrubs, or grasses that have died or decayed, creating macropores; can persist long after vegetation removal.
Cracks and Fissures in Fill Material	Desiccation cracks in clayey fill, settlement-induced fissures, subsidence cracks, or shrink–swell fractures that provide rapid vertical flow paths.
Abandoned or Buried Structures	Demolished building foundations, buried utility lines, fill voids containing construction debris or waste; poorly documented in historical records, often heterogeneous.
Animal Burrows	Gopher tunnels, ground squirrel burrows, and other small mammal activity that can create interconnected voids through fill layers.
Buried or Abandoned Remediation Systems	Gravel backfill from past soil excavations, sealed or improperly abandoned monitoring and extraction wells, old slurry walls, and defunct underground storage or conveyance infrastructure.

2.2 Materials and Methods

2.2.1 Study Areas

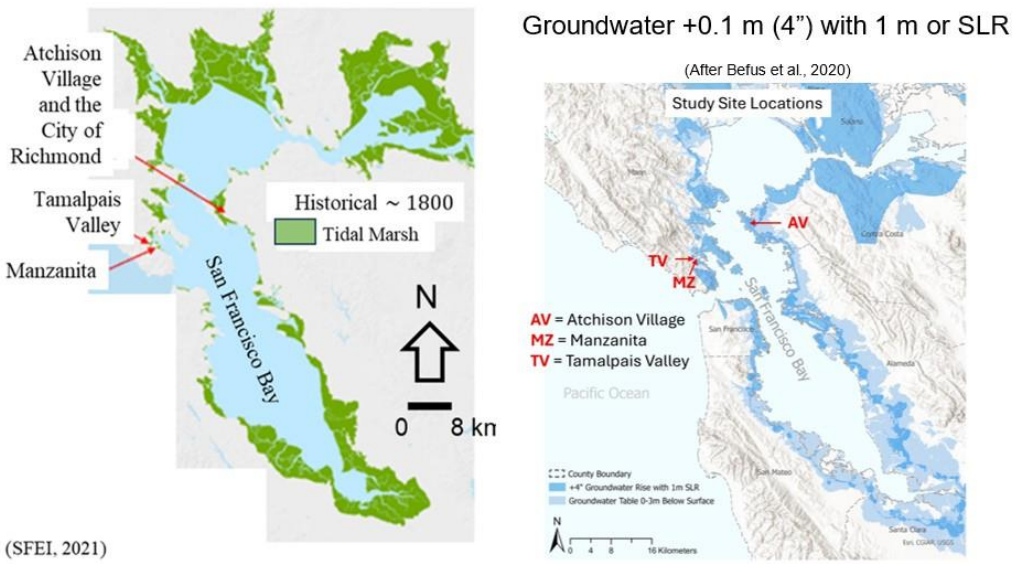

a b

Figure 2.2: a) Historic wetland deposits circa 1800s (modified after SFEI,2021) and b) Study site locations and map of groundwater rise (+0.1 m with 1 m of SLR) (modified after Hill et al., 2023 (basemap), based on database by Befus et al., 2020)

Study sites were selected to represent a range of coastal groundwater conditions typical of the San Francisco Bay Area. Manzanita, located in an unincorporated area of southern Marin County along Richardson Bay, is a low-lying coastal zone developed on artificial fill overlying former wetlands. This fill is primarily composed of clay (CL) and contains a perched groundwater zone above the underlying Young Bay Mud (GEI, 2015). The Young Bay Mud in this region is a plastic clay (CH) that typically acts as a low-permeability aquitard, impeding vertical groundwater flow (GEI, 2015). These subsurface conditions were confirmed in this study through seven soil borings (MW1–MW7), which revealed artificial fill ranging from 2.20 to 3.02 m thick and consisting of predominantly of clay (CL), with smaller amounts of sand, gravel, and construction debris (e.g., brick fragments).

During storm events, precipitation infiltrates through the artificial fill but is often obstructed by the underlying Young Bay Mud, resulting in surface emergence and flooding, particularly in low-lying areas. At Manzanita's coastal margin, flooding is driven by a combination of marine overtopping, stormwater backflow, and groundwater emergence (**Figure 2.3a–f**). These flood risks are further exacerbated by shoreline erosion, tidal pumping, and land subsidence.

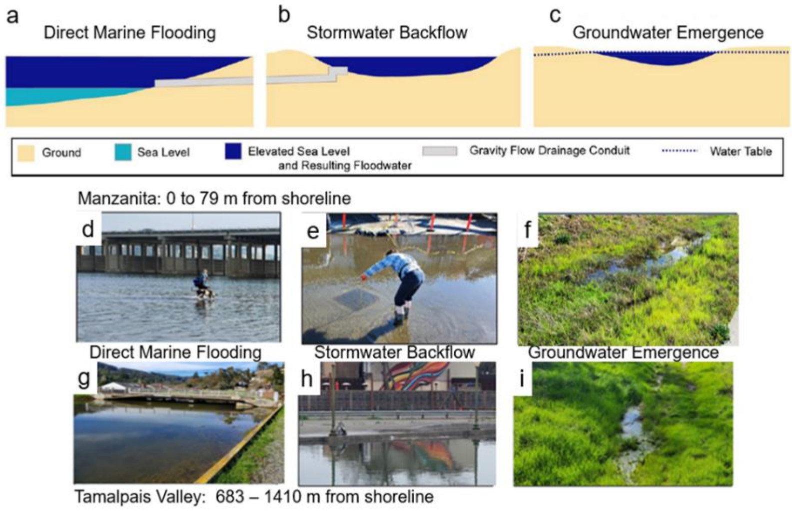

Figure 2.3: a-c) Flooding mechanisms: conceptual diagram and d) Manzanita – direct marine flooding e) stormwater backflow f) groundwater emergence; g) Tamalpais Valley at flood stage h) stormwater backflow along Coyote Creek i) emerging groundwater. Photos by J. Jacobs and O. Jacobs; diagram modified after Habel et al. (2019, 2020).

Tamalpais Valley, located in the unincorporated area of Marin County adjacent to Manzanita and upstream of Richardson Bay, shares similar geologic conditions (**Figures 2.3g-i**), with artificial fill overlying Young Bay Mud (GEI, 2015). Borings at Tamalpais Valley (TVW1-TVW4) had fill depths between 2.08 and 2.29 m (this study) while soil descriptions are like Manzanita for the artificial fill and Young Bay Mud. While engineered levees along Coyote Creek offer current surface flood protection, they do not mitigate stormwater backflow (**Figure 2.3h**) or groundwater rise (**Figure 2.3i**).

Atchison Village, located in the City of Richmond, Contra Costa County, extends from the Santa Fe Channel to an inland residential community. The site exhibits a transition in subsurface materials, from artificial fill near the channel, composed of sand, clay, and construction debris overlying low-permeability wetland deposits, to poorly draining alluvial sediments derived from the East Bay Hills further inland (Figuers, 1998). This stratigraphic variability, combined with the presence of low permeability soils, contributes to increased groundwater flooding risk. In particular, the interaction between artificial fill and poorly draining native sediments creates conditions where water accumulates and persists near the surface, increasing the likelihood of groundwater rise and emergence during AR events (Figuers, 1998). All three study areas have shallow water tables (0-1.5 m below ground surface), and sump pump dewatering is common.

2.2.2 Wells Installation and Groundwater Monitoring

This study used a network of 16 groundwater monitoring wells across three study areas, Manzanita (MZ) (**Figure 2.**), Tamalpais Valley (TV) (**Figure 2.4b**), and Atchison Village (AV) (**Figure 2.4c**), to evaluate groundwater responses to extreme events such as HAT and AR. The installations, completed between September and November 2022, followed a comprehensive optimization framework that prioritized hydrogeologic variability, proximity to trenches, shoreline distance, and surface elevation. Well placement was guided by the Coverage Maximum Index (CovMaxI), which prioritized proximity to shorelines, distance to trenches, surface elevation, and accessibility. This approach ensured the selection of high-priority sites, optimizing spatial coverage and redundancy while managing costs. In Manzanita, wells were placed based on predefined optimization criteria. Tamalpais Valley wells were limited to non-Preferential Flow Pathway (non-PFP) locations due to site access constraints. Atchison Village used three pre-existing irrigation wells and added two new wells: one within a sewer trench (PFP) and another near an existing irrigation well to validate shallow groundwater conditions. All PFP wells in the study are located within 1.1 m of the sewer pipe centerline. Non-PFP wells are positioned at least 4.3 m from the sewer pipe centerline in Manzanita, 3.9 m in Tamalpais Valley, and 10.0 m in Atchison Village.

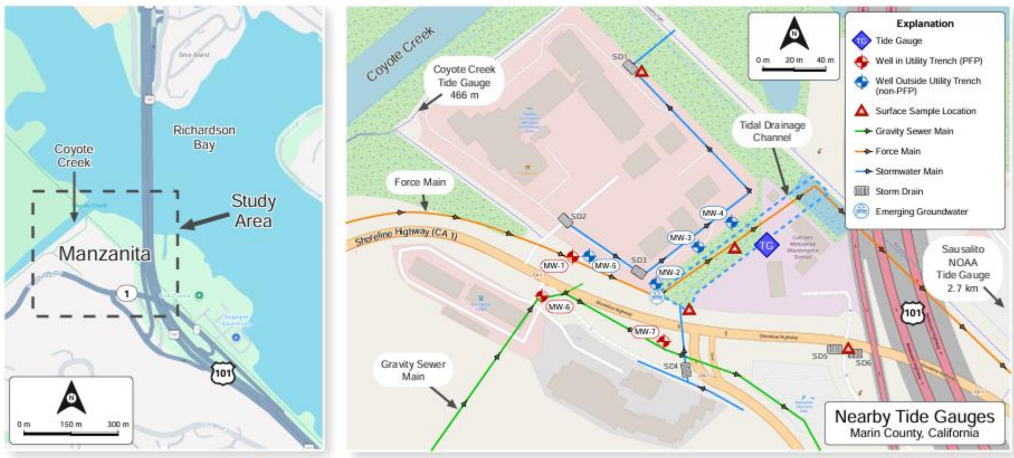

Figure 2.4a: Manzanita site

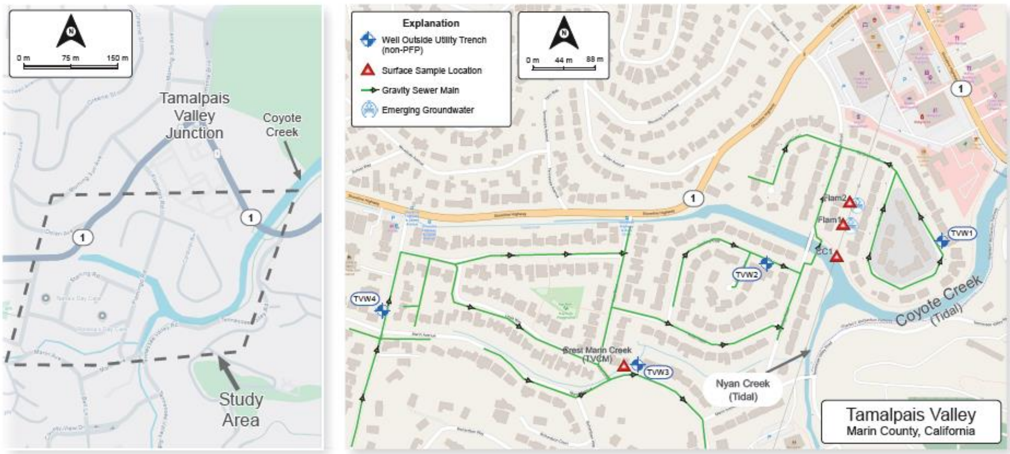

Figure 2.4b: Tamalpais Valley site

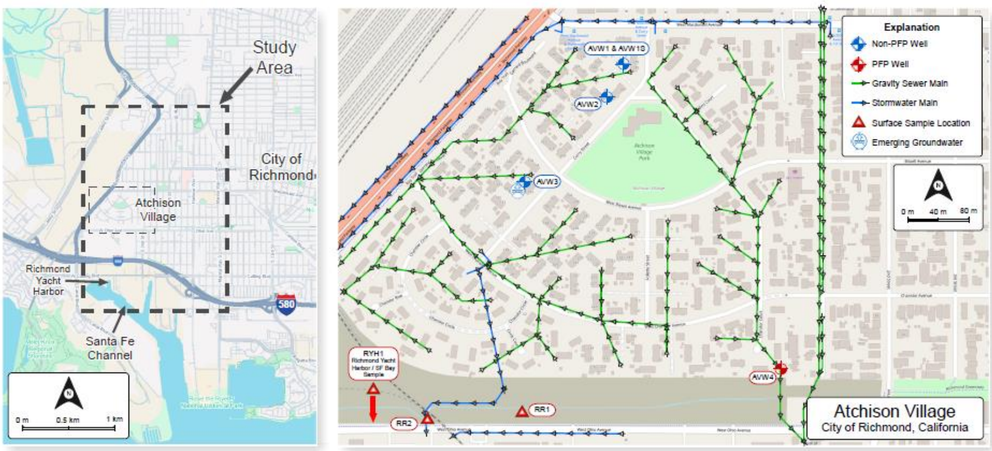

Figure 2.4c: City of Richmond, Atchison Village site

Figure 2.4: Location and well location maps for the three study sites
a) Manzanita site location map (left) and well location map (right)
b) Tamalpais Valley site location map (left) and well location map (right);
c) Map of a portion of the City of Richmond study area which extends from Santa Fe Channel to Atchison Village (left), and Atchison Village well location map (right)

Twelve wells were installed using direct push technology, which allowed for continuous coring to characterize subsurface lithology. These wells were constructed using 2.5-cm diameter PVC casing with 0.5-mm slotted screens, surrounded by 2/12 filter pack sand and sealed with bentonite and neat cement. To prevent damage to sewer pipes, hand-augering was used for three PFP wells (MW6, MW7, and AVW4). Additionally, MW1, a PFP well, was installed using a vacuum truck with an air knife, creating a 10-cm diameter well at a depth of 1.8 m, consistent with the trench depth. All wells were sealed with watertight expanding well plugs and housed in traffic-rated well boxes equipped with O-rings to ensure a watertight seal. A licensed surveyor recorded the elevation and location of each well to a precision of ±3 mm.

A cross-section in Manzanita (**Figure 2.5**), perpendicular to the force main sewer trench and spanning wells MW1 and MW5, illustrates the placement of PFP and non-PFP wells. The Manzanita optimized monitoring network captured variations in surface elevation, shoreline distance, and proximity to trenches, enabling the assessment of groundwater responses to extreme events and providing essential guidance for coastal resilience planning.

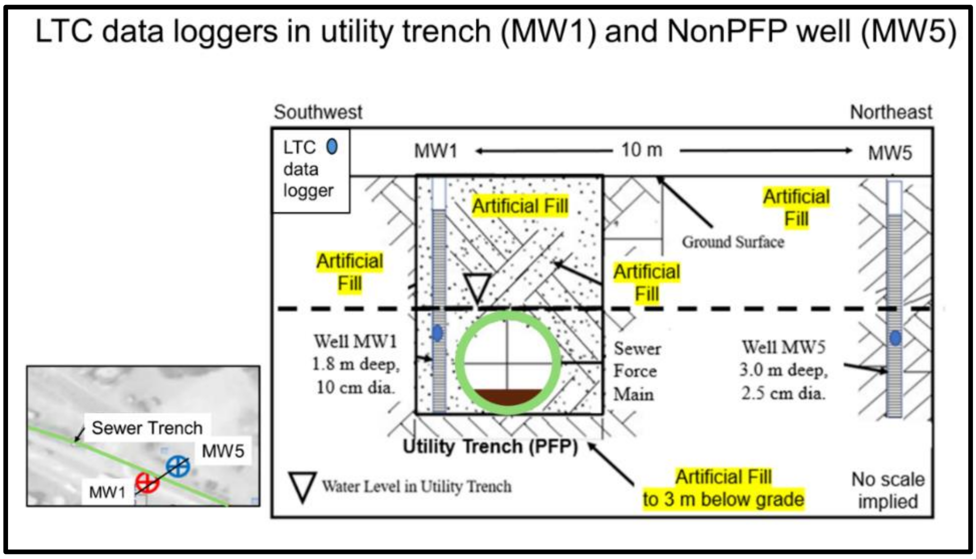

Figure 2.5: Manzanita cross section location map (left) and cross section through MW1 within a force main sewer utility trench and MW5, 10 m away.

Groundwater dynamics were monitored using Solinst Leveloggers (M5 to M30

LTC and LT models). The instruments measured groundwater levels, temperature, and electrical conductivity every 15 minutes with a water level sensor accuracy ranging from ±0.3 cm to ±1.5 cm.

Data collection spanned Water Year 2023, capturing responses to 15 HAT events with tide levels above 2.2 m mean sea level and 15 AR storms producing over 19.5cm of precipitation per event. Groundwater levels, tidal heights, and rainfall data were synchronized to enable detailed spatial and temporal analyses.

2.2.3 Tide and Meteorological Monitoring

Tide and meteorological monitoring were implemented to identify and analyze HAT and AR events across the study sites. For HAT monitoring at Manzanita and Tamalpais Valley a local tide gauge was installed in the Manzanita tidal drainage channel, with the County of Marin Coyote Creek (gauge #38023; located 466 m west of Manzanita and 291 m northeast of Tamalpais Valley) serving as a backup. For Atchison Village, tidal data were obtained from the NOAA tide gauge at the Chevron Pier (Gauge #9414863), situated 2.30 km southwest of Atchison Village. AR impacts were assessed using meteorological data, including precipitation, wind, and surface temperature, from two weather stations. The Almonte Station (KCAMILLV104; 34 m above mean sea level [AMSL]), provided local precipitation and weather data and is located 770 m northwest of Manzanita and 694 m north of Tamalpais Valley. Weather data were collected from the Marina Bay Station (IRIS-KCARICHM131; Elevation 0 m AMSL), situated 2.87 km southeast of Atchison Village. These monitoring networks ensured accurate event identification and comprehensive hydrological analysis across the three study areas.

2.2.4 Highest Astronomical Tide Events

Tide data from the Sausalito gauge (for the Manzanita and Tamalpais Valley areas) and the Chevron Richmond gauge (for the Santa Fe-Atchison Village area) were analyzed. A total of 15 HAT events exceeding 2.2 m above mean sea level for Water Year 2023 (WY2023), spanning from October 1, 2022, to September 30, 2023, were identified using NOAA tide gauge predictions (2024a and 2024b) (labeled 23HAT001 to 23HAT015). For each event, local tide gauge data were used to record the event's start, peak, and end times ($Tide_{start}$, $Tide_{peak}$, and $Tide_{end}$), while groundwater levels at the 16 wells were recorded at corresponding times (GW_{start}, GW_{peak}, and GW_{end}). Key factors such as proximity to the shoreline and trenches were included in the analysis.

2.2.5 Atmospheric River Events

AR events during WY2023 were identified using the Center for Western Weather and Water Resources (CWWWR) database from the Scripps Institution of Oceanography. This database recorded 15 AR events affecting northern California, with intensities ranging from categories 2 to 4 on the Ralph/CWWWR AR scale (1 to 5, with 5 being the highest intensity). These events (labeled 23AR001 to 23AR015) were matched with precipitation data from local weather stations equipped with rain gauges, which recorded the rainfall event parameters ($Rain_{start}$, $Rain_{peak}$, and $Rain_{end}$). Groundwater responses were analyzed by tracking changes in groundwater levels at wells during the corresponding precipitation events.

2.2.6 Hydrologic Data Analysis

Hydrologic signatures recorded by data loggers were analyzed to characterize groundwater dynamics during HAT and AR events. Event start times, peaks, and endpoints were compared to tide (**Figure 2.6a**) and precipitation (**Figure 2.6b**) data to establish correlations with groundwater response (**Figure 2.6c**). Field data were periodically downloaded and cross-referenced with local tide gauge and weather station records to ensure accuracy. Linear regression analysis was performed separately for each of the three study sites and further categorized by PFP and non-PFP data to account for site-specific and sewer-trench proximity-related differences. Groundwater response variability was quantified by calculating the average, minimum, maximum, and standard deviation across events. Independent variables considered in the analysis included geologic substrate (alluvial deposits or artificial fill), distance to the shoreline, proximity to trenches, surface elevation, and event type (HAT or AR). This approach enabled a comprehensive evaluation of groundwater responses to tidal and precipitation forcing, highlighting the influence of shoreline proximity, subsurface materials, and PFPs on groundwater response.

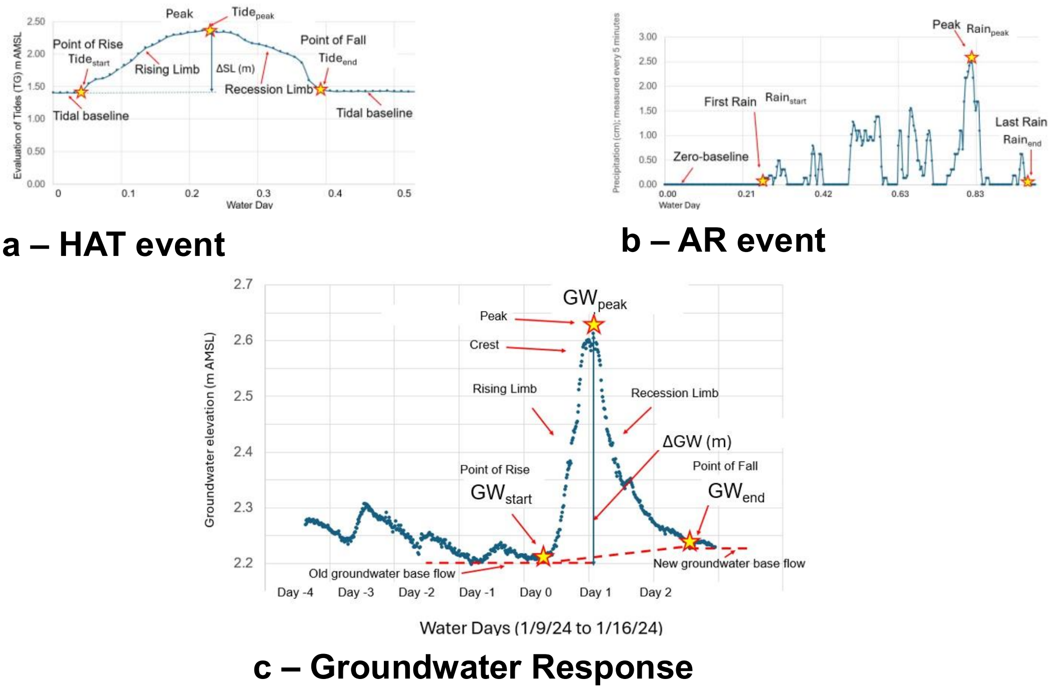

Figure 2.6: a) Method of measuring HAT events, 12/27/23; maximum 2.38 m above mean sea level. b) Method of measuring AR events; example from 1/13/24, 6.1 cm cumulative rain. c) Method of measuring groundwater response; example from MW1, Manzanita to AR event on 1/13/24.

Multivariate regression (**Equation 2.1**) was performed separately for each study site and further divided into PFP and non-PFP data. This approach accounted for site-specific characteristics and sewer-trench proximity differences, providing a more precise understanding of the factors influencing groundwater responses.

$$y = \beta_0 + \beta_1 x_1 + \beta_2 x_2 + \beta_3 x_3 + \beta_4 x_4 + \beta_5 x_5 \qquad (2.1)$$

Where, y is the predicted groundwater response, β_0 is intercept, baseline when all x_i are zero.

$\beta_1 x_1$, $\beta_2 x_2$ . . . $\beta_5 x_5$ are the five independent variables [(in order, precipitation (m), surface elevation (m above mean sea level), distance to shoreline (m), distance to sewer (m), and tide level (m above mean sea level)] times the coefficients, reflecting the influence, impacts or effects of the independent variables.

Adjusted R^2 was used in multivariate regression analysis to account for multiple predictors, as it penalizes the addition of variables that don't substantially improve model fit, providing a more conservative estimate of model performance compared to regular R^2. Adjusted R^2 is calculated by adjusting the R^2 value based on the number of predictors in the model using the formula (**Equation 2.2**):

$$\text{Adjusted } R^2 = 1 - [(1 - R^2)\,(n-1)/(n-k-1)] \tag{2.2}$$

Where, n is the sample size (number of measurements), k is number of predictors.

2.2.7 Machine Learning Analysis of Groundwater Response

Principal Component Analysis (PCA), an unsupervised machine learning method, was used to identify the dominant variables influencing groundwater responses across five independent variables: precipitation (m), tidal level (m), distance to the shoreline (m), proximity to trench (m), and surface elevation (m AMSL). A random forest model captured complex, non-linear relationships between hydrologic drivers, precipitation, tidal level, distance to shoreline, proximity to trenches, and surface elevation, and observed groundwater level changes. This approach was used to generate synthetic groundwater response scenarios in locations like Tamalpais Valley, where PFP wells were not available due to access constraints, allowing for more complete vulnerability assessments under SLR and extreme event conditions.

2.3 Results

2.3.1 Groundwater Dynamics During Extreme Events

Emerging groundwater was observed at all three sites from about March to May 2023 due to elevated groundwater levels following AR events. In Manzanita, groundwater surfaced at a topographic low above a trench. In Tamalpais Valley, emergence was observed at two locations, 79 m and 107 m from Coyote Creek. In Atchison Village, groundwater appeared in sump pump gravel pack and crawl spaces beneath residences. By September 2023, groundwater levels had declined, and no further surface emergence was observed.

Only Atchison Village and Manzanita contained both PFP and non-PFP wells, so comparative averages and amplification ratios for AR events were calculated using data from these two sites. In contrast, groundwater response to HAT events was observed only in Manzanita, where wells are located near the shoreline. Wells in Tamalpais Valley and Atchison Village exhibited negligible response to HAT events (0.00 to 0.01 m). Therefore, only Manzanita wells were used to evaluate groundwater response to HAT events.

Using data from Manzanita and Atchison Village, the average groundwater response to AR events (Figure 7a) was 1.7 times greater in wells located within trenches compared to those farther away. For HAT events, Manzanita exhibited an amplification factor of 1.6 in groundwater response for trench (PFP) wells relative to non-PFP wells. Among non-PFP wells, those in Atchison Village showed slightly higher groundwater responses to AR events than those in

Manzanita and Tamalpais Valley. Overall, PFP wells at both Manzanita and Atchison Village demonstrated greater average groundwater responses than non-PFP wells.

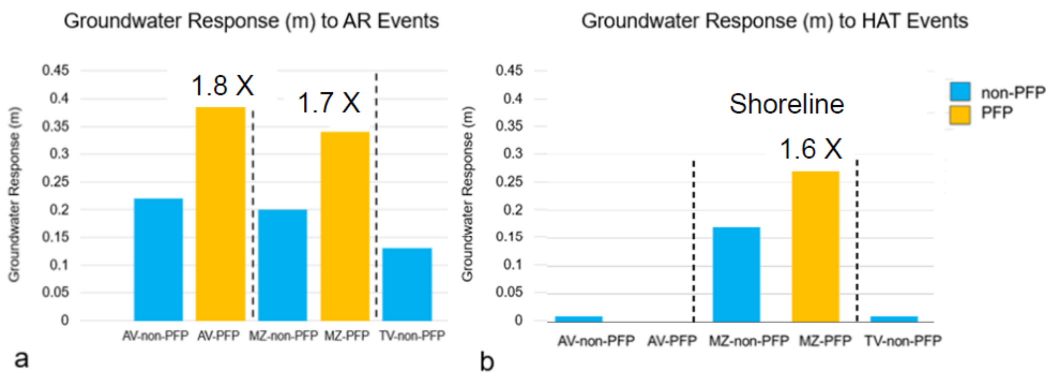

Figure 2.7: a) The chart shows groundwater responses (m) to AR events by study area and well type. b) presents groundwater responses (m) to HAT events by area and well type. Study sites include Atchison Village (AV), Manzanita (MZ), and Tamalpais Valley (TV). Well types are categorized as PFP and non-PFP wells. The values above the PFP bars indicate the amplification factor of groundwater response relative to non-PFP wells at each site.

Average groundwater response in Manzanita during HAT events decreases with increasing distance from the shoreline in both PFP and non-PFP wells (**Figure 2.8**). For HAT events, the multivariate regression analysis, a combined model including shoreline distance, elevation, and proximity to trenches explains 82.1% of the variance in groundwater response (adjusted R^2 = 0.8210, unadjusted R^2 = 0.8253).

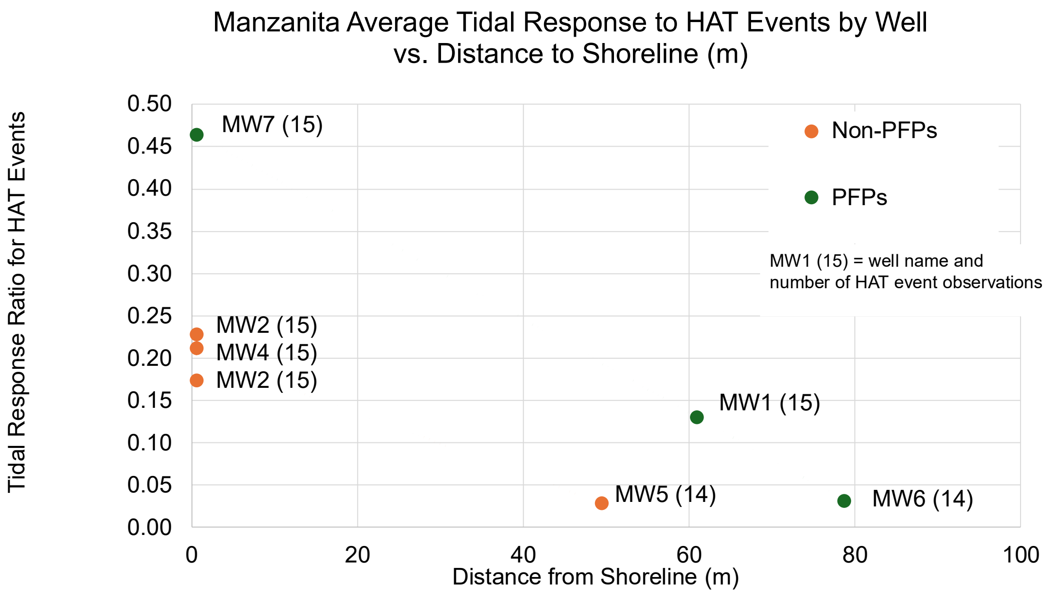

Figure 2.8: Average groundwater response to HAT events vs. distance from shoreline. The numbers in parenthesis are the number of measurements for each well.

For AR events, multivariate regression model performance is highest in AV-PFP wells ($R^2 = 0.912$) and decreases progressively from Manzanita PFP and non-PFP wells to TV-non-PFP wells ($R^2 = 0.678$). Distance to shoreline coefficients ranged from -0.234 to -0.334 ($p < 0.05$). Tidal influence coefficients for TV-non-PFP areas ($\beta = 0.098$; $p > 0.05$). All regression models show strong overall significance (F-stat $p < 0.001$).

2.3.2 Random Forest Model

Because no trench wells were installed in Tamalpais Valley, a Random Forest model was used to generate synthetic groundwater responses under PFP conditions, based on observed patterns from other sites. The model was trained using 222 groundwater level observations drawn from a total of 390 measurements across the three study sites. Input variables included precipitation, tide level, surface elevation, distance to shoreline, proximity to sewer trenches, and event type (HAT or AR). The training dataset included 186 HAT events (93 PFP and 93 non-PFP) and 32 AR events (16 PFP and 16 non-PFP).

Out-of-bag (OOB) error estimates were used for internal validation, yielding an R^2 of 0.82 and a root mean squared error (RMSE) of 0.046 meters. These metrics indicate strong model performance and support the reliability of synthetic predictions. Based on the trained model, 50 synthetic groundwater response predictions were generated for Tamalpais Valley PFP wells, including 5 AR-PFP and 45 HAT-PFP simulations. The predicted average groundwater rise during HAT events in Tamalpais Valley PFP wells was 0.24 meters, closely matching the 0.27 meters observed at Manzanita, suggesting the predictions are both reasonable and field-consistent (**Figure 2.9**).

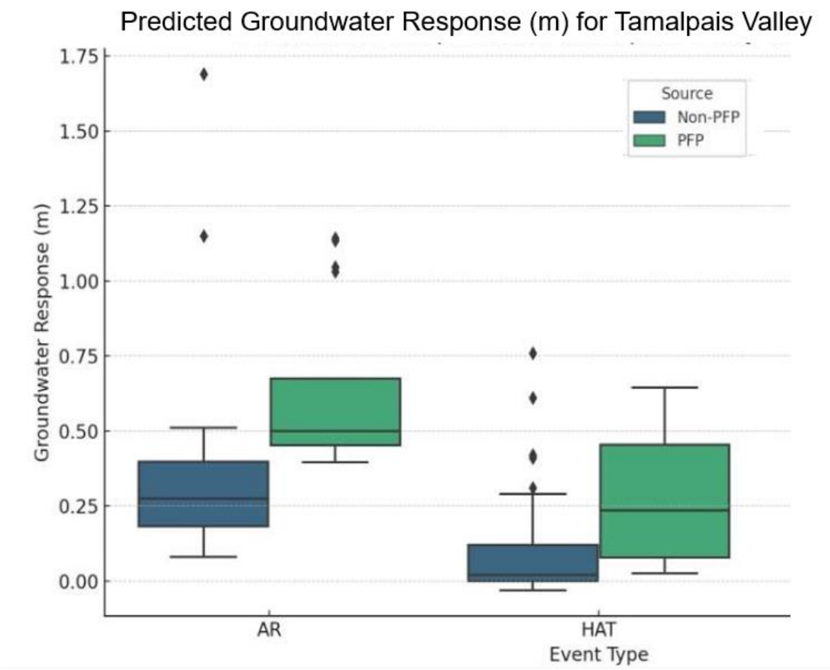

Figure 2.9: Predicted groundwater response (m) for synthetic Tamalpais Valley HAT and AR events

Model performance was evaluated separately for HAT and AR events. For HAT events, the model explained 41% of the variance (R^2 = 0.41). Feature importance values showed that distance to shoreline (34.01%), tide level (22.56%), and precipitation (22.08%) were the most influential variables, followed by proximity to trenches (14.25%) and surface elevation (7.11%) (**Figure 2.10a**). For AR events, model performance was poor, yielding a negative R^2 value of -0.72 and an MSE of 0.41. Precipitation (39.66%) and tide level (37.62%) were the dominant factors, while surface elevation (10.23%), proximity to trenches (8.44%), and distance to shoreline (4.05%) had lower relative importance (**Figure 2.10b**).

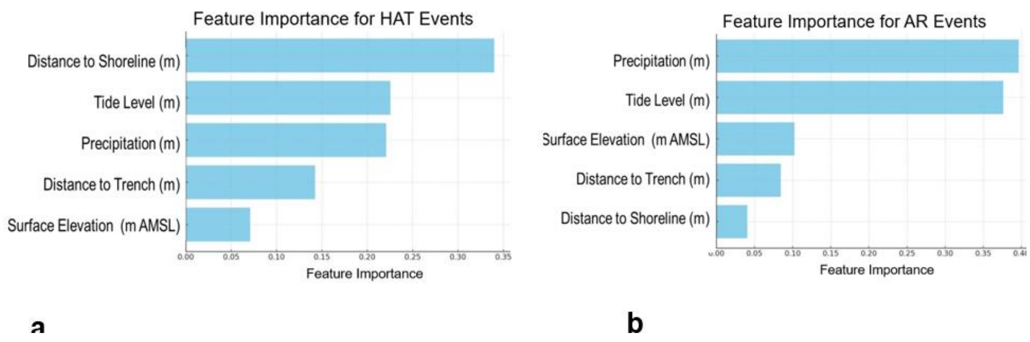

Figure 2.10: a) Feature importance in random forest models for HAT events. b) Feature importance in random forest models for AR events

2.4 Discussion

This study reveals how sewer trenches and associated buried infrastructure in artificial fill and poorly draining alluvial deposits significantly amplify groundwater response to extreme hydrologic events in the San Francisco Bay Area. Across 16 monitoring wells in Manzanita, Tamalpais Valley, and Atchison Village, groundwater levels rose significantly more in wells located near sewer trenches during both AR and HAT events, compared to wells situated farther from trenches. These findings provide strong empirical evidence that infrastructure corridors in artificial fill, function as PFPs, facilitating the lateral propagation of tidal and recharge pressures and accelerating groundwater rise.

During HAT events, groundwater amplification was limited to within 85 meters of the shoreline in trench wells and 57 meters in non-trench wells, with Manzanita trench wells exhibiting a 1.6-times greater rise than more distant wells. During AR events, amplification in trench wells remained substantial, with PFP wells in Manzanita and Atchison Village responding on average 1.7 times more than non-trench wells. These elevated responses in trench-associated wells suggest that sewer trenches and similar subsurface infrastructure enhance both vertical and lateral transmission of hydraulic pressure, consistent with previous studies documenting rapid groundwater response in gravel-lined or backfilled corridors (Habel et al., 2017; May et al., 2022).

In Manzanita, a perched groundwater zone overlying the underlying clay contributed to rapid and emergent groundwater responses, particularly above trench infrastructure. In Tamalpais Valley and Atchison Village, which are located farther inland and less directly exposed to tidal forcing, groundwater showed negligible response to tidal fluctuations. In contrast, Atchison Village exhibited pronounced groundwater rise driven primarily by AR-related recharge.

These site-specific responses reflect broader principles governing groundwater behavior in coastal fill zones. Artificial fill, often comprising heterogeneous mixtures of clay, sand, gravel, and construction debris, presents highly variable hydraulic conductivities that govern infiltration and flow dynamics (Heath, 1983; Hitchcock et al., 2008). Excavated and disturbed trench backfill, whether permeable or not, can act as a PFP within artificial fill. This alters local hydraulic gradients and promotes shallow groundwater accumulation above underlying clay, particularly during heavy rainfall or tidal events.

Multivariate regression analysis demonstrated that shoreline distance, surface elevation, and trench proximity were statistically significant predictors of groundwater rise. A combined model incorporating these spatial variables explained 82.1% of the variance in groundwater response to HAT events, underscoring the central role of both event-based and static site conditions. For AR events, model performance was strongest at Atchison Village PFP wells (R^2 = 0.912), where storm-driven recharge was tightly coupled with infrastructure alignment. These statistical models were further supported by PCA, which showed clear separation between dynamic hydrologic variables (precipitation and tide level) and passive spatial characteristics like elevation, shoreline distance, and trench proximity, suggesting that both sets of factors must be integrated to accurately predict groundwater emergence under future conditions.

The random forest model confirmed that distance to shoreline, tide level, and precipitation were the strongest predictors of groundwater rise during HAT events. Although performance declined for AR events, likely due to complex infiltration and recharge dynamics, trench proximity remained a key variable. These results demonstrate that linear infrastructure influences subsurface flow during both tidal and storm-driven events.

Much of the Bay Area shoreline, from Richmond to San Mateo, is built on artificial fill over former tidal wetlands, with shallow groundwater, low elevation, and dense underground infrastructure. As sea levels rise and AR events intensify, these areas may experience groundwater flooding before marine overtopping occurs. Trench-aligned infrastructure may also facilitate inland salinity intrusion, mobilize subsurface contaminants, and increase pressure in sewer systems, raising the risk of overflows and exposure to hazardous materials (Habel et al., 2019; Hoover et al., 2017).

This study highlights the historically underrecognized role of groundwater in coastal flood risk and resilience planning. Traditional sea level rise models focus primarily on surface inundation from marine overtopping or storm surge, often overlooking subsurface contributions. However, recent research shows that including groundwater rise in flood projections can nearly double the estimated area at risk (Anderson et al., 2018; Rozell, 2021). The findings presented here underscore the need for integrated assessments that account for hydrologic amplification through infrastructure and artificial fill, especially in communities already facing aging utilities and legacy contamination.

The historical development of the San Francisco Bay shoreline has compounded these risks. Over 90% of the region's original tidal wetlands were diked or filled by the early 20th century (Atwater et al., 1977; SFEI, 2021). These fill materials were often undocumented and poorly compacted, resulting in highly variable subsurface conditions. When intersected by preferential flow pathways (PFPs), such as utility trenches, these heterogeneities can enhance groundwater movement and surface emergence. Legacy infrastructure, including abandoned or leaking sewer lines, is frequently unmapped and can act as subsurface flow conduits under both recharge and tidal pressure. The widespread use of bedding sand and gravel in trench backfill further contributes to preferential flow networks within otherwise low-permeability urban fill zones.

2.4.1 Groundwater Emergence Risk 2025-2050

Groundwater emergence risk was evaluated using a categorical scoring system from 0 to 5, where each score represents the likelihood and severity of groundwater, or in some cases, sea level, reaching or exceeding the ground surface. Groundwater emergence risk scores (**Table 2.2**) offer a clear framework for visualizing vulnerability across multiple sites in a heatmap format. A risk score of 4 represents imminent emergence, where groundwater lies within 0.20 m of the surface, while a score of 5 indicates severe emergent conditions, where groundwater reaches or exceeds the ground surface.

Table 2.2: Groundwater Emergence Risk Score Descriptions

Risk Score	Condition Description	Emergent Groundwater Risk
5	Groundwater ≥ Surface (Emergent Groundwater)	Severe emergent conditions
4	Surface - GW >0.20 m	Imminent emergent conditions
3	Surface - GW > 0.20 m and ≤ 0.40 m	Significant risk
2	Surface - GW > 0.40 m and ≤ 0.60 m	Moderate risk
1	Surface - GW > 0.60 m and ≤ 0.80 m	Minimal risk
0	Surface - GW > 0.80 m	No emergence risk

SLR projections began in 2025, anchored to a baseline of 0.72 m AMSL, based on San Francisco NOAA tide gauge station (#9414290). Subsidence rates were applied to account for site-specific surface lowering over time. Artificial fill areas were assigned a subsidence rate of 10 mm/year, as estimated by Govorcin et al. (2025), while alluvial fans and bedrock areas were assigned 2 mm/year, following estimates by Shirzaei and Bürgmann (2018). SLR was modeled at 10 mm/year, consistent with NOAA's Intermediate SLR scenario (Sweet et al., 2017; California OPC, 2018 and 2024), a widely used projection in coastal planning. These parameters were used to estimate when and where groundwater would intersect the ground surface, both under SLR and elevated groundwater conditions associated with AR events.

The framework was applied to contaminated sites where groundwater emergence can impose a greater risk. A total of 30 contaminated sites (**Figure 2.11**) were evaluated using this framework, including 21 contaminated sites (Greenaction, 2023), comprising 7 military sites and 14 industrial sites. In addition, San Francisco International Airport (SFO) and Oakland Airport (OAK-Bay Farm) were added to the study list. All 30 study sites were assessed for surface elevation (m AMSL) and groundwater elevation (m AMSL). HAT events were also analyzed, but groundwater response to HAT events was generally smaller and more localized than the response to AR events. Therefore, AR events were used as the primary scenario for extreme event modeling. Estimated temporary groundwater rise during AR events in trench areas was modeled as an additional 0.40 meters per event, based on the average observed response in Manzanita trench wells (0.42 m per event). Regulatory agency files were used to identify recent depth to groundwater at the contaminated sites, and a groundwater mapping tool (SFEI, 2025) was used for the remaining sites. Google Earth Pro was used to obtain surface elevation data.

The groundwater emergence heatmap (**Figure 2.12**) shows differences in vulnerability across sites and changes in risk over time, from 2025 to 2050. Sites were arranged from least to most flood-prone (top to bottom), with each row displaying two lines per site: the top-line representing risk under Normal conditions with no HAT or AR events, and the bottom-line representing risk under AR conditions. The sites most vulnerable to groundwater emergence, those scoring 4 or 5 under AR conditions beginning in 2025, are concentrated in low-lying, coastal areas built on artificial fill or reclaimed tidal marsh. These include SFO and OAK, where sea level is projected to reach surface elevation, and Manzanita (MZ), Tamalpais Valley (TV), Corte Madera (CM), San Rafael (SR) south Novato (SN), Foster City (FC), and Atchison Village (AV) where emergent groundwater has been observed as springs, seeps, or pools. Other sites include Treasure Island, Mare Island, and Alameda Naval Air Station. All of these areas have limited vertical separation between the water table and the ground surface, even under current conditions. AR events, temporary groundwater spikes further increase the frequency and duration of flooding by 2035.

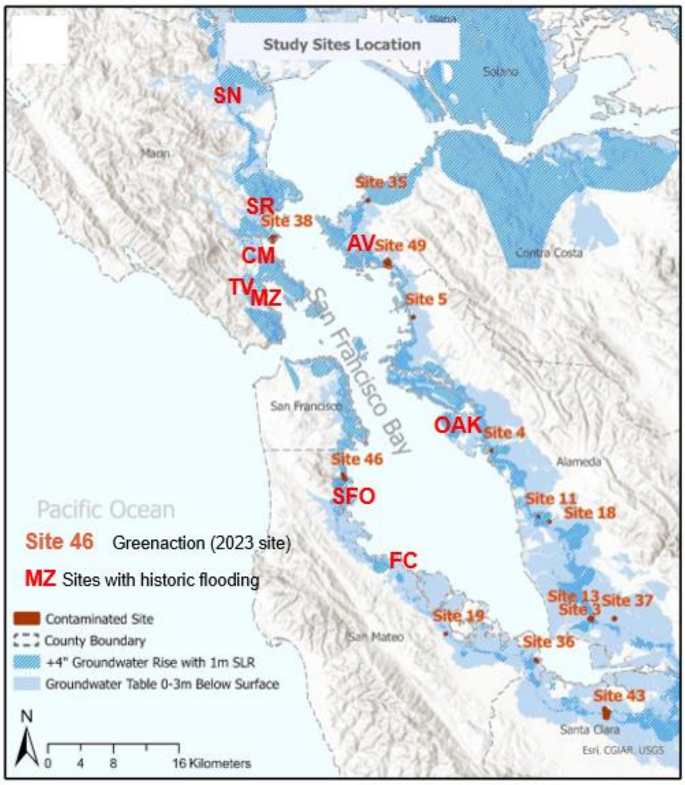

Figure 2.11: Locations of 30 Study Sites Used for Groundwater Emergence Predictions (2025–2050). Numbers refer to sites from (Greenaction, 2023). Basemap from Hill et. al. (2023) after data from Befus et al. (2020).

Many mid-elevation sites, including the Foster City (FC) residential site, as well as contaminated sites: Richmond Zeneca, the Richmond Reaction Products, East Palo Alto Romic, and Brisbane VWR, show a gradual shift from moderate to high risk in the 2040s and 2050s. These sites have buried contaminants, and although they are not immediately emergent, they are projected to cross critical thresholds as sea level rises incrementally. Risk scores at these locations typically range from 2 to 4 under Normal conditions and increase to 5, emergent conditions in trenches, by 2035 during AR events. This trend suggests a threshold-based response, where a combination of SLR and episodic recharge causes sudden groundwater emergence once capacity is exceeded. These sites would benefit from proactive planning, long-term monitoring, and early-warning systems.

By contrast, high-elevation and inland sites, such as Point Molate and San Quentin Prison, maintain low risk scores (0–1) across all years and scenarios. Located more than five m above sea level, they are not expected to experience direct groundwater emergence through 2050. However, these sites may still face indirect risks, such as subsurface lateral flow or contaminant transport along infrastructure corridors, especially if regional gradients shift in response to pressure from lower-elevation areas.

The heatmap structure aligns closely with known patterns of elevation, land use history, and tidal influence. The most flood-prone sites, those appearing at the bottom of the chart, are typically constructed on artificial fill over former wetlands and are located near the shoreline. This pattern underscores the importance of geologic setting as key screening criteria for assessing groundwater emergence vulnerability.

2.4.2 Predicting Groundwater Emergence and Marine Overtopping

To evaluate future flooding risks at a low-lying site like Tamalpais Valley from both groundwater and marine sources, we apply two separate time-to-surface equations: one for groundwater emergence during extreme precipitation, assuming groundwater rise within a trench during an AR event, and one for marine overtopping driven by SLR during a HAT event.

The time (t) when groundwater reaches the ground surface during an atmospheric river (AR) event is calculated by accounting for land subsidence and AR event-driven rise of 0.4 m in groundwater within a trench (**Equations 2.3** and **2.4**):

$$GW_0 + \Delta h\_AR = SE_0 - r\_subs \cdot t; \qquad \text{Solving for t:} \tag{2.3}$$

$$t = (SE_0 - GW_0 - \Delta h\_AR) / r\_subs \tag{2.4}$$

The time (t) when sea level and a HAT event with a groundwater response of 0.25 m in a trench reach the land surface (accounting for subsidence) is (**Equations 2.5** and **2.6**).

$$SL_0 + \Delta h\_HAT + r\_SLR \cdot t = SE_0 - r\_subs \cdot t; \quad \text{Solving for t:} \tag{2.5}$$

$$t = (SE_0 - SL_0 - \Delta h\_HAT) / (r\_SLR + r\_subs) \tag{2.6}$$

where,

SE_0: Initial surface elevation (m AMSL)

GW_0: Initial groundwater elevation (m AMSL)

Δh_AR: Groundwater rise from an AR event (m)

SL_0: Initial sea level relative to mean sea level (m)

Δh_HAT: Sea level rise from a HAT event (m)

r_SLR: Rate of sea level rise (m/year), typically 0.01 m/year (0.01 m/year)

r_subs: Rate of land subsidence (0.01 m/year)

t: Time in years from base year (assumed to be 2025)

2.4.3 Example Calculations for Tamalpais Valley

Assumptions:

$SE_0 = 3.0$ m AMSL

$SL_0 = 0.72$ m

$GW_0 = 2.5$ m AMSL

$\Delta h\_AR = 0.4$ m

$\Delta h\_HAT = 0.25$ m

$r\_SLR = 0.01$ m/year

$r\_subs = 0.01$ m/year

1. Groundwater emergence (AR event):

$t = (3.0 - 2.5 - 0.4) / 0.01 = 0.1 / 0.01 = 10$ years → Year = 2025 + 10 = 2035

2. Marine overtopping (SLR + HAT + subsidence):

$t = (3.0 - 0.72 - 0.25) / (0.01 + 0.01) = 2.03 / 0.02 = 101.5$ years → Year = 2025 + 102 = 2127

Groundwater, amplified by an AR event, is projected to reach the ground surface by the year 2035. In contrast, marine overtopping from the combined effects of SLR and a HAT event in a trench is not expected to reach the surface until 2127.

AR events consistently increase groundwater emergence risk across nearly all sites, particularly between 2035 and 2050. This intensification reflects the combined effect of long-term sea level rise and short-term groundwater elevation during extreme rainfall. Atchison Village, for example, already experienced flooding from stormwater backflow and poor drainage. Under

Normal conditions, its risk scores remain moderate but rise to high under AR conditions within two decades. This demonstrates that AR events act as tipping points, accelerating groundwater emergence within trenches at sites already near threshold, and trenches amplify groundwater emergence associated with extreme events. To improve the accuracy of emerging groundwater predictions, long-term land subsidence should be monitored through satellite-based remote sensing and field surveys in vulnerable areas.

The findings of this study emphasize the significant role of trenches in amplifying groundwater fluctuations to extreme events, particularly in coastal areas with artificial fill. The increased groundwater response near trenches raises concerns for subsurface infrastructure, including sewer and stormwater systems, which are vulnerable to prolonged saturation that can lead to structural instability, increased maintenance costs, and reduced operational efficiency. Among the most critical findings, average groundwater response was the key factor distinguishing PFP and non-PFP wells, although site-specific variability reflected local hydrogeologic conditions. Understanding the spatial variability of groundwater response within trenches compared to more distant areas is essential for developing effective short-term and long-term SLR adaptation strategies. Ultimately, a combination of infrastructure upgrades, data-driven decision-making, and integrated land-use planning will be crucial in reducing groundwater-related flood risks and enhancing the resilience of coastal communities.

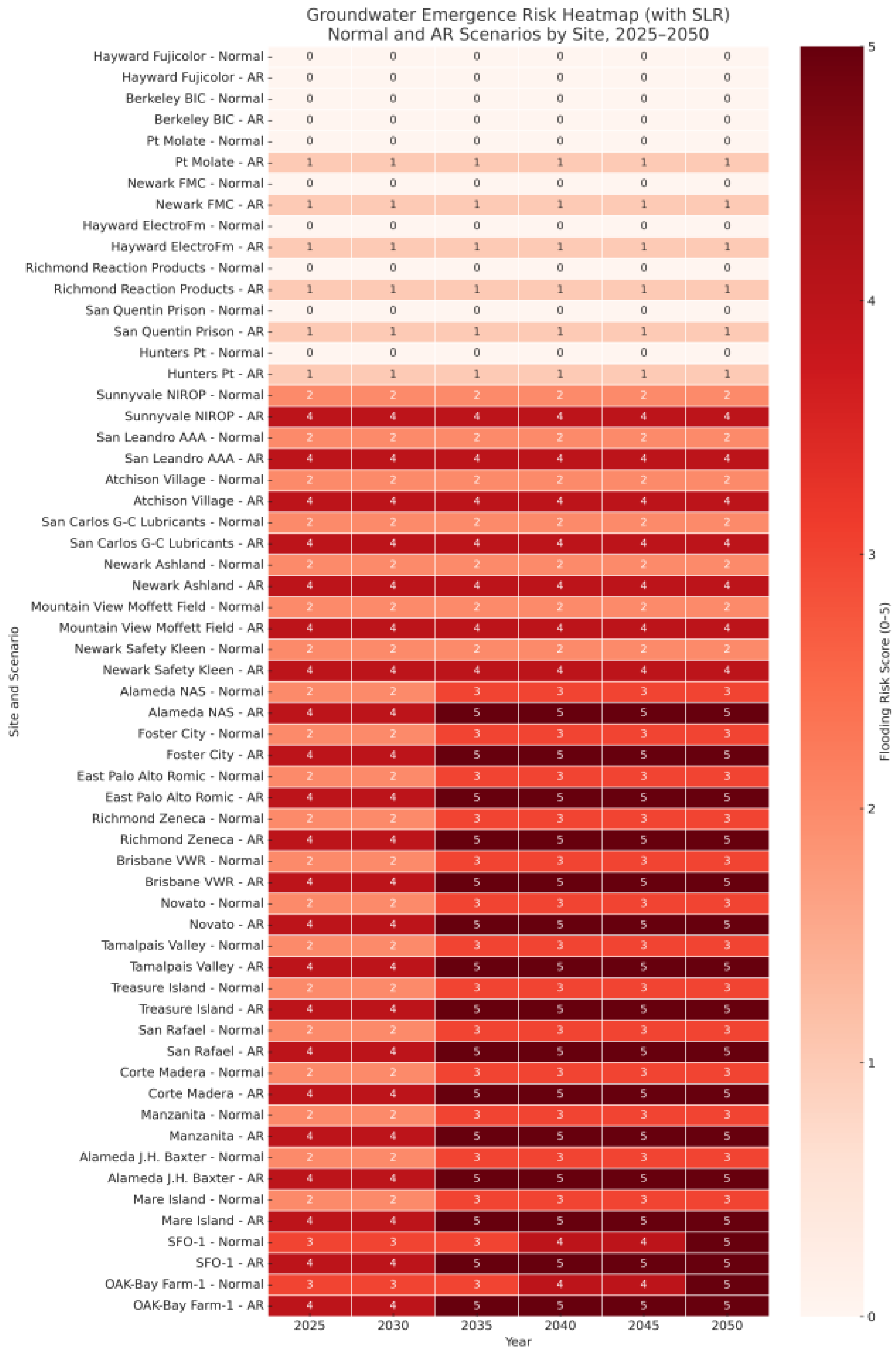
Groundwater Emergence Risk Heatmap (with SLR)
Normal and AR Scenarios by Site, 2025–2050
Site and Scenario
Year
Flooding Risk Score (0–5)
Hayward Fujicolor - Normal
Hayward Fujicolor - AR
Berkeley BIC - Normal
Berkeley BIC - AR
Pt Molate - Normal
Pt Molate - AR
Newark FMC - Normal
Newark FMC - AR
Hayward ElectroFm - Normal
Hayward ElectroFm - AR
Richmond Reaction Products - Normal
Richmond Reaction Products - AR
San Quentin Prison - Normal
San Quentin Prison - AR
Hunters Pt - Normal
Hunters Pt - AR
Sunnyvale NIROP - Normal
Sunnyvale NIROP - AR
San Leandro AAA - Normal
San Leandro AAA - AR
Atchison Village - Normal
Atchison Village - AR
San Carlos G-C Lubricants - Normal
San Carlos G-C Lubricants - AR
Newark Ashland - Normal
Newark Ashland - AR
Mountain View Moffett Field - Normal
Mountain View Moffett Field - AR
Newark Safety Kleen - Normal
Newark Safety Kleen - AR
Alameda NAS - Normal
Alameda NAS - AR
Foster City - Normal
Foster City - AR
East Palo Alto Romic - Normal
East Palo Alto Romic - AR
Richmond Zeneca - Normal
Richmond Zeneca - AR
Brisbane VWR - Normal
Brisbane VWR - AR
Novato - Normal
Novato - AR
Tamalpais Valley - Normal
Tamalpais Valley - AR
Treasure Island - Normal
Treasure Island - AR
San Rafael - Normal
San Rafael - AR
Corte Madera - Normal
Corte Madera - AR
Manzanita - Normal
Manzanita - AR
Alameda J.H. Baxter - Normal
Alameda J.H. Baxter - AR
Mare Island - Normal
Mare Island - AR
SFO-1 - Normal
SFO-1 - AR
OAK-Bay Farm-1 - Normal
OAK-Bay Farm-1 - AR
2025
2030
2035
2040
2045
2050
0
1
2
3
4
5

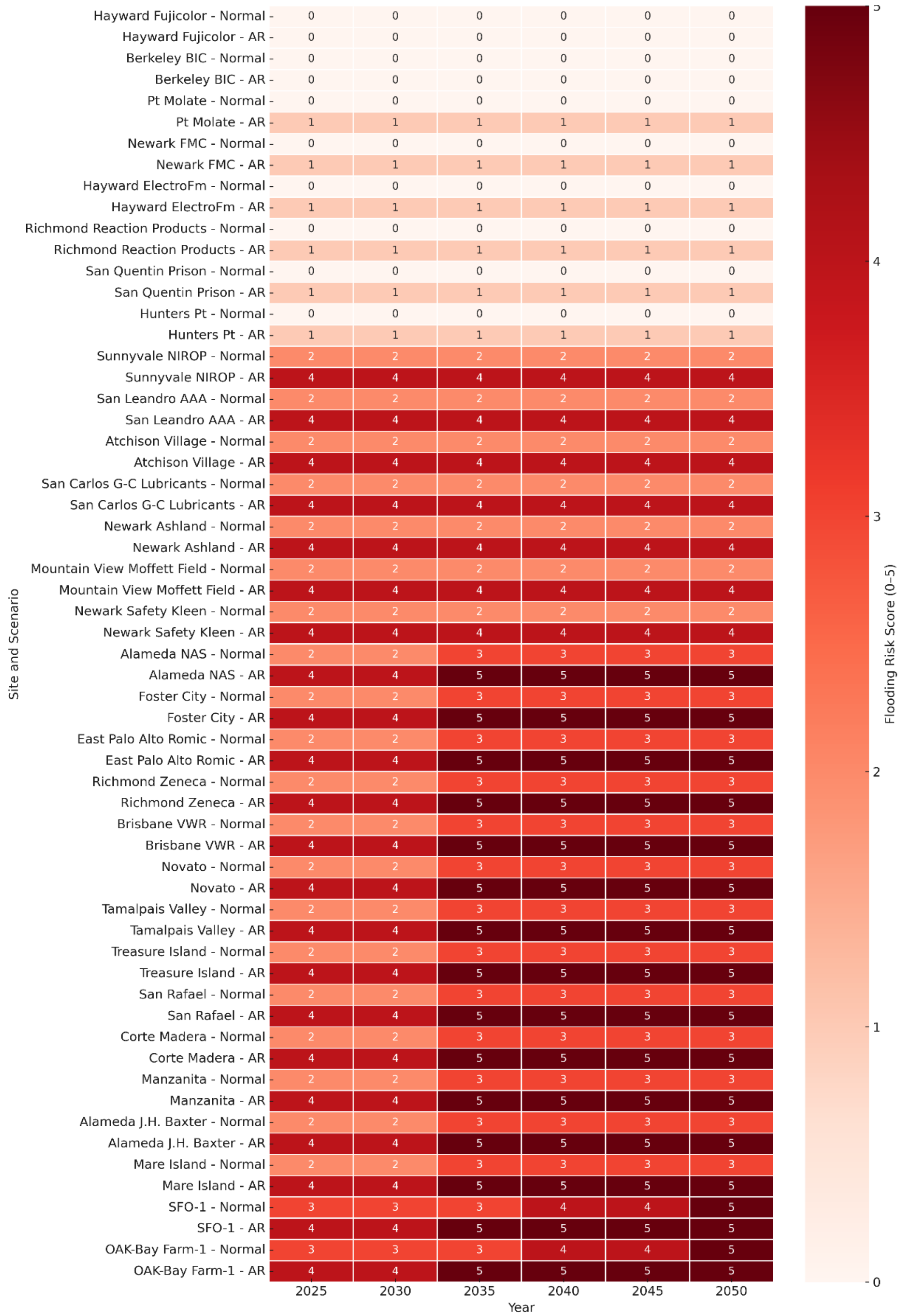

Figure 2.12: Simulated emergence groundwater risk heatmap from trench simulations at 30 coastal sites influenced by SLR and subsidence, with AR and normal scenarios (2025–2050)

3 Emerging Groundwater as a Hidden Hazard: Differentiating Subsurface Flooding Sources Using Ion Geochemistry and Stable Water Isotopes

Abstract

Emerging groundwater is an underrecognized but growing hazard in low-lying coastal areas affected by sea level rise, land subsidence, and extreme precipitation. In urbanized settings where infrastructure intersects shallow water tables, groundwater can breach the surface during high tides or storms, often resembling stormwater ponding, sewer overflow, or tidal backflow. Identification is difficult where low-permeability soils cause surface pooling that mimics groundwater emergence. This study uses stable isotope ratios (δ^2H and $\delta^{18}O$) and major ion chemistry to distinguish emerging groundwater from other surface water sources across three San Francisco Bay Area sites with a history of flooding: Manzanita and Tamalpais Valley, underlain by artificial fill over former wetlands, and Atchison Village, built on poorly drained alluvial sediments. Water samples were collected from groundwater wells, crawlspaces, surface water, sewer overflow, and tidal inlets during atmospheric river events and highest astronomical tide events. Isotopic data were evaluated relative to both global and local meteoric water lines, while ternary

mixing models based on diagnostic ion ratios ($Na^+ + Cl^-$, HCO_3^-, $Mg^{2+} + Ca^{2+}$) were used to estimate source contributions. Results indicate that emerging groundwater was geochemically and isotopically consistent with local groundwater, distinguishing it from direct rainfall, wastewater, tap water, and saltwater sources. These findings demonstrate that geochemical tools can identify groundwater emergence across diverse subsurface conditions and highlight its underappreciated role in compound flooding. As groundwater levels rise in response to climate-driven sea level rise, the ability to accurately identify groundwater emergence will be essential for flood mitigation, infrastructure planning, contaminant management, and effective coastal adaptation.

3.1 Introduction

Traditional flood risk assessments primarily focus on surface water inundation and do not account for emerging groundwater as a risk (Rotzoll and Fletcher, 2013; Befus et al., 2020). Specifically, groundwater geochemistry can shed light on groundwater dynamics and how it is related to flood risks (Michael et al., 2017). Geochemical analysis, including ion chemistry and stable water isotopes ($\delta^{18}O$, δ^2H), provides essential insight into how groundwater interacts with surface water, stormwater, and seawater (Vengosh et al., 2005; Stuyfzand, 2008; and Clark and Fritz, 2013). Ion chemistry identifies the sources and transformations of groundwater constituents, distinguishing between saltwater intrusion, stormwater infiltration, and wastewater contamination (Barlow and Reichard, 2010; and Cartwright et al., 2014). Stable water isotopes trace water source mixing, recharge timing, and evaporation effects, allowing for differentiation between recent stormwater infiltration and older groundwater

(Kendall and McDonnel, 2012; and Kennedy et al., 2012).

Multiple interrelated factors contribute to emerging groundwater and altered groundwater chemistry in urban coastal environments (Werner et al., 2013; and Yu et al., 2018). Sea level rise (SLR) raises regional water tables, reducing vadose zone thickness, increasing groundwater emergence, hydrostatic pressure, and surface water-groundwater connectivity in low-lying areas which can result in flooding (Ferguson and Gleeson. 2012; and Hoover et al., 2017). The rising water table enhances mixing between existing water sources, altering groundwater geochemistry. While such mixing can accelerate saltwater intrusion in other unconfined coastal aquifers (Cooper et al., 1964; Werner and Simmons, 2009), at Manzanita it primarily results in geochemical changes driven by interactions between meteoric and tidally influenced waters. Elevated sodium (Na^+) and chloride (Cl^-) concentrations, along with enriched $\delta^{18}O$ and $\delta^{2}H$ values, are key indicators of mixing of seawater with groundwater (Post and Werner, 2017; and Jiao and Post, 2019).

Highest astronomical tides (HAT) and atmospheric river (AR) events, further intensify groundwater responses (Bjerklie et al., 2018; and Ralph et al., 2018 and 2019). HAT events push tidal water into coastal groundwater zones, increasing hydraulic gradients and this process is reflected in geochemical shifts, including increased salinity and altered ion ratios indicative of tidal mixing (Robinson and Barry, 2007; and Levanon et al., 2017). AR events generate intense rainfall, leading to rapid groundwater recharge and temporary dilution of ion concentrations (Dettinger, 2011; and Gershunov et al., 2017). These storm-driven fluctuations in groundwater chemistry provide a means to assess how different water sources interact in different locations (Levanon et al., 2017). Groundwater rise can lead to emerging groundwater (Plane et al., 2019, Hill et al., 2023).

The San Francisco Bay region is highly vulnerable to groundwater rise and emerging groundwater during and after extreme events due to its complex hydrogeology, extensive land use modifications, and aging stormwater and wastewater infrastructure (Holleman and Stacey, 2014; and Plane et al., 2019). Sewer utility trenches, a significant but often overlooked hydrologic factor, create preferential flow pathways that modify stormwater recharge, alter groundwater flow direction, increase mixing between water sources, and accelerate water table rise during extreme events (Sharp et al., 2010; and Bonneau et al., 2017). Land use modifications further exacerbate the effects of extreme events. The replacement of wetlands with artificial fill alters the natural hydrologic balance, reducing infiltration capacity and increasing surface runoff (Kaushal et al., 2015; and Knüsel et al., 2019). These changes influence groundwater recharge and geochemical evolution, as urban areas lose the natural buffering capacity of historic wetland systems (Moffett et al., 2015; and Jha et al., 2017). Without the ability to absorb and filter incoming water, groundwater systems in these modified landscapes exhibit greater fluctuations in ion concentrations, increased vulnerability to saltwater intrusion, and more pronounced geochemical variability (Foppen, 2002; and Baron et al., 2013).

Building on field data collected during HAT and AR events, this study applies stable water isotope and ion-based geochemical analyses to identify groundwater emergence at representative coastal and inland settings of the San

Francisco Bay region. The central research question is: To what extent can geochemical and isotopic signatures differentiate shallow groundwater emergence from other surface water sources, such as rainfall accumulation, stormwater backflow, sewer overflow, marine inundation, or leakage from tap or irrigation systems? The study aims to improve understanding of groundwater-surface water interactions under compound flooding conditions and to support the development of diagnostic tools for identifying emerging groundwater as a source of surface flooding in vulnerable coastal settings.

3.2 Methods

This study investigates groundwater geochemistry and stable water isotopic signatures at three urban coastal sites in the San Francisco Bay Area: Manzanita and Tamalpais Valley in unincorporated southern Marin County, and Atchison Village in the City of Richmond, Contra Costa County. All three sites have a history of flooding, shallow groundwater (less than one m below the surface), groundwater emergence, and stormwater backflow. (See **Figures 2.2a-b, 2.3a-2.3i.,** and **2.4a-2.4c**).

Water sampling was conducted during HAT events throughout Water Year 2023 (October 1, 2022 – September 30, 2023). Samples were collected in November and December 2022, and in January, February, March, and September 2023 (**Figure 3.1**). To identify the sources of emerging groundwater, samples were collected from groundwater wells and nearby surface water features. Sampling was limited to dry conditions. Surface water samples were collected after at least five days following any AR event. In total, 281 water samples were collected. These included three primary end members: tap water, rainwater, and saltwater. Five secondary sources represented mixed waters—tidal inlet, groundwater, stormwater backflow, sewer overflow, and crawlspace water. One tertiary category consisted of surface water suspected to represent emerging groundwater (**Figure 3.2**).

To estimate the relative contributions of rainwater, tap water, and saltwater to sampled waters, an ion-based ternary mixing mode was used. Each ternary diagram represents normalized proportions of three ion groupings: sodium (Na^+) and chloride (Cl^-) as a proxy for saltwater, bicarbonate (HCO_3^-) for rainwater, and calcium (Ca^{2+}) plus magnesium (Mg^{2+}) for tap water. A single representative sample was used to define each end member at the corners of the ternary diagrams. The saltwater end member was selected based on a sample with a complete major ion analysis and a combination of high chloride concentration and elevated electrical conductivity. Rainwater and tap water end members were defined by averaging multiple samples, when available.

Ion concentrations were normalized to sum to 100% for each sample, enabling comparison across sites. This model assumes conservative mixing with minimal in-situ geochemical alteration. Although it simplifies complex hydrologic and geochemical processes, by treating each ion group as uniquely tied to one source, it provides a useful first-order approximation of source mixing. Interpretations were made in the context of local hydrogeologic conditions. The results reflect ion-based mixing trends rather than exact volumetric contributions.

This approach is adapted from methods described by Jiao and Post (2019) and Cartwright et al. (2007). While useful for identifying broad mixing trends, it does not account for geochemical reactions such as carbonate dissolution or ion exchange, which may alter ion concentrations and affect source estimates. However, to identify emerging groundwater from surface water samples, this method provides a practical first-order tool for distinguishing likely source contributions based on relative ion signatures. Water samples were also analyzed for stable isotopes of water ($\delta^{18}O$ and $\delta^{2}H$) to support source identification and mixing analysis.

A flood driver conceptual diagram illustrates the three primary mechanisms of flooding: marine overtopping (see **Figure 2.3a**), stormwater backflow (see **Figure 2.3b**), and groundwater emergence (see **Figure 2.3c**), with corresponding field observations from Manzanita (see **Figure 2.3d–2.3f**) and Tamalpais Valley (see **Figure 2.3g–2.3i**).

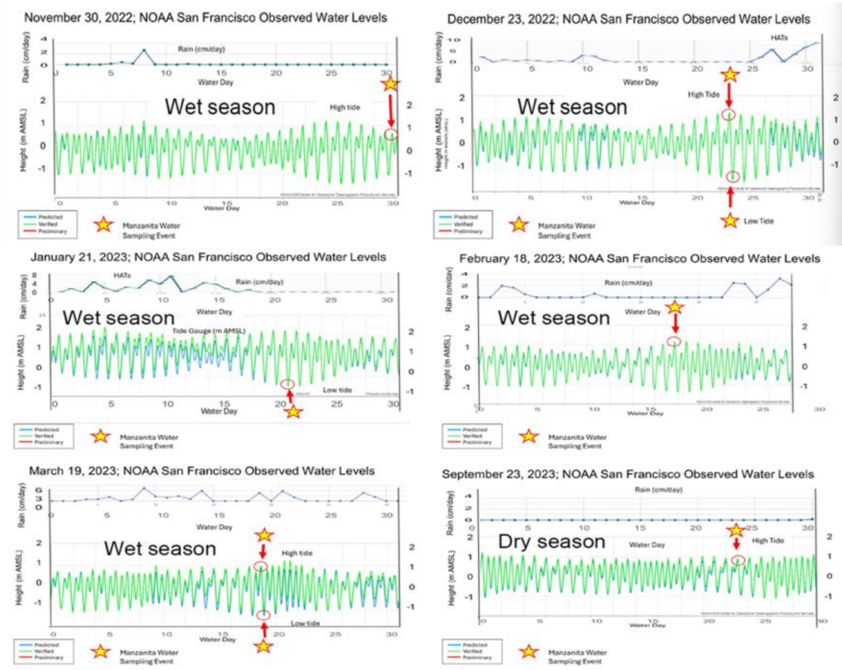

Figure 3.1: Sample collection dates defined by HAT events

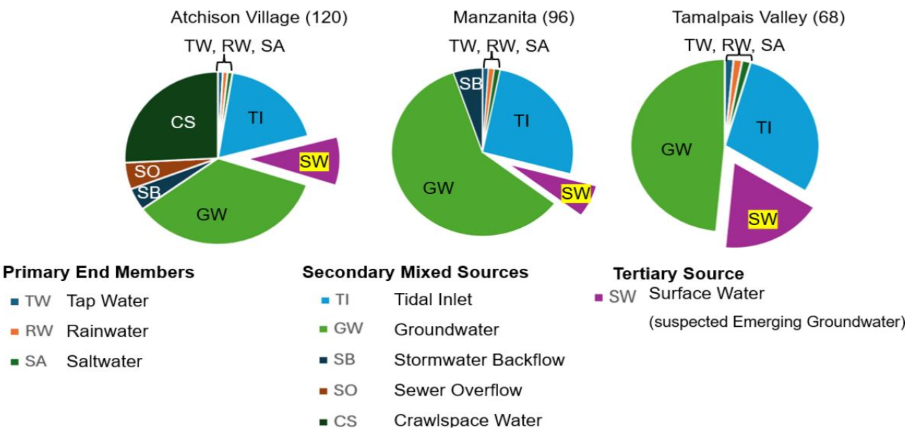

Figure 3.2: Distribution of 281 water samples from the three sites.

Manzanita (see **Figure 2.3a**), the site closest to Richardson Bay, is directly influenced by tidal exchange. Seven soil borings (MW1–MW7) conducted for this study are located 1 to 79 m of the shoreline. Based on boring logs, artificial fill at the site ranges in thickness from 2.20 to 3.02 m and consists predominantly of clay (CL), with lesser amounts of sand, gravel, and construction debris such as brick fragments (this study). This artificial fill overlies the Young Bay Mud, a highly plastic clay (CH) (GEI, 2015; GEI, 2016), interpreted as wetland deposits. Shallow groundwater at Manzanita is unconfined and perched atop the Young Bay Mud. Groundwater generally drains toward the engineered tidal inlet that connects to Richardson Bay.

Tamalpais Valley (see **Figure 2.3b**) is drained primarily by Coyote Creek, an engineered channel that conveys tidal flows further inland. Four wells (TVW1–TVW4) located 683 to 1,410 m inland indicate that the artificial fill ranges in thickness from 2.08 to 2.29 m (this study). This artificial fill overlies the Young Bay Mud, a plastic clay interpreted as historic wetland deposits (GEI, 2015). Shallow groundwater in Tamalpais Valley is unconfined, perched above the Young Bay Mud. Evidence of shallow groundwater in Tamalpais Valley includes water wicking through wood and concrete surfaces and frequent sump pump activity (**Figure 3.3**).

Atchison Village in the City of Richmond in Contra Costa County, California, is built on poorly drained alluvial deposits that contribute to localized flooding during AR events. Deeper alluvial aquifers exist beneath Atchison Village. Atchison Village is situated on poorly drained alluvial deposits adjacent to the Santa Fe Channel. Unlike Manzanita, it is not directly impacted by marine overtopping or tidal backflow through drainage infrastructure. While the site has historically experienced stormwater backflow during extreme rainfall events, there is no evidence of tidal water intrusion via stormdrains or surface channels. The five wells (AVW1, AVW1S, AVW2-AVW4) are located 820 to 1,190 m from the shoreline. Atchison Village includes 162 residential units and a community center. Crawlspaces (**Figure 3.4**) are located 0.5 to 1.5 meters below ground surface, and most units experience chronic flooding, with standing water depths typically ranging from 0.1 to 0.3 meters (McMinn, 2017). Sump pumps are commonly used for dewatering, and as of 2017, 163 sump pumps were in operation across the property (McMinn, 2017; B. Postel, personal communication).

Major ion chemistry and stable isotope analysis were used to identify the dominant water sources contributing to groundwater, surface water, crawlspace water, sewer overflow, and tidal inlet samples across the three sites. Source contributions were evaluated using three water source end members: rainwater, tap water, and saltwater. For the adjacent study sites of Manzanita and Tamalpais Valley, a single rainwater and a single tap water sample collected in Tamalpais Valley were used to represent both areas, while saltwater end member samples were collected from Richardson Bay. For Atchison Village, rainwater and tap water samples were collected within the residential area, and the saltwater end member samples were taken from the Santa Fe Channel, a tidal waterway connected to San Francisco Bay. Major ions were grouped into three diagnostic indicators: Na^{+} + Cl^{-} for saltwater, HCO_3^{-} for rainwater, and Mg^{2+} + Ca^{2+} for tap water. For each water sample, the summed concentration of these three groups was normalized to 100%, resulting in a ternary composition that reflects the relative influence of the three sources. Although the end members (rainwater, saltwater, and tap water) approached pure-source conditions, none plotted exactly at the triangle vertices due to minor ion contributions. This deviation is expected in environmental systems and reflects natural variability in atmospheric deposition, infrastructure leaching, and analytical precision.

The normalized ternary compositions were averaged for each of the mixed-source water types, including groundwater, crawlspace water, surface water, sewer overflow, and tidal inlet, and visualized using a ternary diagram. Stable isotope ratios (δ^2H and $\delta^{18}O$) were used to assess hydrologic processes and further constrain water sources. These values were plotted against the Global Meteoric Water Line (GMWL) and an approximate Local Meteoric Water Line (LMWL) for coastal northern California (Craig, 1961, Ingram and Taylor, 1991, Clark and Fritz, 1997, Gat, 1996) with symbols matching those used in the ternary plot.

Figure 3.3: Evidence of shallow groundwater in Tamalpais Valley (red ovals, top row) and sump pump, lower left and sump pump discharge pipes (lower right)

Figure 3.4: Photo of crawlspace water which has been observed in the wet season (photo from Barbara Postel)

3.3 Results

We performed end member mixing calculations to evaluate the relative contributions of rainwater, tap water, and saltwater to various surface and subsurface mixed-source waters across all three sites. The resulting average source proportions are summarized in **Table 3.1.** Due to their geographic proximity and similar hydrologic settings, Manzanita and Tamalpais Valley shared the same endmembers for saltwater, rainwater, and tap water.

Table 3.1: Summary of end member and mixed-source water samples

Manzanita: 0 - 79 m from the shoreline							
Sample Type	**End Member**	**Mixed Source**	**Symbol**	**% Saltwater**	**% Rainwater**	**% Tap Water**	**%**
Rainwater	X		RW	43.9	30.5	25.5	99.9
Saltwater	X		SA	88.2	0.4	11.4	100.0
Tap Water	X		TW	43.9	30.5	25.5	99.9
Groundwater		X	GW	65.4	8.5	26.1	100.0
Stormwater Backflow		X	SB	77.6	4.8	17.6	100.0
Surface Water		X	SW	57.8	18	24.2	100.0
Tidal Inlet		X	TI	84.9	1.3	13.8	100.0
Tamalpais Valley: 683 -1410 from the shoreline							
Sample Type	**End Member**	**Mixed Source**	**Symbol**	**% Saltwater**	**% Rainwater**	**% Tap Water**	%
Rainwater	X		RW	43.9	30.5	25.5	99.9
Saltwater	X		SA	88.2	0.4	11.4	100.0
Tap Water	X		TW	43.9	30.5	25.5	99.9
Groundwater		X	GW	63.6	13.4	23.0	100.0
Emerging Groundwater		X	EM	81.5	4.1	14.4	100.0
Tidal Inlet		X	TI	80.8	7.0	12.4	100.1
Atchison Village: 820 - 1410 m from the shoreline							
Sample Type	**End Member**	**Mixed Source**	**Symbol**	**% Saltwater**	**% Rainwater**	**% Tap Water**	**%**
Rainwater	X		RW	68.2	10.5	21.2	99.9
Saltwater	X		SA	88.7	0.4	10.9	100.0
Tap Water	X		TW	41.8	28.4	29.8	100.0
Crawlspace Water		X	CS	41.7	27.0	31.3	100.0
Groundwater		X	GW	41.0	26.7	32.3	100.0
Sewer Overflow		X	SO	41.6	25.1	33.3	100.0
Surface Water		X	SW	39.7	27.4	32.9	100.0
Tidal Inlet		X	TI	57.5	14.3	28.2	100.0

3.3.1 Manzanita

Geochemical mixing analysis of Manzanita water samples showed a broad range of source contributions. Most samples reflected mixing among saltwater ($Na^+ + Cl^-$), tap water ($Ca^{2+} + Mg^{2+}$), and rainwater (HCO_3^-). In the ternary diagram (**Figure 3.5**), groundwater samples clustered closer to the saltwater–tap water axis, indicating these were the dominant sources influencing subsurface chemistry. Emerging groundwater and surface water samples plotted within the ternary space defined by these three end members, suggesting subsurface mixing.

Groundwater samples had an average saltwater contribution of 65.4%, indicating significant marine influence, likely due to tidal channel infiltration during HAT events. Stormwater backflow samples had even higher saltwater content (77.6%), with minimal rainwater input (4.8%), suggesting dominance by saline backflow rather than freshwater runoff. Surface water and tidal inlet samples also reflected elevated saltwater proportions (57.8% and 84.9%, respectively), consistent with estuarine intrusion or marine overtopping in low-lying areas.

Stable isotope analysis (**Figure 3.6**) further identifies water sources. Groundwater samples exhibited moderately depleted isotopic values, averaging –4.40‰ for $\delta^{18}O$ and –26.25‰ for $\delta^{2}H$. Stormwater backflow samples showed nearly identical isotopic compositions (–4.46‰ $\delta^{18}O$, –28.86‰ $\delta^{2}H$), indicating a close hydrologic relationship with groundwater. Surface water samples were more isotopically depleted (–7.04‰ $\delta^{18}O$, –49.36‰ $\delta^{2}H$).

Tidal inlet samples showed intermediate enrichment (–3.67‰ $\delta^{18}O$, –23.31‰ $\delta^{2}H$), consistent with a mix of estuarine and meteoric water. Saltwater end member samples from Richardson Bay were highly enriched (–1.87‰ $\delta^{18}O$, –11.16‰ $\delta^{2}H$), while both tap water and rainwater had identical compositions (–2.25‰ $\delta^{18}O$, –14.71‰ $\delta^{2}H$), aligning with the local meteoric water line and serving as reference end members.

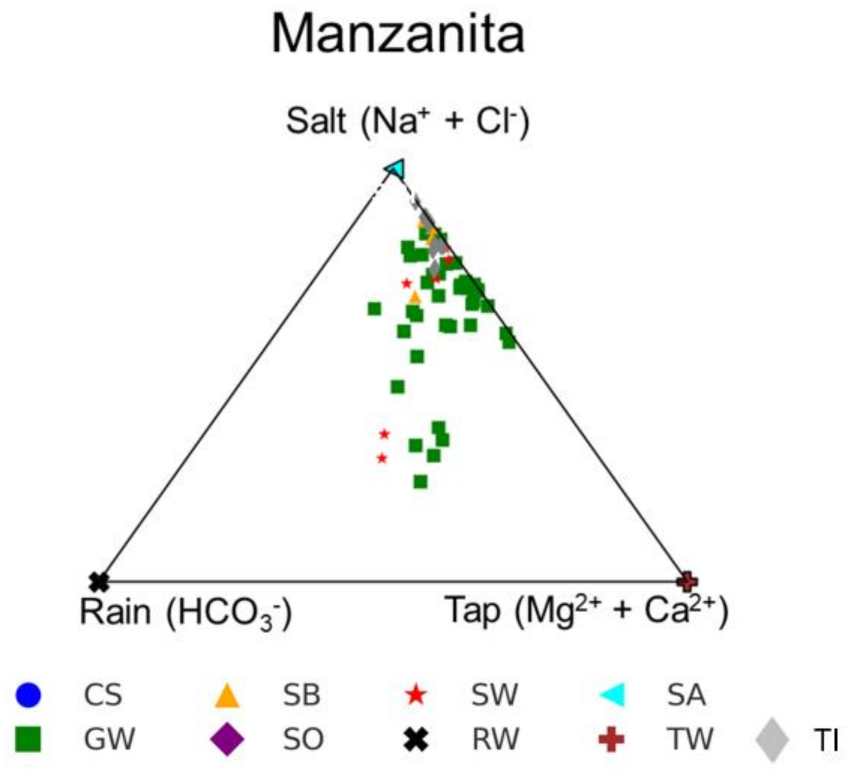

Figure 3.5: Manzanita ternary diagram. Abbreviations include Manzanita (MZ), crawlspace water (CS), groundwater (GW), rainwater (RW), saltwater (SA), stormwater backflow (SB), surface water (SW), tidal inlet (TI), and tap water (TW).

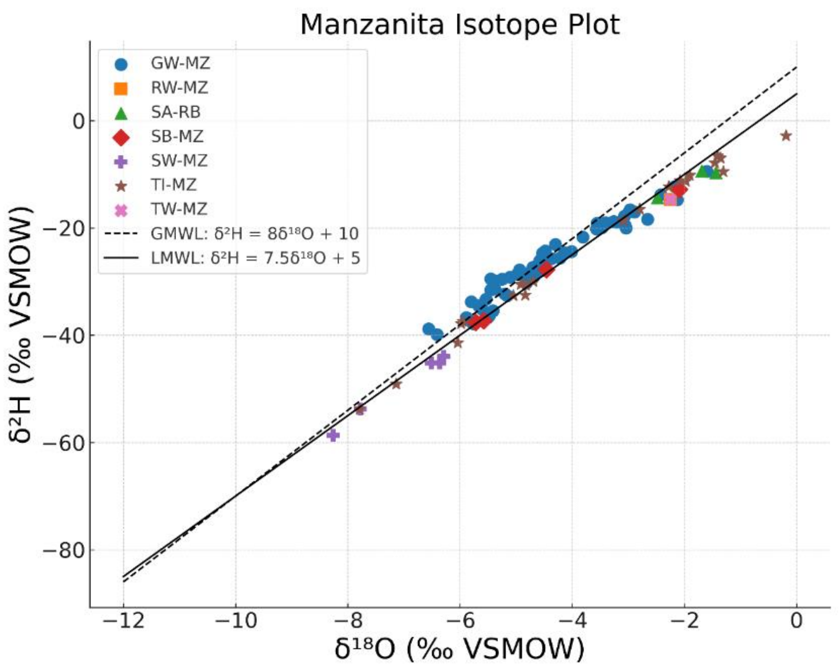

Figure 3.6: Manzanita stable water isotope plot

3.3.2 Tamalpais Valley

Tamalpais Valley groundwater samples had an average saltwater content of 63.6%, while emerging groundwater was more saline, with 81.5% saltwater contribution (see **Table 3.1**). Tidal inlet samples showed elevated saltwater concentrations, averaging 80.8%, with minor contributions from rainwater and tap water. The ternary diagram for Tamalpais Valley (**Figure 3.7**) shows groundwater samples clustering near the saltwater–tap water axis. Tidal inlet samples, including those from Coyote Creek and the Crest Marin tributary, plotted along the saltwater axis, reflecting high estuarine influence.

Stable isotope analysis (**Figure 3.8**) further differentiated sample types. Emerging groundwater exhibited the most isotopically depleted values, with mean $\delta^{18}O$ of −4.72‰ and $\delta^{2}H$ of −28.98‰. Groundwater samples were slightly more enriched, averaging −3.86‰ for $\delta^{18}O$ and −23.27‰ for $\delta^{2}H$. Tidal inlet samples showed intermediate enrichment, with values around −3.8‰ for $\delta^{18}O$ and −21.0‰ for $\delta^{2}H$. Rainwater and tap water had identical isotopic values ($\delta^{18}O$: −2.25‰; $\delta^{2}H$: −14.71‰), consistent with the local meteoric water line. The saltwater samples from Richardson Bay were the most enriched samples, averaging −1.87‰ $\delta^{18}O$ and −11.16‰ $\delta^{2}H$.

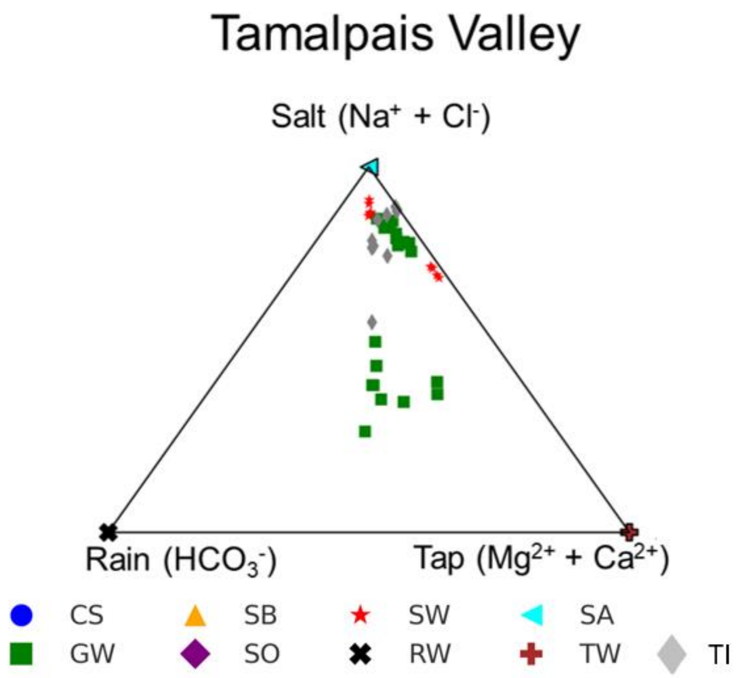

Figure 3.7: Tamalpais Valley ternary diagram. Abbreviations include Tamalpais Valley (TV), emerging groundwater (EM), groundwater (GW), rainwater (RW), saltwater (SA), stormwater backflow (SB), tidal inlet (TI), and tap water (TW).

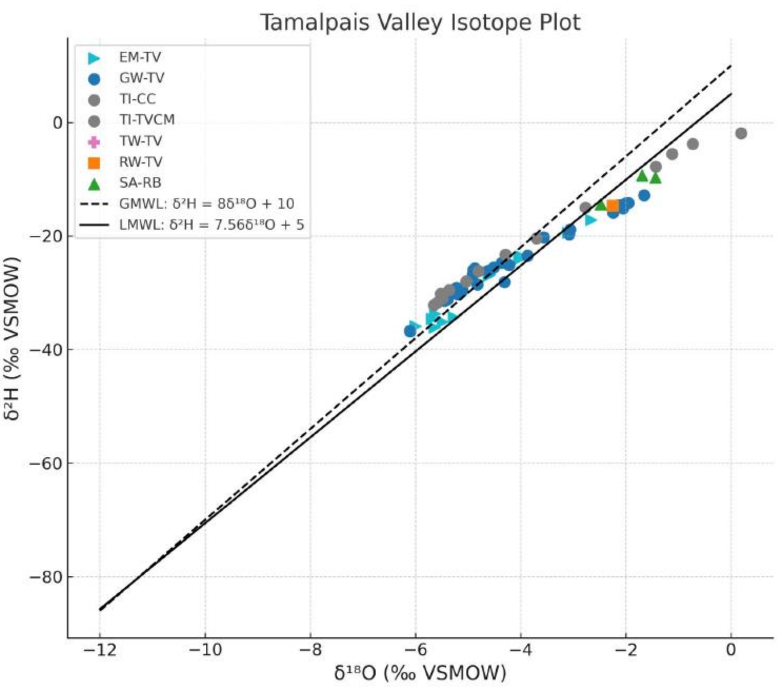

Figure 3.8: Tamalpais Valley stable water isotope plot

3.3.3 Atchison Village

Ternary mixing analysis of water samples from Atchison Village (**Figure 3.9**) showed a more balanced contribution from the three end members compared to the more tidally influenced sites of Manzanita and Tamalpais Valley. Groundwater, crawlspace water, sewer overflow, and surface water samples each displayed relatively equal proportions of saltwater (39–42%), tap water (30–33%), and rainwater (25–27%). Tidal inlet samples also showed marine influence but with lower saltwater content (57.5%) than observed at the other sites.

End member samples plotted near their respective vertices on the ternary diagram: saltwater (high Na^+ + Cl^-), rainwater (high HCO_3^-), and tap water (high Ca^{2+} + Mg^{2+}), confirming appropriate selection for source attribution. Groundwater samples clustered near the base of the triangle, between the rainwater and tap water vertices, indicating minimal saltwater influence. Crawlspace water and surface water samples plotted closely with the groundwater cluster, while sewer overflow samples also clustered near groundwater but with slightly elevated rainwater and tap water fractions. Tidal inlet samples shifted toward the saltwater vertex, consistent with moderate marine character.

Stable isotope analysis (**Figure 3.10**) further distinguished sample types. Groundwater (–6.14‰ $\delta^{18}O$, –38.22‰ δ^2H) and crawlspace water (–6.49‰ $\delta^{18}O$, –42.39‰ δ^2H) exhibited closely aligned isotopic values, while surface water and sewer overflow were more depleted (–7.02‰ and –8.09‰ $\delta^{18}O$, respectively). These samples all plotted along or slightly below the Local Meteoric Water Line (LMWL), indicating limited evaporative enrichment. The Atchison Village surface water samples exhibit $\delta^{18}O$ and δ^2H values that are substantially more depleted than those observed in Atchison Village groundwater or crawlspace water, with $\delta^{18}O$ ranging from −8.35 to −9.36‰, more consistent with rainwater than with groundwater. Tidal inlet samples had isotopic compositions similar to groundwater. Rainwater and tap water were the most isotopically depleted (−9.37‰ $\delta^{18}O$, −66.73‰ $\delta^{2}H$), representing the meteoric end member. Saltwater from the Santa Fe Channel was the most enriched (−1.54‰ $\delta^{18}O$, −9.23‰ $\delta^{2}H$), consistent with marine origin and aligning with the Global Meteoric Water Line (GMWL).

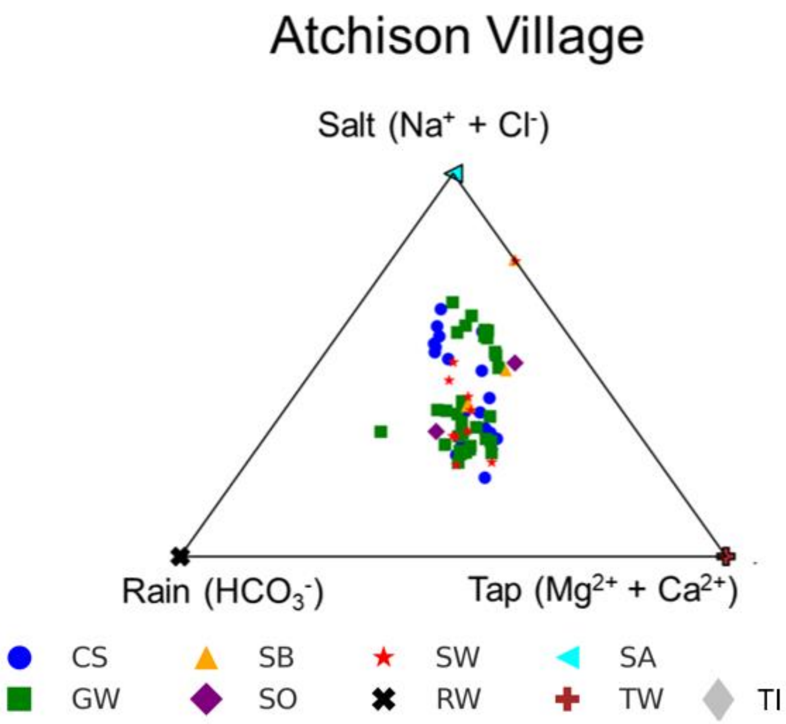

Figure 3.9: Atchison Village ternary diagrams. Abbreviations include Atchison Village (AV), crawlspace water (CS), groundwater (GW), rainwater (RW), saltwater (SA), stormwater backflow (SB), sewer overflow (SO), surface water (SW), tidal inlet (TI), and tap water (TW).

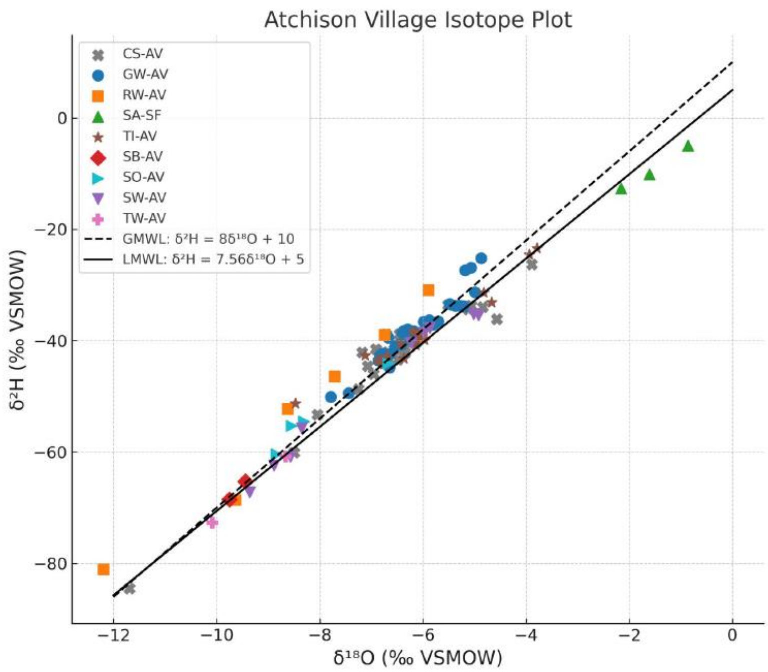

Figure 3.10: Stable water isotope plot for Atchison Village

3.4 Discussion

The ion and isotope results from all three sites underscore the importance of differentiating groundwater emergence from other mixed water sources in low-lying communities where pooling water may arise from complex combinations of urban runoff, subsurface sewer issues, and shallow groundwater rise.

3.4.1 Manzanita

At Manzanita, geochemical and isotopic data indicate active mixing between shallow groundwater, rainfall infiltration, and tidal inflows. Groundwater samples showed elevated saltwater signatures, averaging 65.4%, particularly in those with high Na^+ and Cl^- concentrations, consistent with tidal channel infiltration during high tide events. Stormwater backflow samples exhibited even higher saltwater content (77.6%) and plotted near the saltwater vertex in ternary space, indicating strong marine influence, likely from tidal backflow or overtopping during HAT events.

Stable isotope analysis reinforces these patterns. Groundwater and stormwater backflow samples had nearly identical isotopic values (−4.40‰ and −4.46‰ $\delta^{18}O$), suggesting that stormwater backflow may include recycled or displaced shallow groundwater mobilized during periods of high-water table or tidal forcing. In contrast, surface water samples were more isotopically depleted (−7.04‰ $\delta^{18}O$), indicating a distinct source likely tied to recent rainfall or upland runoff, with limited mixing from saline or groundwater sources. Tidal inlet samples showed intermediate enrichment in $\delta^{18}O$ and $\delta^{2}H$, consistent with brackish estuarine water modified by meteoric input. Saltwater end members from Richardson Bay were the most isotopically enriched and geochemically saline, serving as a clear marine reference point.

Together, these data show that in low-lying artificial fill environments like Manzanita, stormwater accumulation may resemble emerging groundwater but often originates from surface runoff or tidal backflow rather than surface discharge driven by water table rise. Multiple surface water samples from Water Year 2023 were more depleted in $\delta^{18}O$ and $\delta^{2}H$ compared to groundwater and exhibited higher rainwater fractions and lower saltwater contributions, consistent with a surface-derived origin. While some overlap in ion chemistry was observed among water types, isotopic evidence suggests that ponded surface water is not the result of emerging groundwater.

Field observations in spring 2024 (**Figures 3.11** and **3.12)** documented emerging groundwater in Manzanita occurring up to 15 days after earlier atmospheric river (AR) events. On March 13, 2024, a water sample collected from the emergent flow was analyzed in the field using a portable YSI multimeter. The sample exhibited low electrical conductivity (578 μS/cm), equivalent to approximately 0.3 ppt salinity, well below the 2 ppt freshwater threshold (Chapman, 1992; USGS, 2018). These data confirm that true groundwater emergence can occur under specific conditions and may have distinct chemical signatures, particularly during or following HAT or AR events.

The evidence highlights the importance of integrating isotopic analysis, ion chemistry, and in situ monitoring to differentiate between shallow groundwater and other surface water sources. In Manzanita, tidal dynamics and the presence of artificial fill, especially preferential flow pathways such as sewer trenches, strongly influence hydrologic responses. These findings underscore the need for site-specific characterization when evaluating flood risk and groundwater emergence in coastal urban settings.

Figure 3.11: Manzanita emerging groundwater pouring over sidewalk April 15, 2024. The location is directly above a preferential flow pathway (sewer utility trench).

Figure 3.12: Close up of emerging groundwater ponding in Manzanita on March 30, 2024.

Supporting these observations, Manzanita monitoring well MW1, located 53 m northwest of the emergence site and within the same sewer trench, recorded a water table elevation of 1.99 m AMSL on February 29, 2024, nearly identical to the estimated elevation of the emerging groundwater (1.98 m). The sustained emergence observed through March and April 2024 likely reflects delayed discharge from groundwater recharged during the extreme storms of January and February 2024.

A time-series plot of rainfall, tides, and groundwater emergence (**Figure 3.13**) illustrates the temporal dynamics of these events. The chart shows a clear lag between initial storm inputs and the onset of continuous groundwater discharge, followed by a gradual tapering of flow. Groundwater levels are plotted relative to local ground surface elevation, with a reference line at 0 m AMSL indicating the emergence threshold. Following the AR event on March 29, 2024, which delivered 31.50 mm of rainfall, shallow groundwater upwelling persisted until levels receded below the ground surface by April 18, 2024. Groundwater briefly re-emerged at the same location during two separate 24-hour periods on

May 5 and July 2, 2024, before remaining below the surface through at least December 31, 2024. The timing of these brief re-emergence events may be influenced by local irrigation, as adjacent properties have been observed watering during the dry season.

Together, these observations and data illustrate the complex interactions between extreme precipitation, artificial subsurface structures, and groundwater dynamics, providing critical insight into flood risks in urban coastal environments. A conceptual diagram of the Manzanita emerging groundwater is shown in **Figure 3.14**.

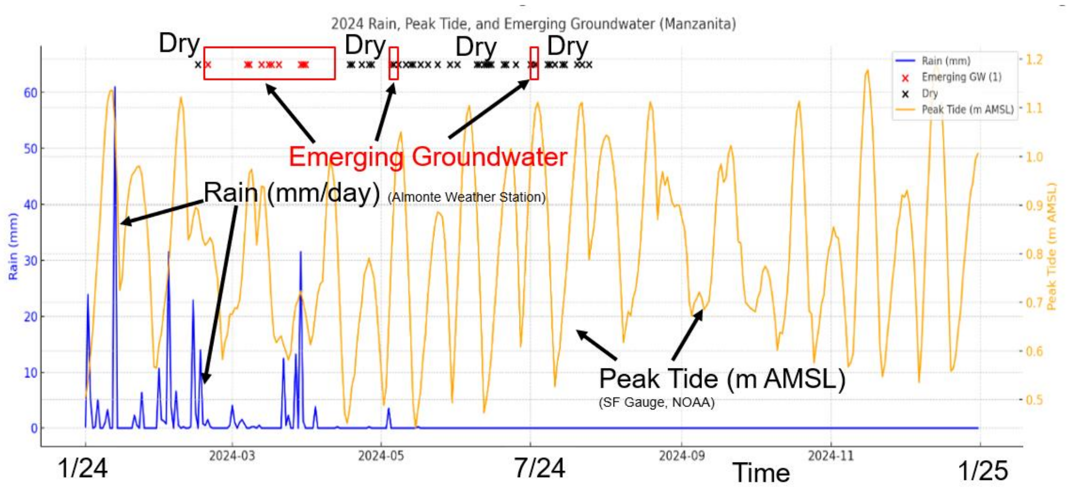

Figure 3.13: Daily rainfall (mm), peak tide (m AMSL), and emerging groundwater presence (black = dry, red = wet) in Manzanita, 2024.

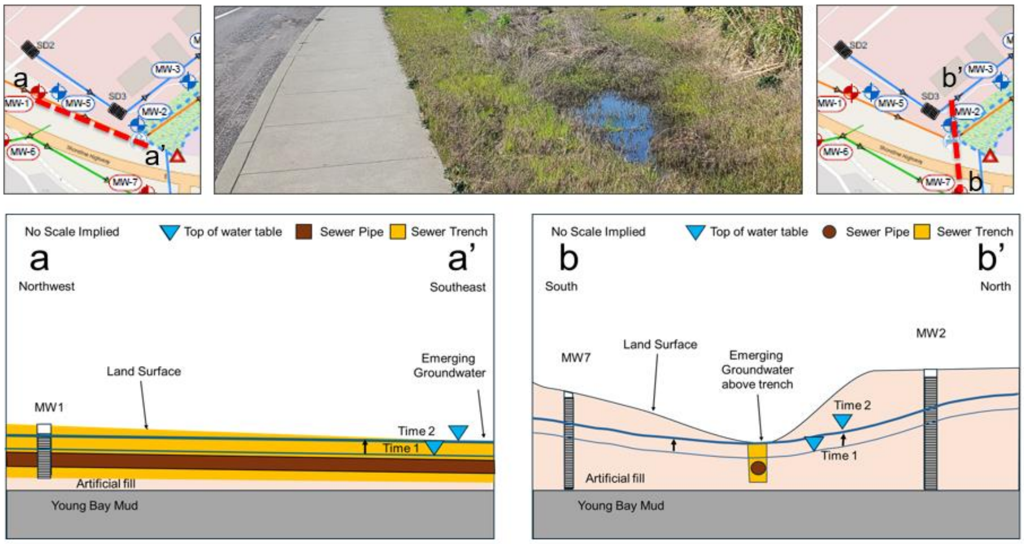

Figure 3.14: diagram of emerging groundwater, Manzanita, no scale implied

Manzanita, groundwater emergence was observed in 2024 within a low-lying area situated directly above a preferential flow pathway, specifically a sewer trench. The emerging groundwater was fresh water and not associated with HAT events, but rather several AR events. Emerging groundwater such as observed in Manzanita can lead to persistent surface saturation, increasing the likelihood of ponding, structural instability, and contaminant release from the subsurface.

3.4.2 Tamalpais Valley

Tamalpais Valley groundwater samples showed limited saltwater content, consistent with well placement away from tidal channels and outside preferential flow pathways, tidal inlet samples confirm that estuarine water can reach parts of the site during HAT events. Ternary mixing results show high saltwater contributions in both emerging groundwater (81.5%) and tidal inlet samples (80.8%), indicating episodic estuarine intrusion even in this inland setting. This suggests the presence of buried preferential pathways or low-permeability conduits that intermittently connect inland fill zones to tidal creeks. Isotopic depletion in emerging groundwater (−4.72‰ $\delta^{18}O$, −28.98‰ $\delta^{2}H$) reflects limited evaporation and recent meteoric recharge, while slightly enriched groundwater samples suggest longer residence times or minor evaporative mixing. Tidal inlet samples exhibited intermediate isotopic values, consistent with estuarine water diluted by meteoric input, and isotopically distinct from the more enriched Richardson Bay marine end member. The mixing patterns in Tamalpais Valley reflect a combination of tidal inflow and rain-influenced shallow groundwater. With 13.4% rainwater and 23.0% tap water contributions observed in groundwater samples, local recharge and possible anthropogenic inputs also play a role. Emerging groundwater in Tamalpais Valley ranged from brackish to tidally influenced. These findings underscore the complex hydrologic processes operating in low-lying inland zones and the importance of differentiating source contributions to guide appropriate flood mitigation strategies.

3.4.3 Atchison Village

Surface water samples in Atchison Village, initially considered potential indicators of emerging groundwater, exhibit more depleted $\delta^{18}O$ and $\delta^{2}H$ values ($\delta^{18}O$: −8.35 to −9.36‰) than local groundwater or crawlspace water, consistent with a rainwater origin. These samples also contain lower concentrations of chloride, sodium, and bicarbonate, and exhibit electrical conductivity values (172–312 μS/cm) below those of groundwater and generally comparable to crawlspace water. These characteristics suggest a surface-derived origin from direct rainfall or stormwater accumulation, rather than emerging groundwater. Clear isotopic separation among end members in Atchison Village further validates the mixing analysis: rainwater and tap water were strongly depleted, confirming their use as appropriate meteoric references, while groundwater, crawlspace water, and tidal inlet samples shared similar δ-values, highlighting their connection to the shallow aquifer. Surface water and sewer overflow fell in intermediate positions, reflecting their mixed meteoric and subsurface origins.

Geochemical and isotopic data indicate that both crawlspace water and sewer overflow in Atchison Village primarily reflect shallow groundwater. Crawlspace water closely matches local groundwater composition, averaging 41.7% saltwater, 27.0% rainwater, and 31.3% tap water, with elevated bicarbonate and moderate electrical conductivity. Isotopic signatures plot near groundwater values with minimal evaporative enrichment, confirming hydraulic connectivity to the shallow saturated zone during periods of high-water table. These results support the interpretation that crawlspace flooding arises from groundwater emergence rather than isolated leaks or surface runoff, serving as a direct indicator of subsurface flooding risk.

Sewer overflow samples exhibit nearly identical mixing proportions (41.6% saltwater, 25.1% rainwater, 33.3% tap water), further reinforcing a dual origin from infiltration/inflow (I&I) and groundwater intrusion. Their close alignment with groundwater and crawlspace water in both isotope and ternary plots suggests that groundwater likely enters the sewer system during high water table conditions, particularly following AR events. This highlights the importance of accounting for subsurface connectivity in adaptation planning, especially as sea level rise and extreme precipitation events intensify.

Compared to Manzanita and Tamalpais Valley, Atchison Village groundwater shows more balanced source contributions and a lower overall saltwater fraction. Groundwater, crawlspace water, surface water, and sewer overflow samples all plot along the local meteoric water line (LMWL), indicating minimal evaporation and a common meteoric origin. These waters reflect shallow subsurface interaction and recharge-dominated dynamics in poorly drained alluvium, rather than marine influence.

In contrast, tidal inlet samples show a strong marine signature (57.5% saltwater) and are compositionally distinct from crawlspace and sewer overflow samples. While these samples reflect estuarine backflow into open drainage channels during HAT events, Atchison Village wells remained fresh. This contrast supports the conclusion that flooding in Atchison Village is driven by groundwater rise and stormwater backflow, not by tidal intrusion into the shallow aquifer.

Groundwater emergence is an underrecognized but potentially significant contributor to surface flooding in low-lying coastal areas like Manzanita, as well as more inland sites such as Tamalpais Valley and Atchison Village. In Atchison Village, seasonal crawlspace flooding is linked to a rising water table and is likely to worsen with increasing storm intensity. Geochemical and isotopic data help distinguish between mixed water sources, including floodwater, enabling the identification of emerging groundwater and guiding appropriate engineering responses. While marine flooding may require shoreline defenses and stormwater can be managed with surface drainage, groundwater emergence demands subsurface solutions such as trench drains or dewatering systems. As sea levels continue to rise and extreme precipitation events become more frequent, accurately identifying the source of surface water will be critical for climate adaptation, infrastructure resilience, and public health protection in vulnerable coastal areas.

4 Prioritizing Contaminated Sites Vulnerable to Sea-level Rise and Groundwater Emergence Using DRASTIC Indexing Framework, San Francisco Bay Area, California, USA

Abstract

The San Francisco Bay Area is increasingly vulnerable to sea level rise, which can trigger both coastal flooding and shallow groundwater emergence, processes that elevate the risk of human exposure to industrial contaminants buried in artificial fill and coastal sediments. This study investigates whether a rapid, cost-effective indexing framework can be used to prioritize contaminated sites at risk from hydrologic changes driven by climate change. The analysis focused on sites projected to experience at least 1 m of sea level rise and where groundwater lies within three meters of the land surface. Fourteen geographically distributed sites were selected based on the presence of volatile organic compounds, which are highly soluble, mobile in groundwater, and pose significant vapor intrusion risks. Trichloroethylene and tetrachloroethylene were used as proxy contaminants due to

their widespread occurrence and relevance to legacy pollution in the region.

To assess site vulnerability, a multi-tiered, index-based framework was developed. The DRASTIC index provided a baseline characterization of hydrogeologic vulnerability. To address additional risk dimensions not fully captured by DRASTIC, three supplementary indices were created: the Site Characteristics Index, the Contaminant Characteristics Index, and the Inundation Vulnerability Index. These represent site-specific hydrogeologic conditions, including DRASTIC, contaminant persistence and mobility, and flood exposure, respectively. Bivariate correlation analysis among these indices was used to identify and rank high-priority sites, those most vulnerable to sea level rise, shallow groundwater rise, and potential mobilization of subsurface contaminants. A z-score transformation was applied to standardize each index, enabling direct comparison and the development of composite rankings based on both predefined and data-driven weights. The strong correlation between the two ranking approaches ($R^2 = 0.754$) demonstrates the reliability of the framework. This structured assessment supports evidence-based prioritization of high-risk sites, helping to optimize the allocation of investigation and mitigation resources in response to increasing threats from sea level rise and climate-driven flooding.

4.1 Introduction

The intersection of sea level rise (SLR), groundwater rise, and public health risks in the San Francisco Bay Area is increasingly concerning, particularly as rising water tables and changing biogeochemistry can mobilize buried contaminants in shallow groundwater and contribute to overland tidal flooding (Cushing et al., 2023). Beyond SLR and groundwater rise, urban preferential flow pathways, such as sewer trenches and other underground infrastructure, can alter groundwater flow patterns, potentially creating new pathways for human and environmental exposure to buried contaminants (Hill et al., 2023). The Greenaction (2023) report *Ticking Time Bomb* highlights the social vulnerability concerns of SLR, and groundwater rise in the area, emphasizing the disproportionate risks faced by communities near contaminated sites and highlighting 50 environmental case studies in various states of investigation and remediation. Rather than being a comprehensive list of all contaminated sites potentially affected by SLR, the report illustrates the spatial diversity, contaminant variety, and differing cleanup statuses of the selected sites. Sites where industrial facilities and landfills have been constructed on reclaimed wetland where artificial fill was emplaced are particularly vulnerable to contaminant transport. Indeed, an estimated 85.2 percent of wetlands around San Francisco Bay have disappeared (Brophy et al., 2019) since the 1800s (**Figure 4.1a**) and industrial facilities and landfills were commonly developed on or near artificial fill placed on former tidal flat and tidal marsh deposits (SFEI, 2017, 2021). Together, these factors show that many contaminated sites in the region are situated in low-lying, geologically altered areas highly susceptible to water table rise and overland flooding.

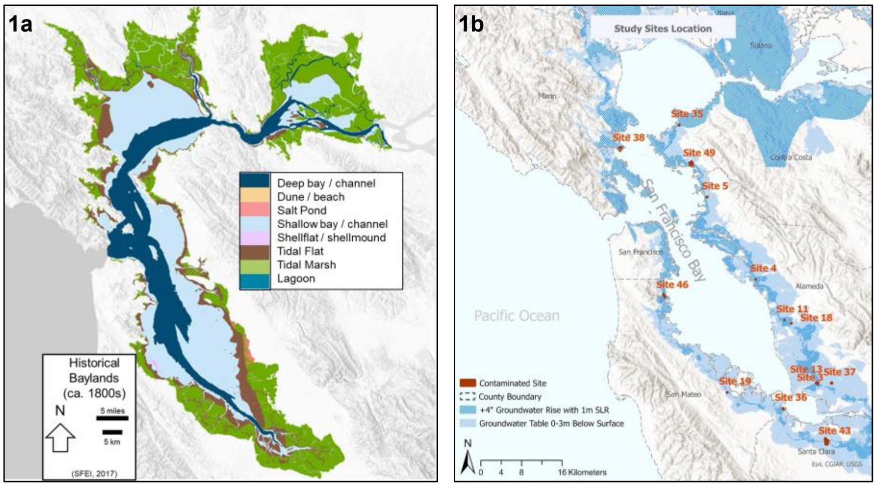

Figure 4.1: a) Historic Baylands in San Francisco Bay (modified after SFEI, 2017). b) Study site locations on basemap of groundwater rise with the red digits referring to the Greenaction (2023) site numbers (modified after Hill et al., 2023 (basemap), based on database by Befus et al., 2020)

The escalating risks of coastal flooding, groundwater inundation, and contaminant migration in the San Francisco Bay Area due to SLR were underscored in Hill et al 2023, in response to modeling from Befus et al 2020. The Befus et al (2020) study modeled the mechanisms by which rising water tables, driven by SLR, can exacerbate flooding. These findings highlight the need for proactive assessment and mitigation strategies to address the compound flooding threats posed by climate change in vulnerable coastal settings. Hill et al. (2023) also emphasized the interconnectedness of groundwater, surface water, and infrastructure vulnerabilities, a critical lens for understanding risk in dense, urbanized regions such as the San Francisco Bay Area. An empirically-based rapid assessment method (Plane et al. (2019) identified potential groundwater flooding hotspots as sea levels rise, focusing on how these hazards intersect with vulnerable infrastructure. The approach provides a foundation for assessing urban flooding risks, which is particularly relevant to the San Francisco Bay

Area's buried contaminants and dense network of buried urban utility trenches, which create preferential flow pathways (PFPs). The hydrologic responses of shallow groundwater to SLR are profiled by May et al. (2020), which uses a simple 1:1 estimate of how changes could influence contaminant emergence at the ground surface. Using this broad estimate of groundwater rise in various SLR scenarios, May et al. (2020) offer an initial assessment of the vulnerability of contaminated sites to emergent groundwater in the City of Alameda, California, an East Bay community. Expanding on earlier work by incorporating the effects of extreme weather events (e.g., atmospheric rivers) on groundwater systems, May et al. (2022) highlighted how these extreme events exacerbate SLR-induced vulnerabilities, demonstrating the compounded risks of flooding and groundwater rise for coastal communities.

Identifying the locations most likely to experience groundwater inundation, Plane and Hill (2017) mapped minimum depths to groundwater in a coastal case study of Alameda County in California with the largest number of coastal contaminated sites in the San Francisco Bay area. Using data sourced from GeoTracker, California's site cleanup database which includes groundwater level data, Plane and Hill provide critical interpretation of this data to identify areas most likely to experience groundwater inundation under SLR scenarios. The findings are essential for identifying regions with increased contaminant mobilization risks, particularly where shallow groundwater intersects with industrial pollution. Exploring how SLR impacts urban networks such as wastewater and stormwater infrastructure, Hummel et al. (2018) used Plane et al.'s 2019 empirical groundwater depth estimates to focus on the potential for contaminant release from overwhelmed urban wastewater treatment systems. The paper draws attention to infrastructure vulnerabilities such as increased inflow and infiltration that can amplify the risks of contaminant exposure during extreme weather events in coastal areas. Publicly owned treatment works (POTWs) in areas with submerged headworks already face increased wastewater volumes and due to infiltration and inflow. SLR exacerbates these issues by further increasing wastewater volumes. Hill et al. (2023) provided a conceptual model and comprehensive analysis of contaminated sites in the San Francisco Bay Area and Superfund sites nationally that are at risk from SLR and groundwater rise. They also identified a significant association between administratively active ("open") sites and community social vulnerability. These findings underscore the urgency of developing methods to prioritize mitigation efforts and protect public health in high-risk zones.

Hill et al. (2023) identified 13 contaminated Superfund sites in the San Francisco Bay Area and 5,282 additional sites where soil and/or groundwater currently or historically contained volatile organic compounds (VOCs), toxic metals, radioisotopes, and other contaminants, all of which may be at risk of mobilization by rising groundwater under a 1.0 m SLR scenario. Additionally, the study revealed that groundwater rise may impact twice the land area affected by direct coastal inundation (Befus et al., 2020), reinforcing the urgency of planning for emerging groundwater threats. The potential economic impacts of contaminant mobilization include increased remediation costs, decreased property values, and costs associated with human health impacts. Infrastructure may be damaged by corrosive contaminants in rising groundwater, leading to additional maintenance, operations, and replacement costs. Furthermore, the loss of usable land due to contamination and flooding can have significant economic implications for coastal communities.

Originally developed by the National Water Well Association (now the National Ground Water Association) for the U.S. Environmental Protection Agency, the DRASTIC method offers a widely used, cost-effective approach for assessing the intrinsic vulnerability of groundwater systems (Aller et al., 1987). It evaluates hydrogeologic settings based on seven core parameters: depth to water, net recharge, aquifer media, soil media, topography, impact of the vadose zone, and hydraulic conductivity. Each parameter is assigned a qualitative rating and weight, and the final vulnerability index is calculated as a weighted sum. This structure allows for straightforward application using readily available geospatial and geological data, making the method well-suited for regional-scale assessments (Lindström, 2005).

DRASTIC indexing was selected for this study based on its simplicity, transparency, and global recognition as a standardized groundwater assessment framework. Its integration with GIS further enhances its utility for spatial planning and environmental screening (Patel et al., 2022; Barbulescu, 2020; Fannakh and Farsang, 2022). The model has been successfully applied across a range of environmental contexts, including studies in Greece (Kirlas et al., 2023), Pakistan (Maqsoom et al., 2021), India (Bera et al., 2021), China (Wang et al., 2012), Tunisia (Chandoul et al., 2015), Iran (Malakootian and Nozari, 2020), Turkey (Soylu et al., 2022), Italy (Ducci and Sellerino, 2022), and Malaysia (Shirazi et al., 2013).

In the San Francisco Bay Area, DRASTIC has been used to assess groundwater vulnerability to various contaminants. Pierno (1999) evaluated pesticide and nitrate risks in South Bay aquifers. Mohr (2007) assessed chlorinated solvent contamination, particularly PCE and TCE, linked to historical dry-cleaning sites. Todd and Kennedy-Jenks (2010) expanded on these studies by using a modified DRASTIC model integrated with GIS to evaluate threats from PCE, TCE, and nitrate contamination, informing long-term water resource protection. Jurek (2014) applied a similar method in southern Alameda County to examine PCE risks in the Niles Cone Groundwater Basin. Collectively, these efforts confirm the utility of DRASTIC as a regional screening tool for groundwater vulnerability in both agricultural and industrial contexts.

While the DRASTIC framework provides a foundational method for assessing intrinsic groundwater vulnerability, it requires adaptation to reflect the dynamic conditions introduced by sea level rise, flooding, and extreme weather. The standard model assumes static hydrologic conditions, vertical contaminant migration from the surface, and homogeneous subsurface materials (Aller et al., 1987). These assumptions limit its ability to characterize coastal systems where contamination may originate from buried sources, be mobilized by lateral groundwater shifts, or be influenced by saltwater intrusion and tidal fluctuations (Jiao & Post, 2019). Critics have also noted challenges with calibration, sensitivity, and input data variability (NRC, 1993; Rosen, 1994; Rupert, 2001). In response to these limitations, this study develops an enhanced DRASTIC-based screening method that can serve as a reliable tool for prioritizing high-risk sites vulnerable to SLR for future investigation and mitigation.

4.2 Materials and Methods

To address gaps in traditional vulnerability assessments, this study introduces three supplementary indices and associated factors that expand the DRASTIC framework's applicability to dynamic coastal systems. These indices capture: (1) contaminant characteristics, such as solubility, mobility, diversity of contaminant classes, concentration levels, and persistence, based on fate and transport principles documented by Freeze and Cherry (1979) and environmental chemical characteristics such as solubility and mobility described by Schwarzenbach et al. (2016); (2) site characteristics, such as depth to water, surface–subsurface interaction, migration potential, and permeability, drawing from foundational transport and hydrogeologic concepts developed by Freeze and Cherry (1979), Fetter (1981), and Heath (2004); and (3) coastal inundation vulnerability factors, including land use patterns, projected sea level and groundwater rise rates, surface elevation, and proximity to the shoreline, based on the work of Rotzoll and Fletcher (2013), Jiao and Post (2019), Befus et al. (2020), Hill et al., (2023) and Habel et al. (2024).

A targeted selection of contaminated sites is made based on the presence of specific contaminants, their location in areas with shallow groundwater, within three m of the land surface, and exposure to projected sea level rise (SLR) of one m by 2100. This SLR projection is based on intermediate to high CO_2 emissions scenarios outlined by the Intergovernmental Panel on Climate Change (IPCC), specifically RCP 4.5 and RCP 8.5 (IPCC, 2021). The *Ticking Time Bomb* report by Greenaction (2023) identifies 50 contaminated sites in the region, documenting a wide array of hazardous substances, including radioactive materials, chlorinated solvents (e.g., TCE and PCE), petroleum hydrocarbons (e.g., benzene, toluene, gasoline, and diesel), pesticides, toxic metals (e.g., lead, arsenic, and mercury), polycyclic aromatic hydrocarbons (PAHs), and polychlorinated biphenyls (PCBs). To prioritize these sites based on human health risks, specific contaminants were selected based on their toxicity and mobility in groundwater. Specifically, VOCs were chosen as proxy contaminants due to their high solubility, mobility, and elevated potential to have near-term impacts on human health via the vapor intrusion pathway that can allow uphill transport to indoor air via pipes and utility trenches (Riis et al., 2010; Roghani et al., 2018; Beckey and McHugh, 2020).

Many VOCs are characterized by their high-water solubility and mobility, making them a dominant class of groundwater contaminants at both former and active industrial facilities in the study area. For this study, seven VOCs were initially selected as possible proxy compounds to represent target contaminant concentrations. This group includes chlorinated solvents such as carbon tetrachloride (CT), tetrachloroethylene (PCE), dichloroethane (DCA), dichloroethene (DCE), trichloroethylene (TCE), and 1,1,1-trichloroethane (1,1,1-TCA). The selection of these chemical proxies was based on prior research identifying the most used and released VOCs over the past several decades (**Table 4.1**). Chlorinated VOCs, including PCE, TCE, DCE, DCA, and 1,1,1-TCA, persist in groundwater due to their low biodegradability, high density, and resistance to natural attenuation. Unlike non-chlorinated VOCs such as benzene, toluene, ethylbenzene, and xylenes (BTEX), which degrade more readily in aerobic conditions. Specifically, PCE and TCE can persist for decades due to their low reactivity in groundwater. Indeed, moderate concentrations of PCE and TCE were detected in approximately 5% of the primary aquifer systems in the San Francisco area (Mathany et al., 2009; Ray et al., 2013). Given their prevalence across the studies listed in **Table 4.1**, PCE and TCE were selected as contaminant proxies for potential mobilization within shallow, unconfined groundwater.

Table 4.1: Studies of commonly used VOCs

Reference	Commonly used VOCs
Moran et al., 2007	1,1,1-TCA, chloroform, DCA, DCE, methylene chloride, PCE, and TCE
Mackay and Cherry, 1989	1,1,1-TCA, CT, PCE, and TCE
Schaumburg, 1990	1,1,1-TCA, CT, PCE, and TCE
Rivett et al., 1990	1,1,1-TCA, CT, PCE, and TCE
Henschler, 1994	PCE and TCE
Volpe et al., 2007	PCE and TCE
Ray et al., 2009 and 2013	PCE and TCE

4.2.1 Study Area

We selected 14 non-military sites (see **Figure 4.1b**) from the *Greenaction* (2023) report, all of which identified chlorinated solvents, specifically TCE and/or PCE, as contaminants of concern. All sites were in areas where groundwater is predicted to rise with 1-m SLR scenario, and the location will either be inundated by rising tidal water or have groundwater within 3-m of the land surface.

4.2.2 Calculating the DRASTIC Index

DRASTIC assigns qualitative ratings and weights to parameters from readily available databases or lithologic estimates to generate an index value for site comparison (Lindström, 2005). This study utilized the original DRASTIC rating and weighting system (Aller et al., 1987)

The DRASTIC index (DI) is calculated following **Equation** 1:

$$DI = D_r*D_w + R_r*R_w + A_r*A_w + S_r*S_w + T_r*T_w + I_r*I_w + C_r*C_w \quad (1)$$

where, D_i represents the DRASTIC index, and the capital letters D,R,A,S,T,I,C refer to the seven hydrogeologic parameters: Depth to water, Recharge, Aquifer media, Soil media, Topography, Impact of the vadose zone, and hydraulic Conductivity of the aquifer. Subscripts r and w denote the parameter's rating and weighting, respectively, as defined by Aller et al. (1987). The DRASTIC variable rating system is summarized in **Table 4.2**.

Substituting the specific weighting factors defined by Aller et al. (1987), the DRASTIC index is calculated following Equation 2:

$$DI = D_r*5 + R_r*4 + A_r*3 + S_r*2 + T_r*1 + I_r*5 + C_r*3 \quad (2)$$

where, the weightings (5, 4, 3, 2, 1, 5, and 3) correspond to the respective parameters D,R,A,S,T,I,C. This standardized approach ensures that each parameter contributes to the overall index in proportion to its influence on groundwater vulnerability. The weighting factors used by the DRASTIC method (Aller et al., 1987) are predefined in the DRASTIC framework and were established through expert consensus and empirical studies to reflect how strongly each parameter affects the potential for contaminant transport through the subsurface.

Table 4.2: DRASTIC variable rating system based on Aller et al. (1987) as presented in Mohr, 2007.

Depth to Water	
Feet bgs	**Rating**
0-5	10
5-15	9
15-30	7
30-50	5
50-75	3
75-100	2
100+	1

Aquifer Media	
Type	**Rating**
Massive Shale	1-3 (2)
Metamorphic/Igneous	2-5 (3)
Weathered Metamorphic/Igneous	3-5 (4)
Glacial Till	4-6 (5)
Bedded Sandstone, Limestone and Shale Sequences	5-9 (6)
Massive Sandstone or Limestone	4-9 (6)
Sand and Gravel	4-9 (8)
Basalt	2-10 (9)
Karst Limestone	9-10 (10)

Topography	
Percent slope	**Rating**
0-2	10
2-6	9
6-12	5
12-18	3
18+	1

Hydraulic Conductivity	
gpd/ft	**Rating**
1-100	1
100-300	2
300-700	4
700-1,000	6
1,000-2,000	8
2,000+	10

Net Recharge	
in/yr	**Rating**
0-2	1
2-4	3
4-7	6
7-10	8
10+	9

Soil Media	
Type	**Rating**
Thin or Absent	10
Gravel	10
Sand	9
Peat	8
Shrinking and/or Aggregated Clay	7
Sandy Loam	6
Loam	5
Silty Loam	4
Clay Loam	3
Muck	2
Non-shrinking / Non-aggregated Clay	1

Impact of Vadose Zone	
Type	**Rating**
Confining Layer	1 (1)
Silt/Clay	2-6 (3)
Shale	2-5 (3)
Limestone	2-7 (6)
Sandstone	4-8 (6)
Bedded Limestone, Sandstone, Shale	4-8 (6)
Sand and Gravel with Significant Clay	4-8 (6)
Metamorphic/Igneous	2-8 (4)
Sand and Gravel	6-9 (8)
Basalt	2-10 (9)
Karst Limestone	8-10 (10)

Source: USEPA, DRASTIC, May 1987.
Ratings for Aquifer Media and Impact of Vadose Zone are provided as a range; any value within the range can be used; values shown in parentheses are typical values.
bgs = below ground surface
gpd/ft = gallons per day per foot
in/yr = inches per year

Detailed lithologic descriptions from three to five soil boring logs per study site were used to characterize four of the seven DRASTIC parameters: aquifer media, soil media, hydraulic conductivity, and the impct of the vadose zone. These borehole logs provided critical information on sediment texture, stratigraphy, and permeability variations. Net Recharge estimates were based on precipitation data from local weather stations, in conjunction with soil infiltration potential and land cover characteristics. Depth to water and contaminant concentration data were obtained from current state and regional regulatory agency databases. Topography was assessed using high-resolution topographic maps and digital elevation models (DEMs), supported by web-based terrain analysis tools.

The integration of parameter ratings with the standardized DRASTIC weights allowed for the calculation of a composite index score at each site, facilitating a comparative assessment of groundwater vulnerability across diverse hydrogeologic and land use settings in the study area. As rainfall infiltration rates may not be readily available, especially in urban areas with varied surface permeability, an alternate net recharge calculation was described by Piscopo (2001) and Chitsazan and Akhtari (2009) and incorporates slope, rainfall, and soil permeability. The alternative net recharge parameter is calculated following **Equation 3**:

$$R = \text{Slope (\%)} + \text{Rainfall (mm/yr)} + \text{Soil Permeability (gpd/ft}^2\text{)} \tag{3}$$

Future SLR, groundwater rise and management actions such as widespread pumping of shallow groundwater in response to flooding significantly reshape the traditional concept of groundwater vulnerability by introducing dynamic hydrological changes that can mobilize previously stable buried subsurface contaminants. To address these evolving challenges, we developed a site-specific conceptual model integrating DRASTIC parameters with modifications for SLR, focusing on the unique threats posed by SLR, groundwater rise, and climate-driven impacts in coastal regions (**Figure 4.2a** and **4.2b**).

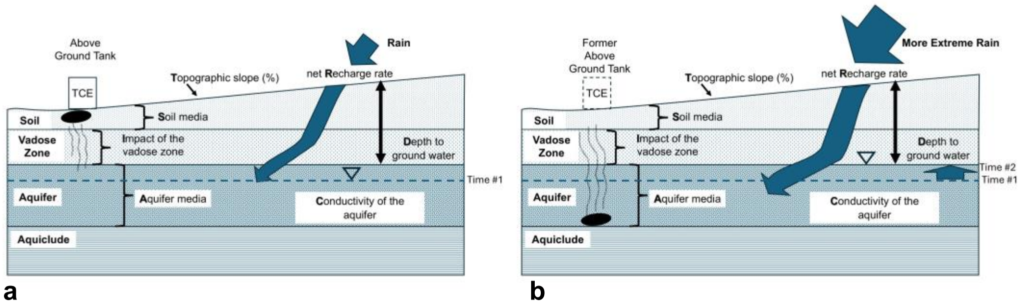

Figure 4.2: a) Conceptual model of the DRASTIC parameters at Time #1 (DRASTIC concepts by Aller et a., 1987); b) Updated conceptual model of the DRASTIC parameters at Time #2, with more extreme rain, and groundwater rise

4.2.3 Data Sources

For the DRASTIC parameters, vadose zone and aquifer information were obtained from boring logs available on the State Water Resources Control Board (SWRCB) GeoTracker website (https://geotracker.waterboards.ca.gov/) and the Department of Toxic Substances Control (DTSC) EnviroStor website (https://www.envirostor.dtsc.ca.gov/public/). Additional boring logs from liquefaction studies are available from the California Geological Survey. The United States Department of Agriculture (USDA) Natural Resources Conservation Service Web Soil Survey (https://websoilsurvey.nrcs.usda.gov/app/) provides soil data, drainage characteristics, and shallow subsurface information. The most recent groundwater monitoring reports from these sources provided data on the Highest Current Contaminant Concentration (HCCC), Depth to Water (DTW and the D in DRASTIC). Additional parameters were derived from topographic maps (USGS) for slope analysis (% slope), Surface Elevation (SE), and Distance to Water (DW). Annual precipitation data was sourced from NOAA rainfall records. To support the spatial analysis, site data from GeoTracker and groundwater depth estimates from Plane and Hill (2017) were used to evaluate which locations were most vulnerable to shallow groundwater inundation. Extreme weather and tidal flooding vulnerability were integrated by referencing SLR response studies such as Befus et al. (2020), May et al. (2022), and Hill et al. (2023), which provided empirical and modeled insight into groundwater rise, flood risk, and contaminant exposure under climate change scenarios.

4.2.4 Computing Supplementary Vulnerability Indices

To expand the DRASTIC framework for use with SLR, three supplemental indices were developed: the Site Characteristics Index, the Contaminant Characteristics Index, and the Inundation Vulnerability Index. A Some of the main parameters of the Supplementary Indices are summarized in **Figure 4.3**.

The Site Characterization Index (SCI) (**Table 4.3**) is a refinement of the traditional DRASTIC index, designed to incorporate the influence of surface material permeability (SMP). A direct comparison of SCI and DRASTIC across sites shows a very strong linear relationship ($R^2 = 0.93$, $p < 0.00001$), confirming that SCI is structurally aligned with DRASTIC. This high correlation reflects that SCI preserves the core hydrogeologic vulnerability components of DRASTIC, while also adjusting for surface-layer dynamics that may amplify or mitigate exposure risks. SCI is intended to represent hydrogeologic vulnerability including depth to water (D), vadose zone and recharge interactions (R, S, T, and I), aquifer characteristics (A and C), as well as an index of surface permeability. The Site Characteristics Index is calculated following **Equations 4 – 6:**

$$SCI = DI + SMP \tag{4}$$

$$DI = DTW_{rw} + SSIF_{rw} + CMP_{rw} \quad (5)$$

$$DI = (D*5) + ((R*4) + (I*5) + (S*2) + (T*1)) + ((A*3) + (C*3)) \quad (6)$$

where SCI is the site characteristics index; DI is the DRASTIC index, DTW is depth to water (the D in DRASTIC, with the same weighting factor); SSIF is the surface to subsurface interaction factors (the R, S, T, and I of DRASTIC). CMP is contaminant migration potential (the A and C in DRASTIC). The SMP is the surface material permeability based on the multi-resolution land characteristics (MRLC) consortium urban impervious data (MRLC.gov, 2024).

Table 4.3: Site Characteristics Index (SCI) rating and weighting factors

Depth to Water; max possible 50	**Surface and Subsurface Interaction Factors; max possible 116**	**Contaminant Migration Potential; max possible 60**	**Surface Material Permeability (SMP); based on MRLC, 2024); weighting of 3; max possible: 36**	
DTW	**SSIF**	**CMP**	**SMP**	**Rating**
D of DRASTIC with weighting established by Aller et al., 1987	R, S, T, and I of DRASTIC with weighting established by Aller et al., 1987	A and C of DRASTIC with weighting established by Aller et al., 1987	>80% area/site within class 1	9
			60% - 80% area/site within class 1 and 2	7
			40% - 60% area/site within class 1 and 2	5
			20% - 40% area/site within class 1, 2 and 3	3
			<20% area/site within class 1, 2 and 3	1

Conversion Table from SCI score weighted rating to 0-9 digit

From	**To**	**Digit**
243	262	9
219	242	8
195	218	7
171	194	6
147	170	5
123	146	4
99	122	3
75	98	2
51	74	1
27	50	0

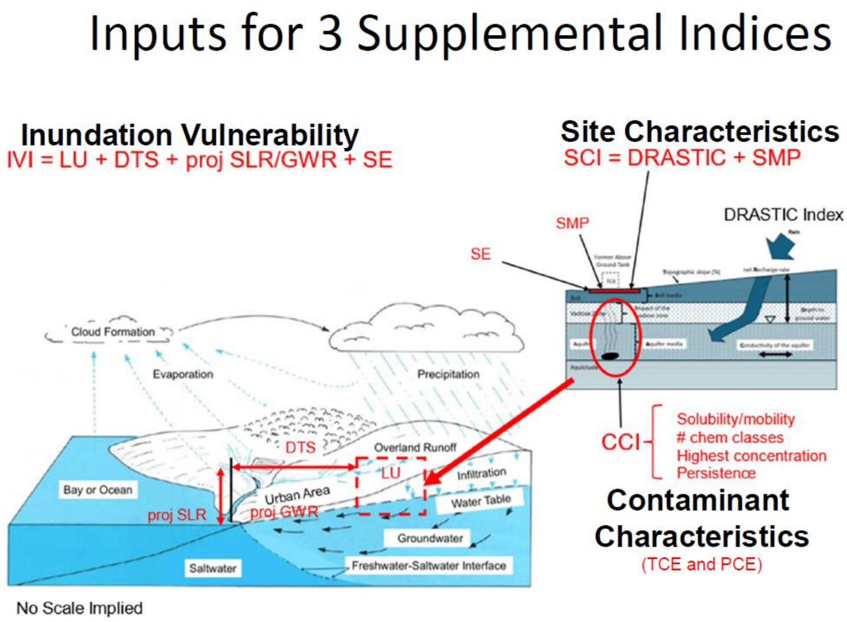

Figure 4.3: Schematic of the DRASTIC index as well as the three supplementary indices (CCI, SCI, and IVI). DTS = distance to shoreline, GWR = groundwater rise, SLR = sea level rise, SMP = surface material permeability, SE = surface elevation, LU = land use

The Contaminant Characteristics Index (CCI) **(Table 4.4)** relates to details about the buried contamination, as calculated following **Equation 7**:

$$CCI = CP*5 + NCC*4 + HCCC*5 + PC*5 \tag{7}$$

where, CCI is contaminant characteristics index, CP is a contaminant profile (solubility and mobility), NCC is number of contaminant classes, HCCC is highest current contaminant concentration, and PC is persistence of the contaminant. The numbers to the left of the parameters are the weighting factors. The weighting of the supplementary indices was determined by assessing the degree to which each parameter influences contaminant migration or human exposure. Parameters with a direct influence on contaminant transport were assigned the highest weight of 5, underscoring their critical role. Those factors with an indirect effect but important parameters received a weight of 4. In contrast, parameters that exert a moderate impact were weighted at 3, while those with a low level of influence were assigned 2, and those considered to have very little impact were given a weight of 1. This hierarchical weighting scheme is based on the DRASTIC weighting system (Aller et al., 1987) and ensures that each parameter's contribution to the overall index is proportionate to its significance in controlling subsurface contaminant mobility.

Table 4.4: Contaminant Characteristics Index (CCI) rating and weighting factors

Contaminant Profile (Solubility and Mobility); Weighting = 5		Contaminant Classes: (VOCs-PFOS, Hydrocarbons, Pesticides, Metals, PAHs); Weighting = 4		Contaminant Concentration: Primary contaminant (proxy for all contaminants), free product (dense non-aqueous phase liquid; DNAPL) with reductions in magnitude. Example of 1% of solubility for TCE and PCE and benzene in parts per million (ppm); Weighting = 5		Persistence of Contaminant (PC) in the Environment; Weighting = 5	
Solubility and Mobility	**Rating**	**Number of Classes**	**Rating**	**HCCC**	**Rating**	**PC**	**Rating**
Chlorinated Solvents (e.g., Tetrachloroethylene, Trichloroethylene): fluorinated organic compounds, radioactive wastes	10	5	10	TCE: 11 mg/L (DNAPL); PCE: 1.5 mg/L (DNAPL); benzene: 17.8 mg/L (LNAPL)	10	Very High Persistence; Per- and Polyfluoroalkyl Substances (PFAS, PFOS)	10
Gasoline and Petroleum Hydrocarbons-	8	4	8	TCE: 1.1 mg/L; PCE: 0.15 mg/L; benzene: 1.78 mg/L	8	High Persistence; PCBs, Chlorinated VOCs (TCE, PCE)	8
Pesticides (e.g., Atrazine, Glyphosate)	6	3	6	TCE: 0.11 mg/L; PCE: 0.015 mg/L; benzene: 0.178 mg/L	6	Moderately High Persistence; SVOCs	6
Toxic Metals (e.g., Lead, Mercury, Arsenic)	4	2	4	TCE: 0.011 mg/L; PCE: 0.0015 mg/L; benzene: 0.0178 mg/L	4	Moderate Persistence; Hydrocarbons, BTEX Compounds	4
Polycyclic Aromatic Hydrocarbons (PAHs)	2	1	2	TCE: 0.0011 mg/L; PCE: 0.00015 mg/L; benzene: 0.00178 mg/L	2	Moderately Low Persistence	3
Polychlorinated biphenyls (PCBs)	1			TCE: <0.0011 mg/L; PCE: <0.00015 mg/L; benzene: <0.00178 mg/L	1	Low Persistence; Non-Chlorinated VOCs	1
Unknown or no data available	*	Unknown or no data available	*	Unknown or no data available:	*	Unknown or no data available	*

Conversion table from CCI score weighted rating to a 0 - 9 digit

From	To	Digit
174	190	9
157	173	8
140	156	7
123	139	6
106	122	5
89	105	4
72	88	3

Inundation Vulnerability Index (IVI) is related to SLR and groundwater emergence (**Table 4.5**) is calculated following **Equation 8**:

$$IVI = LU*4 + PSGR*3 + SE*5 + DST*4 \quad (8)$$

where IVI is the sea level rise/groundwater rise vulnerability index, LU is the land use, PSGR is the projected sea level rise and groundwater rise, SE is the surface elevation above mean sea level (m), and DTS is distance to shoreline (m).

To operationalize the vulnerability assessment framework, the DRASTIC index was first applied to establish baseline hydrogeologic vulnerability across contaminated sites. This was then augmented by three supplementary indices, the CCI, SCI, and IVI to capture additional factors not addressed by the standard DRASTIC model. Two critical spatial parameters, surface elevation and horizontal distance to shoreline, were also incorporated to account for proximity-based exposure to SLR and groundwater emergence. Each parameter and index were evaluated using bivariate scatter plots to analyze site rankings across five distinct vulnerability relationships. For each comparison, the top four sites, approximately one quartile (28.6%) of the 14 assessed locations, were designated as high-priority based on relative values. These five sets of top-ranking sites were then aggregated to identify locations most consistently flagged as vulnerable across multiple dimensions. This qualitative, stepwise process offered a structured, transparent, and repeatable approach to identifying sites with compounded exposure to climate-driven hydrologic changes and contaminant mobilization risks, forming a data-driven foundation for future investigation and mitigation prioritization.

Table 4.5: Inundation Vulnerability Index (IVI) rating and weighting factors

Land Use (LU); Weighing = 4		Projected SLR/Groundwater Rise (PSGR); Weighting = 3		Surface elevation above mean sea level (m) (SE); Weighting = 5		Distance to Shoreline (DTS); Weighting = 4	
LU	**Rating**	**PSG**	**Rating**	**SE**	**Rating**	**DW**	**Rating**
High-risk industrial or former industrial	10	Extreme rise (>1 meter); water table near surface (0 to 1.5 m)	10	Extremely low or below water level; extreme flood risk (<0.5 m).	10	Very close to shoreline (<0.5 km); extreme risk from SLR and coastal flooding.	10
Mixed-use areas	8	High rise (0.5 to 1 meter); very shallow water table (1.5 m to 4.6 m)	8	Very low elevation (0.5-2.0 m); high flood risk.	8	Close to shoreline (0.5-1 km); high flood risk.	8
Residential redevelopments on former industrial lands	6	Moderate rise (up to 0.5 meters); shallow water table (4.6 m to 9.1 m)	6	Lower elevation (2.0-5.0 m); moderate flood risk.	6	Intermediate distance (1-2 km); moderate coastal flood risk.	6
Residential areas without flood protections	4	Minimal rise anticipated; moderate to deep water table (9.1 m - 15.2 m)	4	Moderate elevation (5.0-10.0 m); low flood risk.	4	Intermediate distance (1-2 km); moderate coastal flood risk.	4
Residential or vacant land with some level of flood defenses	2	No projected groundwater rise; deep water table (>15.2 m)	2	High elevation (>10.0 m above sea level or above flood stage of river), minimal flood risk.	2	Moderately far (2-5 km); low coastal flood risk.	2
Natural areas or well-protected land with effective flood defenses	1					Far from shoreline (>5 km); no impact from coastal flooding.	1
Unknown or no data available	*	Unknown or no data available	*	Unknown or no data available	*	Unknown or no data available:	*

Conversion Table from IVI score weighted rating to 0-9 digit

From	To	Digit
149	160	9
137	148	8
125	136	7
113	124	6
101	112	5
89	100	4
77	88	3
65	76	2
53	64	1

4.2.5 Index Analysis

To better understand the relative importance and influence of each parameter contributing to the three supplemental vulnerability indices, two complementary index analyses were performed: z-score standardization and One-At-a-Time (OAT) sensitivity analysis were used to evaluate parameter variability and assess how individual parameters affect overall index scores across sites.

Because the three supplementary indices have different maximum possible scores, **z-score standardization** was applied to allow for direct comparison. This transformation normalized all parameters to a common scale, with a mean of zero and a standard deviation of one, using the population standard deviation. Z-scores were calculated using **Equation 9**:

$$Z = (X - \mu)/\sigma \tag{9}$$

where z is the z-score, X is the raw individual parameter for each site, μ is the mean score across all 14 sites, and σ is the population standard deviation. z-scores were first calculated for the four parameters within each of the three supplementary indices. These standardized values enabled evaluation of the relative contribution of each parameter to overall index scores without altering their underlying distributions. For each site, standardized index scores were then averaged to produce a composite z-score, reflecting relative vulnerability across hydrogeologic, contaminant, and inundation-related index. Sites were subsequently ranked from highest to lowest composite z-score to support cross-site comparison and prioritization.

A single-parameter sensitivity analysis was performed to determine the influence of individual DRASTIC parameters on the overall vulnerability index.

The OAT method used is the Map Removal and Single-Parameter Sensitivity Approach (Lodwick et al., 1990), calculating the effective weight of each parameter using **Equation 10**:

$$W_{eff} = [(Pr_i \times Dr_i) / \sum_{i=1}^{n} (Pr_i \times Dr_i)] \times 100 \qquad (10)$$

Where, W_{eff} is the effective weight (%) of the parameter, Pr_i is the rating assigned to the parameter, Dr_i is the assigned to the parameter, $\sum_{i=1}^{n} (Pr_i \times Dr_i)$ is the sum of the products of ratings and weights for all parameters (i = 1 to n).

This equation calculates the influence of each parameter on the final index score. Theoretical weights are predefined values established by Aller et al. (1987). In contrast, the sensitivity analysis calculates the actual influence of each parameter on the final index score, revealing how much each parameter contributes in practice. This data-driven approach was used to identify which parameters had the greatest influence on vulnerability index scores at each site.

4.3 Results

Of the possible indexing points using the predefined weighting system, site characteristics (DRASTIC and SMP) represent 44% of the total possible indexing points, with contaminant characteristics (32%) and SLR and groundwater flooding potential (25%) (**Figure 4.4**).

4.3.1 Index Outputs (Raw Scores)

Raw scores for the DRASTIC, Site Characteristics Index (SCI), Contaminant Characteristics Index (CCI), and Inundation Vulnerability Index (IVI) were calculated for all 14 study sites. DRASTIC scores ranged from 72 to 135 across sites (**Table 4.5**). SCI values incorporated DRASTIC scores along with surface permeability data. CCI scores were based on contaminant-specific metrics including solubility, persistence, and mobility. IVI scores, reflected site-specific conditions related to flood exposure, including elevation, groundwater depth, and proximity to flood sources. Scatter plots of the DRASTIC index and the other indices show the vulnerabilities of the study sites (**Figure 4.5a to 4.5d**). The numbers on these figures correspond to site numbers used in the Greenaction (2023) report. The areas of higher priority reflect elevated vulnerability index scores on both axes. Each index (IVI, CCI, and SCI) was normalized to a 0–9 scale based on its respective value range, enabling consistent comparison and visualization across indices with differing units and magnitudes (**Figure 4.6**). The chart highlights the five most vulnerable Sites 49, 19, 46, 36, and 5.

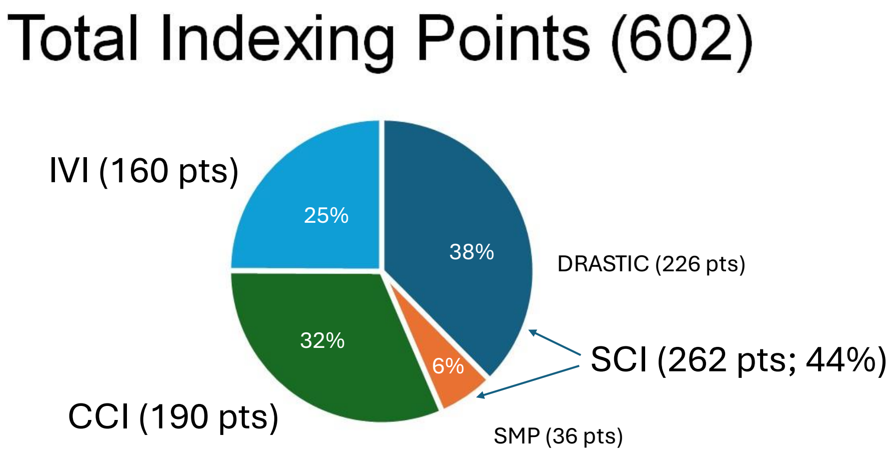

Figure 4.4: DRASTIC and supplemental indexing points

Table 4.6: Raw scores for DRASTIC, and three supplementary indices

Site Number	DRASTIC Index	Site Characteristics Index		Contaminant Characteristics Index		Inundation Vulnerability Index	
	Max Points	Max Points	Scale	Max Points	Scale	Max Points	Scale
	226 Weighted Points	262 Weighted Points	0-9 Index Digit	190 Weighted Points	0-9 Index Digit	160 Weighted Points	0-9 Index Digit
3	72	84	2	136	6	110	5
4	94	94	2	152	7	110	5
5	96	100	3	162	8	124	6
11	86	90	2	136	6	92	4
13	91	103	3	154	7	124	6
18	135	139	4	136	6	92	6
19	115	119	3	162	8	140	8
35	106	126	4	146	7	84	3
36	91	95	2	150	7	160	9
37	80	84	2	132	6	124	6
38	123	135	4	116	5	124	6
43	86	90	2	156	7	108	5
46	107	111	3	164	8	130	7
49	119	131	4	180	9	130	7

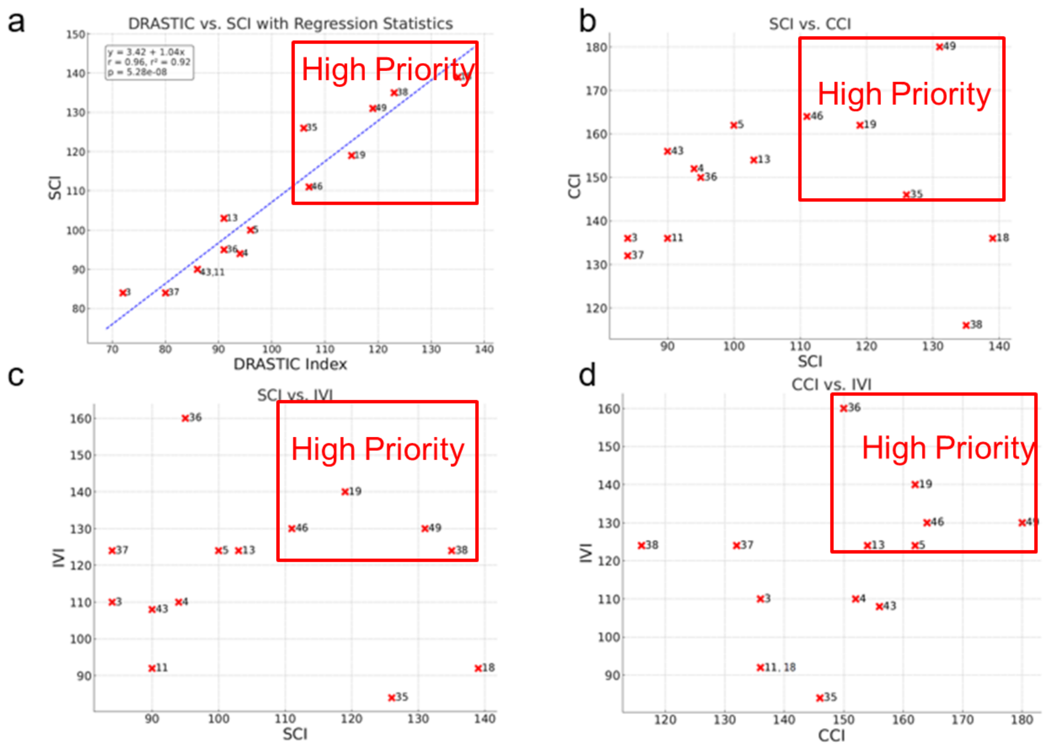

Figure 4.5: a) DRASTIC vs. SCI. b) SCI vs. CCI. c) SCI vs. IVI. d) CCI vs. IVI

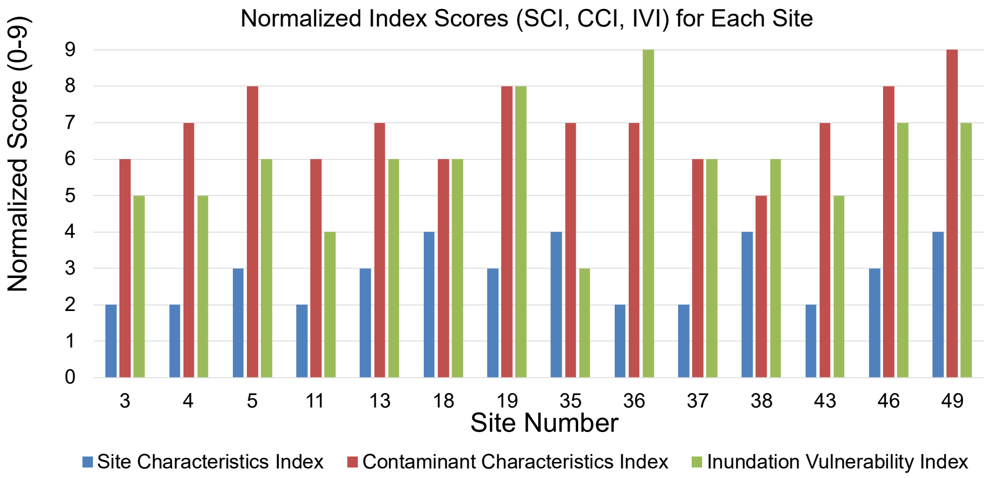

Figure 4.6: Site-level comparison of normalized hydrogeologic, contaminant, and inundation indices

A summary table (**Table 4.6**) presents the composite z-score rankings for all 14 sites across the three supplementary indices. For each index, both raw cumulative scores and their corresponding z-scores are displayed, enabling direct comparison across sites despite differences in index scale. For each index, z-scores were averaged by site to produce a composite z-score that reflects overall vulnerability across hydrogeologic, contaminant, and inundation-related dimensions. Sites were ranked from highest to lowest composite z-scores to support prioritization based on cumulative site vulnerability (see the two rightmost columns of the table). The composite ranking labeled CR-P is based on predefined weightings from Aller et al. (1987), while CR-DD reflects composite rankings using data-driven weightings developed in the sensitivity analysis (described below). The table highlights the range and variability of index scores across sites, as well as the relative influence of each index (SCI, CCI, and IVI) on the final composite rankings. Lower composite rank values indicate higher site vulnerability and thus greater priority for evaluation.

Z-scores were not applied to scatter plots of paired indices (e.g., SCI vs. CCI), as those visualizations are intended to show relationships between the original cumulative raw index scores rather than standardized values.

Table 4.7**:** Composite ranking of sites based on z-scoring for CCI, SCI, and IVI scoring.

Site No.	CCI	SCI	IVI	Z_ CCI	Z_ SCI	Z_ IVI	Z_ Comp.	Rank SCI	Rank CCI	Rank IVI	CR-P	CR-DD
3	136	84	110	-0.80	-1.24	-0.41	-0.82	13	10	9	13	11
4	152	94	110	0.21	-0.71	-0.41	-0.30	10	7	9	10	10
5	162	100	124	0.84	-0.38	0.31	0.25	8	3	5	5	5
11	136	90	92	-0.80	-0.92	-1.32	-1.01	11	10	12	14	14
13	154	103	124	0.33	-0.22	0.31	0.14	7	6	5	6	6
18	136	139	92	-0.80	1.70	-1.32	-0.14	1	10	12	8	12
19	162	119	140	0.84	0.63	1.12	0.86	5	3	2	2	3
35	146	126	84	-0.17	1.00	-1.73	-0.30	4	9	14	9	13
36	150	95	160	0.08	-0.65	2.14	0.52	9	8	1	4	2
37	132	84	124	-1.06	-1.24	0.31	-0.66	13	13	5	12	9
38	116	135	124	-2.07	1.48	0.31	-0.09	2	14	5	7	7
43	156	90	108	0.46	-0.92	-0.51	-0.32	11	5	11	11	8
46	164	111	130	0.97	0.20	0.61	0.59	6	2	3	3	4
49	180	131	130	1.98	1.27	0.61	1.29	3	1	3	1	1

4.3.2 Sensitivity Analysis

A sensitivity analysis was conducted to assess the relative influence of individual parameters within each index framework. For the DRASTIC index and each of the three supplementary indices, one input layer was removed at a time, and the index was recalculated without that parameter. This one-at-a-time (OAT) method enabled direct comparison between the original full index score and the modified score, helping to identify which parameters had the greatest effect on overall site vulnerability rankings in terms of percent contribution. The same procedure was applied to the Site Characteristics Index, Contaminant

Characteristics Index, and Inundation Vulnerability Index to evaluate the contribution of each component to the composite index score.

To quantify the sensitivity of each parameter, a sensitivity index (SI) was calculated using the following Equation 10:

$$SI = (I_{removed}/I_{total}) \text{ X } 100 \quad (10)$$

where SI is the sensitivity index for the removed parameter

I_{total} is the total weighted index score with all parameters included

$I_{removed}$ is the recalculated score with one parameter removed.

For DRASTIC, the depth to groundwater (D) provides the largest percent contribution to the index (46.4%) confirms the critical importance of this parameter in the DRASTIC index. It also validates its highest weight of 5, as defined by Aller et al. (1987), emphasizing its significant influence compared to other parameters.

A scatter plot comparing composite site ranks calculated using predefined weights versus data-driven weights (**Figure 4.7**) shows a strong correlation. These composite ranks reflect cumulative scores across the SCI, CCI, and IVI indices. The maximum possible scores, based on sensitivity analysis weightings, are 226 for DRASTIC and 100 each for SCI, CCI, and IVI.

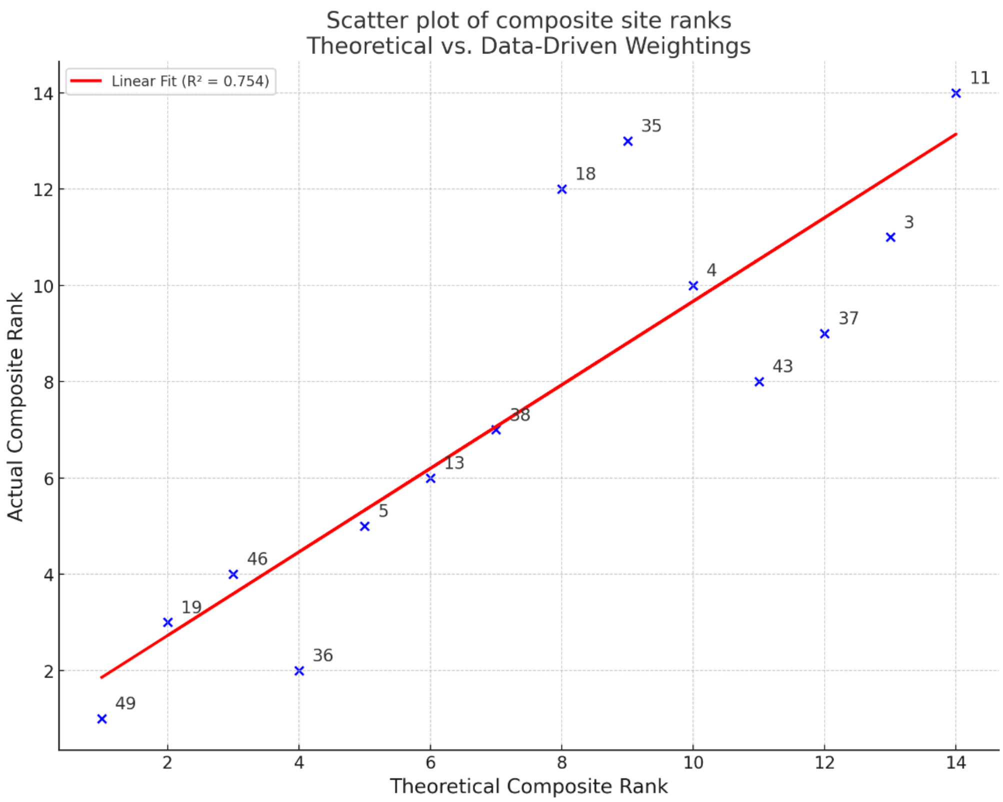

Figure 4.7: Scatter plot of composite site ranks based on cumulative SCI, CCI, and IVI scores using predefined and data-driven weightings

4.4. Discussion

This study addresses the growing need to evaluate contaminant mobilization risk in the context of SLR and groundwater emergence by integrating hydrologic, chemical, and spatial factors that are often overlooked in traditional groundwater vulnerability assessments. To overcome the limitations of the original DRASTIC model, developed for generalized inland environments and assuming vertical infiltration and relatively stable groundwater systems (Aller et al., 1987; NRC, 1993; Rupert, 2001), this study introduced three supplemental indices. SCI enhances DRASTIC by incorporating surface material permeability, which is especially relevant in urban and coastal landscapes. CCI quantifies contaminant solubility, persistence, and mobility, while IVI characterizes flood-related vulnerability, including marine overtopping, groundwater emergence, and stormwater flooding. Additional spatial parameters, such as surface elevation and proximity to shoreline, further contextualize site vulnerability. Together, these parameters enable capturing site dynamics such as groundwater mounding, vertical gradients, and saline intrusion (Michael et al., 2017; Jiao and Post, 2019).

The composite z-score analysis using the predefined weights (see **Table 4.7**) identified Sites 49, 19, and 46 as having the highest overall vulnerability based on the combined influence of SCI, CCI, and IVI. The elevated cumulative z-scores for these sites suggest that their vulnerability is not driven by a single dominant factor, but by consistent risk across all three indices. When summing their rankings across SCI, CCI, and IVI, Sites 49, 19, and 46 scored 7, 10, and 11 respectively, lower than all other sites—indicating higher cumulative vulnerability.

The z-score analysis also helped identify the relative strengths and weaknesses of each site across index parameters. Parameters with z-scores above zero contributed more than average to site vulnerability, while those below zero contributed less. Sites 49, 19, and 46 showed consistently elevated z-scores, resulting in composite ranks of 1, 2, and 3, respectively. In contrast, Sites 37, 3, and 11 exhibited mostly negative z-scores and were ranked 13 through 15, indicating the lowest overall vulnerability out of the sites investigated here.

The scatter plots (see **Figures 4.5b–4.5d**) comparing SCI, CCI, and IVI provide a multidimensional perspective on site vulnerability. Sites appearing in the upper-right quadrant of each bivariate plot represent areas where two distinct risk factors converge, noted within the red dashed lines as high priority. In the SCI vs. CCI plot, Sites 49, 19, and 46 show both high hydrogeologic sensitivity and high contaminant persistence/mobility. In the SCI vs. IVI plot, Sites 19, 49, and 38 combine shallow groundwater and permeable soils with high flood potential. In the CCI vs. IVI plot, Sites 49, 46, and 19 reflect the convergence of flood exposure and chemical persistence, suggesting a heightened risk of contaminant re-mobilization during storms or groundwater rise.

Sites 49, 19, and 46 were consistently identified as high-risk across all three scatter plots. Visual interpretation of their positions in high-risk quadrants is consistent with their high composite z-scores. They also share key characteristics, including low surface elevation, shallow groundwater, high concentrations of TCE or PCE, and coastal proximity.

Although the IVI and CCI indices both contribute to overall site vulnerability, statistical analyses reveal that they are largely independent. Paired scatter plots, Pearson correlation coefficients, and principal component analysis (PCA) indicated no strong linear relationship between IVI and CCI. PCA confirmed that these indices load onto separate principal components, reflecting their distinct underlying variables. IVI is based on physical and spatial site characteristics, such as surface elevation, distance to shoreline, and flood susceptibility, that change gradually across landscapes. In contrast, CCI reflects site-specific chemical and toxicological factors that can vary sharply due to local contaminant sources and land use history. As a result, site scores for CCI tend to cluster for sites with similar contaminants (e.g., chlorinated solvents), while IVI values are more widely distributed due to continuous spatial gradients. Some sites with high CCI are in physically less vulnerable areas, and vice versa, underscoring the importance of evaluating chemical and physical vulnerability dimensions independently when screening sites under future SLR and storm scenarios.

The sensitivity analysis reinforces the dominant role of the Depth to Water (D) parameter in both DRASTIC and SCI indices. In SCI, Depth to Water contributed 63.11% of the total sensitivity, underscoring its critical role in contaminant transport, especially in shallow groundwater systems. In contrast, five DRASTIC parameters, Aquifer Media (A), Soil Media (S), Topography (T), Impact of the Vadose Zone (I), and Hydraulic Conductivity (C), each contributed 10% or less, indicating limited influence on site scores. While sensitivity analysis assumes parameter independence, many hydrogeologic variables are interrelated. For example, recharge, soil permeability, and aquifer conductivity often co-vary, which may influence parameter interpretation. Still, the results remain valuable for identifying influential factors and refining assessments, particularly in data-limited settings.

Theoretical weights from the original DRASTIC model (5, 4, 3, 2, 1, 5, 3) are based on expert judgment and assume uniform importance of parameters across different hydrogeologic settings (Aller et al., 1987). These weights are static and do not account for local variability. In contrast, data-driven weights capture how each parameter influences vulnerability within the specific study area. Discrepancies arise because some parameters, like Depth to Water, may exert more influence under certain site conditions, such as shallow water tables, impermeable soils, or high recharge zones, which are not always captured by predefined frameworks. The comparison between composite rankings based on predefined and data-driven weights (see **Figure 4.7**) shows a strong statistical relationship. Both Pearson and Spearman correlation coefficients were 0.868, with p-values < 0.001. The R^2 value of 0.754 indicates that 75% of the variation in actual rankings is explained by the predefined model. These results validate the use of predefined weights as a reliable starting point. Sites 49, 36, 19, 46, and 5 ranked as the five sites with the highest overall SLR vulnerability based on composite scores under both predefined and data-driven weights. The sites cluster in the lower left on **Figure 4.7**. However, several other sites shifted in vulnerability rank when data-driven weights were applied, reflecting site-specific conditions that deviate from standardized assumptions. While predefined weights offer consistency, data-driven weights improve accuracy by adapting to local conditions.

Although this study focused on 14 sites, the indexing methodology is scalable and can be extended to regional assessments using Geographic Information Systems (GIS). The framework is also adaptable to other contaminant classes, including petroleum hydrocarbons, metals, pesticides, radioactive contaminants, and fluorinated compounds, enhancing its utility for broader coastal risk evaluations. As coastal conditions continue to evolve with SLR and climate change, integrating hydrogeologic, contaminant, and flood vulnerability indices offers a comprehensive and efficient approach for assessing and prioritizing sites where multiple risk factors converge.

Bibliography

Abdullah, T.O., Ali, S.S., Al-Ansari, N.A., and Knutsson, S., 2016, Groundwater vulnerability using DRASTIC and COP models: Engineering, v. 8, p. 741–760, https://doi.org/10.4236/eng.2016.811067.

AEG (Association Engineering Geologists), 2018, Geology of cities of the world series, in Johnson, K.A., and Bartow, G.W., eds., Geology of San Francisco, California, United States of America: 61st Annual Meeting of the AEG and 13th International Association of Environmental & Engineering Geologists Congress, San Francisco, California, September 16–22, 2018, 189 p.

Akenji, V.N., Ako, A.A., Akoachere, R.A., and Hosono, T., 2015, DRASTIC-GIS model for assessing vulnerability to pollution of the phreatic aquiferous formations in Douala–Cameroon: Journal of African Earth Sciences, v. 102, p. 180–190, https://doi.org/10.1016/j.jafrearsci.2014.11.001.

Albinet, M., 1970, Vulnerabilite des nappes d'eau souterrune a la pollution (Groundwater vulnerability to contamination): Bureau de Recherches Geologiques et Minieres (BRGM), v. 70 SGN 325 HYD, p. 31.

Aller, L., Bennett, T., Lehr, J.H., Petty, R.H., and Hackett, G., 1987, DRASTIC: A standardized system for evaluating ground water pollution potential using hydrogeologic settings: Ada, Oklahoma, U.S. Environmental Protection Agency, EPA/600/2-87/035, 622 p.

Anderson, T.R., Fletcher, C.H., Barbee, M.M., Romine, B.M., Lemmo, S., and Delevaux, J.M.S., 2018, Modeling multiple sea level rise stresses reveals up to twice the land at risk compared to strictly passive flooding methods: Scientific Reports, v. 8, 14484, 14 p., https://doi.org/10.1038/s41598-018-32658-x.

ASTM International, 2005, Standard practice for classification of soils for engineering purposes (Unified Soil Classification System): West Conshohocken, Pennsylvania, ASTM International, D2487-17R25, 10 p.

Atwater, B.F., Conrad, S.G., Dowden, J.N., Hedel, C.W., MacDonald, R.L., and Savage, W., 1979, History, landforms, and vegetation of the estuary's tidal marshes, 1850-1980, in Fifty-eighth Annual Meeting of the Pacific Division of the American Association for the Advancement of Science, San Francisco, California, June 12–16, 1977: San Francisco State University, p. 347–385.

Atwater, B.F., Hedel, C.W., and Helley, E.J., 1977, Late Quaternary depositional history, Holocene sea-level changes, and vertical crustal movement, southern San Francisco Bay, California: U.S. Geological Survey Professional Paper 1014, 15 p.

Back, W., 1960, Hydrochemical facies and ground-water flow patterns in northern part of Atlantic Coastal Plain, hydrology of aquifer systems: U.S. Geological Survey Professional Paper 498-A, 50 p.

Back, W., 1961, Techniques for mapping of hydrochemical facies, in Short papers in the geologic and hydrologic sciences: U.S. Geological Survey Professional Paper 424-D, p. D380–D382.

Barbulescu, A., 2020, Assessing groundwater vulnerability: DRASTIC and DRASTIC-like methods: A review: Water, v. 12, no. 5, 22 p., https://doi.org/10.3390/w12051356.

Barlow, P.M., and Reichard, E.G., 2010, Saltwater intrusion in coastal regions of North America: Hydrogeology Journal, v. 18, no. 1, p. 247–260, https://doi.org/10.1007/s10040-009-0514-3.

Barron, O.V., Barr, A.D., and Donn, M.J., 2013, Effect of urbanisation on the water balance of a catchment with shallow groundwater: Journal of Hydrology, v. 485, p. 162–176, https://doi.org/10.1016/j.jhydrol.2012.04.027.

BCDC (Bay Conservation and Development Commission), 2020, Adapting to rising tides 2020. Adapting to rising tides Bay Area: Short report summary of regional sea level rise vulnerability and adaptation study: San Francisco, Bay Conservation and Development Commission and Metropolitan Transportation Commission/Association of Bay Area Governments, 36 p.

BCDC (Bay Conservation and Development Commission), 2016, San Francisco Bay tidal datums and extreme tides study: San Francisco, Final Report, 140 p.

Beckley, L., and McHugh, T., 2020, A conceptual model for vapor intrusion from groundwater through sewer lines: Science of the Total Environment, v. 698, 134283, https://doi.org/10.1016/j.scitotenv.2019.134283.

Befus, K.M., Barnard, P.L., Hoover, D.J., Finzi Hart, J.A., and Voss, C.I., 2020, Increasing threat of coastal groundwater hazards from sea-level rise in California: Nature Climate Change, v. 10, p. 946–952, https://doi.org/10.1038/s41558-020-0874-1.

Befus, K.M., Finzi Hart, J.A., Griswold, M., Hallenbeck, T., and May, C.L., 2019, Bay Area groundwater and sea level rise workshop summary: 13 p.

Beimeng, Q., Chongwei, C., and Yixing, Y., 2015: International Journal of Electrochemical Science, v. 10, p. 545–558.

Bera, A., Mukhopadhyay, B.P., Chowdhury, P., Ghosh, A., and Biswas, S., 2021, Groundwater vulnerability assessment using GIS-based DRASTIC model in Nangasai River Basin, India with special emphasis on agricultural contamination: Ecotoxicology and Environmental Safety, v. 214, 112085, https://doi.org/10.1016/j.ecoenv.2021.112085.

Bjerklie, D.M., Hay, L.E., and Markstrom, S.L., 2018, Watershed scale response to climate change—Feather River Basin, California: U.S. Geological Survey Fact Sheet 3054, 6 p., https://doi.org/10.3133/fs20183054.

Blake, M.C., Jr., Graymer, R.W., and Jones, D.L., 2000, Geologic map and map database of parts of Marin, San Francisco, Alameda, Contra Costa, and Sonoma Counties, California: U.S. Geological Survey Miscellaneous Field Studies Map MF-2337, scale 1:75,000, https://doi.org/10.3133/mf2337.

Bonneau, J., Fletcher, T.D., Costelloe, J.F., and Burns, M.J., 2017, Stormwater infiltration and the 'urban karst'—A review: Journal of Hydrology, v. 552, p. 141–150, https://doi.org/10.1016/j.jhydrol.2017.06.043.

Bordbar, M., Neshat, A., and Javadi, S., 2019, A new hybrid framework for optimization and modification of groundwater vulnerability in coastal aquifer: Environmental Science and Pollution Research, v. 26, p. 21808–21827, https://doi.org/10.1007/s11356-019-05469-4.

Bosserelle, A.L., Morgan, L.K., and Hughes, M.W., 2022, Groundwater rise and associated flooding in coastal settlements due to sea-level rise: A review of processes and methods: Earth's Future, v. 10, e2021EF002580, https://doi.org/10.1029/2021EF002580.

BMIPM (Bothin Marsh Initial Planning Memo), 2020, Evolving shorelines, initial planning memo: One Tam, Golden Gate National Parks Conservancy, 56 p.

Boyle, B., 2017, Groundwater vulnerability assessment for nitrate pollution in the Salinas Valley using a modified DRASTIC model [Master's thesis]: San Francisco, University of San Francisco, 59 p.

Brophy, L.S., Greene, C.M., Hare, V.C., Holycross, B., Lanier, A., Heady, W.N., O'Connor, K., Imaki, H., Haddad, T., and Dana, R., 2019, Insights into estuary habitat loss in the western United States using a new method for mapping maximum extent of tidal wetlands: PLoS ONE, v. 14, no. 8, e0218558, https://doi.org/10.1371/journal.pone.0218558.

Buddemeier, R., 1996, Dynamic interplay of saltwater intrusion and SGD, in Wong, T., 2008, Comprehensive monitoring of salt water intrusion and submarine groundwater discharge in coastal systems: United Nations Commission on Sustainable Development, UNCSD-16, May 16, 16 p.

Canfield, D.E., 2001a, Stable isotope geochemistry, in Biogeochemistry of sulfur isotopes: Washington, D.C., Mineralogical Society of America, v. 42, p. 607–636.

Canfield, D.E., 2001b, Isotope fractionation by natural populations of sulfate-reducing bacteria: Geochimica et Cosmochimica Acta, v. 65, no. 7, p. 1117–1124, https://doi.org/10.1016/S0016-7037(00)00584-6.

Cantrell, K.J., Kaplan, D.I., and Wietsma, T.W., 1995, Zero-valent iron for the in-situ remediation of selected metals in groundwater: Journal of Hazardous Materials, v. 42, no. 2, p. 201–212, https://doi.org/10.1016/0304-3894(95)00016-N.

Cartwright, I., Gilfedder, B., and Hofmann, H., 2014, Contrasts between estimates of baseflow help discern multiple sources of water contributing to rivers: Hydrology and Earth System Sciences, v. 18, no. 1, p. 15–30, https://doi.org/10.5194/hess-18-15-2014.

CCSF (City and County of San Francisco), 2016, San Francisco sea level rise action plan: San Francisco, 100 p.

Chandoul, I.R., Bouaziz, S., and Dhia, H.B., 2015, Groundwater vulnerability assessment using GIS-based DRASTIC models in shallow aquifer of Gabes North (South East Tunisia): Arabian Journal of Geosciences, v. 8, p. 7619–7629, https://doi.org/10.1007/s12517-014-1708-0.

Chapman, D., 1996, Water quality assessments—A guide to use of biota, sediments and water in environmental monitoring (2nd ed.): United Nations Educational, Scientific and Cultural Organization, World Health Organization, United Nations Environment Programme, 651 p.

Chappelle, F., 1993, Ground-water microbiology & geochemistry: New York, John Wiley & Sons, Inc., 424 p.

Chitsazan, M., and Akhtari, Y., 2009, A GIS-based DRASTIC model for assessing aquifer vulnerability in Kherran Plain, Khuzestan, Iran: Water Resources Management, v. 23, p. 1137–1155, https://doi.org/10.1007/s11269-008-9319-8.

Christensen, T.H., Bjerg, P.L., Banwart, S.A., Jakobsen, R., Heron, G., and Albrechtsen, H.J., 2000, Characterization of redox conditions in groundwater contaminant plumes: Journal of Contaminant Hydrology, v. 45, no. 3–4, p. 165–241, https://doi.org/10.1016/S0169-7722(00)00109-1.

Church, J.A., and White, N.J., 2011, Sea level rise from the late 19th to the early 21st century: Surveys in Geophysics, v. 32, no. 4–5, p. 585–602, https://doi.org/10.1007/s10712-011-9119-1.

Clark, I.D., and Fritz, P., 1997, Environmental isotopes in hydrogeology: Boca Raton, Florida, CRC Press, 328 p.

Cooper, H.H., Kohout, F.A., Henry, H.R., and Glover, R.E., 1964, Sea water in coastal aquifers: U.S. Government Printing Office, USGS Water Supply Paper 1613-C, 84 p.

Craig, H., 1961, Isotopic variations in meteoric waters: Science, v. 133, p. 1702–1703, https://doi.org/10.1126/science.133.3465.1702.

Cullimore, D.R., and Johnston, L.A., 2004, Inter-relationship between sulfate reducing bacteria associated with microbiologically influenced corrosion and other bacterial communities in wells: National Association of Corrosion Engineers (NACE), NACE 2004 meeting, New Orleans, Louisiana, 9 p.

Cushing, L., Ju, Y., Kulp, S., Depsky, N., Karasaki, S., Jaeger, J., Raval, A., Strauss, B., and Morello-Frosch, R., 2023, Toxic tides and environmental injustice: Social vulnerability to sea level rise and flooding of hazardous sites in coastal California: Environmental Science & Technology, v. 57, p. 7370–7381, https://doi.org/10.1021/acs.est.2c08781.

CW3E (Center for Western Weather and Water Extremes), 2023, The landfalling atmospheric rivers of water year (WY) 2023: Scripps Institution of Oceanography, 6 p.

Dettinger, M., 2011, Climate change, atmospheric rivers, and floods in California—A multimodel analysis of storm frequency and magnitude changes: Journal of the American Water Resources Association, v. 47, no. 3, p. 514–523, https://doi.org/10.1111/j.1752-1688.2011.00546.x.

Dettinger, M.D., Ralph, F.M., Das, T., Neiman, P.J., and Cayan, D.R., 2011, Atmospheric rivers, floods, and the water resources of California: Water, v. 3, no. 2, p. 445–478, https://doi.org/10.3390/w3020445.

Droycon Bioconcepts Inc., 2004, Biological activity reaction test BART user manual: 57 p.

Ducci, D., and Sellerino, M., 2022, A modified AVI model for groundwater vulnerability mapping: Case studies in southern Italy: Water, v. 14, 248, https://doi.org/10.3390/w14020248.

Duffield, G., 2019, Aquifer testing 101: Hydraulic properties representative values of hydraulic properties: 22 p.

El Yousfi, Y., et al., 2023, Pollution vulnerability of the Ghiss Nekkor alluvial aquifer in Al-Hoceima (Morocco), using GIS-based DRASTIC model: International Journal of Environmental Research and Public Health, v. 20, p. 49–92, https://doi.org/10.3390/ijerph20064992.

El-Aassar, A.-H., Hagagg, K., Hussien, R., Oterkus, S., and Oterkus, E., 2023, Integration of groundwater vulnerability with contaminants transport modeling in unsaturated zone, case study El-Sharqia, Egypt: Environmental Monitoring and Assessment, v. 195, 722, 13 p., https://doi.org/10.1007/s10661-023-11186-w.

Elder, W.P., 1998, Geology of the Golden Gate Headlands: U.S. Geological Survey Bulletin 2188, Chapter 3, 26 p.

European Commission, 2010, Technical background document on identification of mixing zones: Communication and Information Resource Centre for Administrations, Businesses and Citizens (CIRCABC), 34 p.

Fannakh, A., and Farsang, A., 2022, DRASTIC, GOD, and SI approaches for assessing groundwater vulnerability to pollution: A review: Environmental Sciences Europe, v. 34, 77, https://doi.org/10.1186/s12302-022-00656-6.

Ferguson, G., and Gleeson, T., 2012, Vulnerability of coastal aquifers to groundwater use and climate change: Nature Climate Change, v. 2, no. 5, p. 342–345, https://doi.org/10.1038/nclimate1413.

Fetter, C.W., 1980, Applied hydrogeology: Columbus, Ohio, Charles E. Merrill, 488 p.

Figuers, S., 1998, Groundwater study and water supply history of the East Bay Plain, Alameda and Contra Costa Counties, CA: Norfleet Consultants, prepared for The Friends of the San Francisco Estuary, 120 p.

Focazio, M.J., 2002, Assessing ground-water vulnerability to contamination: Providing scientifically defensible information for decision makers: Denver, Colorado, U.S. Geological Survey Circular 1224, 33 p.

Foppen, J.W., 2002, Impact of high-strength wastewater infiltration on groundwater quality and drinking water supply: the case of Sana'a, Yemen: Journal of Hydrology, v. 263, no. 1–4, p. 198–216, https://doi.org/10.1016/S0022-1694(02)00051-3.

Freeze, R.A., and Cherry, J.A., 1979, Groundwater (2nd ed.): Englewood Cliffs, New Jersey, Prentice Hall, 604 p.

Fry, N., and Steenson, R., 2019, User's guide: Derivation and application of environmental screening levels (ESLs), interim final, revision 1: San Francisco Regional Water Quality Control Board, 215 p.

Gat, J.R., 1996, Oxygen and hydrogen isotopes in the hydrologic cycle: Annual Review of Earth and Planetary Sciences, v. 24, p. 225–262, https://doi.org/10.1146/annurev.earth.24.1.225.

GEI (Geotechnical Consultants, Inc.), 2015, Coyote Creek Levee evaluation project geotechnical data report, Coyote Creek, Marin County, CA: Submitted to Marin County Flood Control and Water Conservation District, Project 140457-0, Rev. 1, 93 p.

GEI (Geotechnical Consultants, Inc.), 2016, Coyote Creek Levee evaluation project existing conditions levee evaluation and recommendations for improvements, Coyote Creek, Marin County, CA: Submitted to Marin County Flood Control and Water Conservation District, Project 1404570, 207 p.

Gershunov, A., Shulgina, T., Ralph, F.M., Lavers, D.A., and Rutz, J.J., 2017, Assessing the climate-scale variability of atmospheric rivers affecting western North America: Geophysical Research Letters, v. 44, no. 15, p. 7900–7908, https://doi.org/10.1002/2017GL074175.

Google Scholar, 2024, "DRASTIC groundwater vulnerability assessment" topic search, retrieved November 19, 2024.

Gornitz, V., Couch, S., and Hartig, E.K., 2001, Impacts of sea level rise in the New York City metropolitan area: Global and Planetary Change, v. 32, p. 61–88, https://doi.org/10.1016/S0921-8181(01)00150-3.

Govorcin, M., Bekaert, D.P.S., Hamlingtonm, B.D., Sangha, S.S., and Sweet, W., 2025, Variable vertical land motion and its impacts on sea level rise projections: Science Advances, v. 11, no. 5, 11 p., https://doi.org/10.1126/sciadv.adg3292.

Greenaction Staff, 2023, Ticking time bomb: Climate change and sea level and GWR, shoreline contamination, and environmental justice in the San Francisco Bay Area: San Francisco, California, Greenaction for Health and Environmental Justice, 173 p.

Habel, S., Fletcher, C.H., Rotzoll, K., El-Kadi, A.I., and Oki, D.S., 2019, Comparison of a simple hydrostatic and a data-intensive 3D numerical modeling method of simulating sea-level rise induced groundwater inundation for Honolulu, Hawai'i, USA: Environmental Research Communications, v. 1, 041005, https://doi.org/10.1088/2515-7620/ab21fe.

Habel, S., Fletcher, C.H., Anderson, T.R., and Thompson, P.R., 2020, Sea-level rise induced multi-mechanism flooding and contribution to urban infrastructure failure: Scientific Reports, v. 10, 3796, https://doi.org/10.1038/s41598-020-60762-4.

Habel, S., Fletcher, C.H., Barbee, M.M., and Fornace, K.L., 2024, Hidden threat: The influence of sea-level rise on coastal groundwater and the convergence of impacts on municipal infrastructure: Annual Review of Marine Science, v. 16, p. 81–103, https://doi.org/10.1146/annurev-marine-041723-112328.

Habel, S., Fletcher, C.H., Rotzoll, K., and El-Kadi, A.I., 2017, Development of a model to simulate groundwater inundation induced by sea-level rise and high tides in Honolulu, Hawaii: Water Research, v. 114, p. 122–134, https://doi.org/10.1016/j.watres.2017.02.035.

Hamdan, I., Al-Rawabdeh, A., and Al Hseinat, M., 2020, Groundwater vulnerability assessment for the corridor wellfield using DRASTIC and modified DRASTIC models: A case study of eastern Jordan: Open Journal of Geology, v. 10, p. 991–1008, https://doi.org/10.4236/ojg.2020.1010044.

Hauer, M.E., Evans, J.M., and Mishra, D.R., 2016, Millions projected to be at risk from sea-level rise in the continental United States: Nature Climate Change, v. 6, p. 691–695, https://doi.org/10.1038/nclimate2961.

Hay, C.C., Morrow, E., Kopp, R.E., and Mitrovica, J.X., 2015, Probabilistic reanalysis of twentieth-century sea level rise: Nature, v. 517, no. 7535, p. 481–484, https://doi.org/10.1038/nature14093.

Heath, R.C., 1983, Basic ground-water hydrology: U.S. Geological Survey Water-Supply Paper 2220, 86 p.

Henschler, D., 1994, Toxicity of chlorinated organic compounds: Effects of the introduction of chlorine in organic molecules: Angewandte Chemie International Edition, v. 33, p. 1920–1935, https://doi.org/10.1002/anie.199419201.

Heudorfer, B., Haaf, E., Stahl, K., and Barthel, R., 2019, Index-based characterization and quantification of groundwater dynamics: Water Resources Research, v. 55, p. 5575–5592, https://doi.org/10.1029/2018WR024418.

Hill, K., Hirschfeld, D., Lindquist, C., Cook, F., and Warner, S., 2023, Rising coastal groundwater as a result of sea-level rise will influence contaminated coastal sites and underground infrastructure: Earth's Future, v. 11, no. 9, 15 p., https://doi.org/10.1029/2022EF003285.

Hitchcock, C., Givler, R., DePascale, G., and Dulberg, R., 2008, Detailed mapping of artificial fills, San Francisco Bay Area, California, final technical report for U.S. Geological Survey National Earthquake Hazard Reduction Program Grant Number 07HQGR0078: 23 p.

Holleman, R.C., and Stacey, M.T., 2014, Coupling of sea level rise, tidal amplification, and inundation: Journal of Physical Oceanography, v. 44, no. 5, p. 1439–1455, https://doi.org/10.1175/JPO-D-13-0214.1.

Hoover, D.J., Odigie, K.O., Swarzenski, P.W., and Barnard, P., 2017, Sea-level rise and coastal groundwater inundation and shoaling at select sites in California, USA: Journal of Hydrology: Regional Studies, v. 11, p. 234–249, https://doi.org/10.1016/j.ejrh.2015.12.055.

Hopkins, L.D., 1977, Methods for generating land suitability maps: A comparative evaluation: Journal of the American Planning Association, v. 43, p. 386–400, https://doi.org/10.1080/01944367708977903.

Hummel, M.A., Berry, M.S., and Stacey, M.T., 2018, Sea level rise impacts on wastewater treatment systems along the US coasts: Earth's Future, v. 6, p. 622–633, https://doi.org/10.1002/2017EF000805.

Hwang, H.T., Jeen, S.W., Suleiman, A.A., and Lee, K.K., 2017, Comparison of saturated hydraulic conductivity estimated by three different methods: Water, v. 10, 125, https://doi.org/10.3390/w10020125.

IPCC (Intergovernmental Panel on Climate Change), 2021, Climate change 2021: The physical science basis. Contribution of Working Group I to the Sixth Assessment Report of the Intergovernmental Panel on Climate Change: Cambridge, UK, Cambridge University Press, 2391 p.

Ingraham, N.L., and Taylor, B.E., 1991, Light stable isotope systematics of large-scale hydrologic regimes in California and Nevada: Water Resources Research, v. 27, no. 1, p. 77–90, https://doi.org/10.1029/90WR01708.

Jha, M.K., Singh, A., and Nanda, G., 2017, Urbanization impacts on groundwater resources: A review: International Journal of Water, v. 11, no. 1, p. 37–60, https://doi.org/10.1504/IJW.2017.081107.

Jiao, J., and Post, V., 2019, Coastal hydrogeology: New York, Cambridge University Press, 403 p.

Jurek, A.C., 2014, Vulnerability of groundwater to perchloroethylene contamination from dry cleaners in the Niles Cone groundwater basin, southern Alameda County, CA [Master's thesis]: San Jose, California, San Jose State University, 67 p.

Kaushal, S.S., McDowell, W.H., Wollheim, W.M., Johnson, T.A.N., Mayer, P.M., Belt, K.T., and Pennino, M.J., 2015, Urban evolution: The role of water: Water, v. 7, no. 8, p. 4063–4087, https://doi.org/10.3390/w7084063.

Kendall, C., and McDonnell, J.J., eds., 2012, Isotope tracers in catchment hydrology: Amsterdam, Elsevier, 839 p.

Kennedy, C.D., Bataille, C., Liu, Z., Ale, S., VanDeVelde, J., Roswell, C.R., and Bowen, G.J., 2012, Dynamics of nitrate and chloride during storm events in agricultural catchments with different subsurface drainage intensity: Journal of Hydrology, v. 466, p. 1–10, https://doi.org/10.1016/j.jhydrol.2012.08.002.

Khrisat, H.T., and Al-Bakri, J., 2019, Assessment of groundwater vulnerability in Azraq catchment in Fuhais-Jordan using DRASTIC model: Open Journal of Geology, v. 9, p. 364–377, https://doi.org/10.4236/ojg.2019.97024.

King County, Washington, 2005, Executive's recommended regional infiltration control program: December, 278 p.

Kirlas, M.C., Karpouzos, D.K., Georgiou, P.E., and Theodossiou, N.A., 2023, A GIS-based comparative groundwater vulnerability assessment using modified-DRASTIC, environments: Environments, v. 10, 95, https://doi.org/10.3390/environments10060095.

Kirlas, M.C., Karpouzos, D.K., Georgiou, P.E., and Theodossiou, N., 2023, A GIS-based comparative groundwater vulnerability assessment using modified-DRASTIC, modified-SINTACS and NV index in a porous aquifer, Greece, in Gökçekuş, H., and Kassem, Y., eds., Climate change, natural resources and sustainable environmental management: Cham, Switzerland, Springer International Publishing, Environmental Earth Sciences, p. 330–338, https://doi.org/10.1007/978-3-031-04375-8_37.

Knudsen, K.L., Sowers, J.M., Witter, R.C., Wentworth, C.M., and Helley, E.J., 2000, Preliminary maps of Quaternary deposits and liquefaction susceptibility, nine-county San Francisco Bay Region, California: A digital database: U.S. Geological Survey Open-File Report 00-444, https://doi.org/10.3133/ofr00444.

Knüsel, B., Zumwald, M., Baumberger, C., Hadorn, G.H., Fischer, E.M., Bresch, D.N., and Knutti, R., 2019, Applying big data beyond small problems in climate research: Nature Climate Change, v. 9, no. 3, p. 196–202, https://doi.org/10.1038/s41558-019-0404-1.

Konhuaser, K., 2006, Introduction to microbiology: Hoboken, New Jersey, Wiley, 425 p.

LAO (Legislative Analyst's Office), 2020, What threat does sea-level rise pose to California?: The California Legislature's Nonpartisan Fiscal and Policy Advisor, August 10, 10 p.

Lebrato, M., Garbe-Schönberg, D., Müller, M.N., Blanco-Ameijeiras, S., Feely, R.A., Lorenzoni, L., Molinero, J.C., Bremer, K., Jones, D.O.B., Iglesias-Rodriguez, D., Greeley, D., Lamare, M.D., Paulmier, A., Graco, M., Cartes, J., Barcelos E Ramos, J., de Lara, A., Sanchez-Leal, R., Jimenez, P., Paparazzo, F.E., Hartman, S.E., Westernströer, U., Küter, M., Benavides, R., da Silva, A.F., Bell, S., Payne, C., Olafsdottir, S., Robinson, K., Jantunen, L.M., Korablev, A., Webster, R.J., Jones, E.M., Gilg, O., Bailly du Bois, P., Beldowski, J., Ashjian, C., Yahia, N.D., Twining, B., Chen, X.G., Tseng, L.C., Hwang, J.S., Dahms, H.U., and Oschlies, A., 2020, Global variability in seawater Mg and Sr ratios in the modern ocean: Proceedings of the National Academy of Sciences of the United States of America, v. 117, no. 36, p. 22281–22292, https://doi.org/10.1073/pnas.1918943117.

Levanon, E., Yechieli, Y., Gvirtzman, H., and Shalev, E., 2017, Tide-induced fluctuations of salinity and groundwater level in unconfined aquifers—Field measurements and numerical model: Journal of Hydrology, v. 551, p. 665–675, https://doi.org/10.1016/j.jhydrol.2017.05.044.

Lewis, M.A., Cheney, C.S., and Odochartaigh, B.E., 2006, Guide to permeability indices: UK Open Report, 29 p.

Lindström, R., 2005, Groundwater vulnerability assessment using process-based models [Ph.D. thesis]: Stockholm, Sweden, TRITA-LWR, 88 p.

Little, B., and Lee, J., 2009, Microbiologically influenced corrosion, in Kirk-Othmer encyclopedia of chemical technology: Hoboken, New Jersey, John Wiley & Sons, Inc., chapter 27, 38 p.

Liu, K-K., and Kao, S-J., 2007, A three end-member mixing model based on isotopic composition and elemental ratio: Terrestrial, Atmospheric and Oceanic Sciences, v. 18, no. 5, p. 1067–1075, https://doi.org/10.3319/TAO.2007.18.5.1067(Oc).

Lodwick, W.A., Monson, W., and Svoboda, L., 1990, Attribute error and sensitivity analysis of map operations in geographical information systems suitability analysis: International Journal of Geographical Information System, v. 44, p. 413–428, https://doi.org/10.1080/02693799008941556.

MCFCWCD (Marin County Flood Control and Water Conservation District), 2016, Coyote Creek Level evaluation project geotechnical data report: GEI Consultants, 657 p.

MRLC (Multi-Resolution Land Characteristics Consortium), 2024, Urban impervious data: Retrieved November 18, 2024.

Maal-Bared, R., Simpson, D., and Craik, C.S., 2016, Using biological activity reaction tests (BART) to monitor microbially-influenced corrosion in cast iron pipes [poster]: National Drinking Water and Wastewater Conference, Toronto, Ontario, Canada, Canadian Water and Wastewater Association.

Mackay, D.M., and Cherry, J.A., 1989, Groundwater contamination: Pump-and-treat remediation: Environmental Science & Technology, v. 23, no. 6, p. 630–636, https://doi.org/10.1021/es00064a001.

Malakootian, M., and Nozari, M., 2020, GIS-based DRASTIC and composite DRASTIC indices for assessing groundwater vulnerability in the Baghin aquifer, Kerman, Iran: Natural Hazards and Earth System Sciences, v. 20, p. 2351–2363, https://doi.org/10.5194/nhess-20-2351-2020.

Malings, C.A., 2017, Optimal sensor placement for infrastructure system monitoring using probabilistic graphical models and value of information [Ph.D. dissertation]: Pittsburgh, Pennsylvania, Carnegie Mellon University, 244 p.

Maqsoom, A., Aslam, B., Alwetaishi, M., Awais, M., Hassan, U., Maqsoom, S., Alaloul, W.S., Musarat, M.A., Zerouali, B., and Hussein, E.E., 2021, A GIS-based groundwater contamination assessment using modified DRASTIC geospatial technique: Water, v. 13, 2868, https://doi.org/10.3390/w13202868.

Margat, J., 1968, Vulnerabilité des nappes d'eau souterraine a la pollution [Groundwater vulnerability to contamination]; Bases Cartogr. (Doc.): Orléans, France, BRGM.

Marin County Flood Control and Water Conservation District (MCFCWCD), 2016, Coyote Creek Level evaluation project geotechnical data report: GEI Consultants, 657 p.

Mathany, T.M., Kulongoski, J.T., Ray, M.C., and Belitz, K., 2009, Groundwater-quality data in the South Coast Interior Basins study unit, 2008—Results from the California GAMA Program: U.S. Geological Survey Data Series Report 463, 82 p., https://doi.org/10.3133/ds463.

May, C.L., Mohan, A., Hoang, O., Mak, M., and Badet, Y., 2020, The response of the shallow groundwater layer and contaminants to sea level rise: Report by Silvestrum Climate Assoc. for the City of Alameda, California, 153 p.

May, K., Mohan, L., Plane, E., Ramrez-Lopez, D., Mak, D., Luchinsky, L., Hale, T., and Hill, K., 2022, Shallow groundwater response to sea-level rise: Alameda, Marin, San Francisco, and San Mateo Counties: San Francisco Estuary Institute (SFEI), 67 p.

McDonald, S.D., Nichols, D.R., Wright, N.A., and Atwater, B., 1978, Map showing thickness of young bay mud, southern San Francisco Bay, California: U.S. Geological Survey Miscellaneous Field Studies Map 976, scale 1:125,000.

McHarg, I.L., 1969, Design with nature: Garden City, New York, Natural History Press, 197 p.

McMillan, H., 2020, Linking hydrologic signatures to hydrologic processes: A review: Hydrological Processes, v. 34, p. 1393–1409, https://doi.org/10.1002/hyp.13632.

McMinn, R.M., 2017, Crawl space recovery, storm drains and standing water, Atchison Village flooding: Report to Atchison Village Mutual Homes Corporation, March 27, 13 p.

Miao, Z., Brusseau, M.L., Carroll, K.C., Carreón-Diazconti, C., and Johnson, B., 2012, Sulfate reduction in groundwater: Characterization and applications for remediation: Environmental Geochemistry and Health, v. 34, no. 4, p. 539–550, https://doi.org/10.1007/s10653-011-9423-1.

Michael, H.A., Post, V.E., Wilson, A.M., and Werner, A.D., 2017, Science, society, and the coastal groundwater squeeze: Water Resources Research, v. 53, p. 2610–2617, https://doi.org/10.1002/2017WR020851.

Moffett, K.B., Nardin, W., Silvestri, S., Wang, C., and Temmerman, S., 2015, Multiple stable states and catastrophic shifts in coastal wetlands: Progress, challenges, and opportunities in validating theory using remote sensing and field data: Remote Sensing, v. 7, no. 8, p. 10184–10226, https://doi.org/10.3390/rs70810184.

Mohr, T.K.G., 2007, Study of potential for groundwater contamination from past dry cleaner operations in Santa Clara County: San Jose, California, Santa Clara Valley Water District, 209 p.

Moran, M.J., Zogorski, J.S., and Squillace, P.J., 2007, Chlorinated solvents in groundwater of the United States: Environmental Science & Technology, v. 41, p. 74–81, https://doi.org/10.1021/es061553y.

Moran, M.J., 2006, Occurrence and implications of selected chlorinated solvents in ground water and source water in the United States and in drinking water in 12 Northeast and Mid-Atlantic States, 1993–2002: U.S. Geological Survey Scientific Investigations Report 2005–5268, 70 p.

Morgan, C.O., and Winner, M.D., 1962, Hydrochemical facies in the 400 foot and 600-foot sands of the Baton Rouge area, Louisiana: U.S. Geological Survey Professional Paper 450, p. 120–121.

Muyzer, G., and Stams, A., 2008, The ecology and biotechnology of sulphate-reducing bacteria: Nature Reviews Microbiology, v. 6, p. 441–454, https://doi.org/10.1038/nrmicro1892.

NOAA (National Oceanic and Atmospheric Administration), 2019, Tide elevation data: San Francisco, California.

NOAA (National Oceanic and Atmospheric Administration), 2024, Tide elevation data: Richmond, California (Chevron Tide Station), #9414863, retrieved September 1, 2024.

NOAA (National Oceanic and Atmospheric Administration), 2024, Tide elevation data: Sausalito, California, #9414806, retrieved September 1, 2024.

NRC (National Research Council), 1993, Ground water vulnerability assessment: Predicting relative contamination potential under conditions of uncertainty: Washington, D.C., National Academies Press, 210 p., https://doi.org/10.17226/2050.

Nerem, R.S., Chambers, D.P., Choe, C., and Mitchum, G.T., 2010, Estimating mean sea level change from the TOPEX and Jason altimeter missions: Marine Geodesy, v. 33, no. S1, p. 435–446, https://doi.org/10.1080/01490419.2010.491031.

OPC (California Ocean Protection Council), 2018, State of California sea-level rise guidance 2018 update: California Natural Resources Agency, 84 p.

OPC (California Ocean Protection Council), 2024, California sea level rise guidance: 2024 science and policy update: California Sea Level Rise Science Task Force, California Ocean Protection Council, California Ocean Science Trust, 101 p.

Oppenheimer, M., Glavovic, B.C., Hinkel, J., van de Wal, R., Magnan, A.K., Abd-Elgawad, A., Cai, R., CifuentesJara, M., DeConto, R.M., Ghosh, T., Hay, J., Isla, F., Marzeion, B., Meyssignac, B., and Sebesvari, Z., 2019, Sea level rise and implications for low-lying islands, coasts and communities, in Pörtner, H.-O., Roberts, D.C., Masson-Delmotte, V., Zhai, P., Tignor, M., Poloczanska, E., Mintenbeck, K., Alegría, A., Nicolai, M., Okem, A., Petzold, J., Rama, B., and Weyer, N.M., eds., IPCC special report on the ocean and cryosphere in a changing climate: Cambridge, UK and New York, Intergovernmental Panel on Climate Change (IPCC), Cambridge University Press, p. 321–445.

Parris, A., Bromirski, P., Burkett, V., Cayan, D., Culver, M., Hall, J., Horton, R., Knuuti, K., Moss, R., Obeysekera, J., Sallenger, A., and Weiss, J., 2012, Global sea level rise scenarios for the US national climate assessment: NOAA Technical Memo OAR CPO-1, 37 p.

Patel, P., Mehta, D., and Sharma, N., 2022, Calibration of the DRASTIC ground water vulnerability mapping method: Water Supply, v. 33, no. 5, p. 5190–5205, https://doi.org/10.2166/ws.2022.263.

Pierno, R., 1999, Appendix K: The DRASTIC spatial index of groundwater sensitivity, an analysis of the sensitivity to contamination of the Santa Clara Valley groundwater aquifers based on the USEPA DRASTIC methodology, in Mohr, T.K.G., 2007, Study of potential for groundwater contamination from past dry cleaner operations in Santa Clara County: San Jose, California, Santa Clara Valley Water District, p. 166–203.

Piper, A.M., 1944, A graphic procedure in the geochemical interpretation of water analyses: Transactions of the American Geophysical Union, v. 25, p. 914–923, https://doi.org/10.1029/TR025i006p00914.

Piscopo, G., 2001, Groundwater vulnerability map explanatory notes - Castlereagh Catchment: Parramatta, New South Wales, Australia, NSW Department of Land and Water Conservation, 16 p.

Plane, E., Hill, K., and May, C., 2019a, A rapid assessment method to identify potential groundwater flooding hotspots as sea levels rise in coastal cities: Water, v. 11, 2228, https://doi.org/10.3390/w11112228.

Plane, E., Hill, K., and May, K., 2019b, Minimum depth to groundwater for the coastal San Francisco Bay Area: Dataset 5606.

Plane, E., and Hill, K.Z., 2017, Minimum depth to groundwater for coastal Alameda County [Dataset]: Dryad Digital Repository.

Post, V.E., and Werner, A.D., 2017, Coastal aquifers: Scientific advances in the face of global environmental challenges: Journal of Hydrology, v. 551, p. 1–3, https://doi.org/10.1016/j.jhydrol.2017.05.021.

Postel, B., 2025, Personal communication regarding Atchison Village crawlspace flooding: April 22, 2025.

Rahman, A., 2008, A GIS based DRASTIC model for assessing groundwater vulnerability in shallow aquifer in Aligarh, India: Applied Geography, v. 28, p. 32–53, https://doi.org/10.1016/j.apgeog.2007.07.008.

Ralph, F.M., Rutz, J.J., Cordeira, J.M., Dettinger, M., Anderson, M., Reynolds, D., Schick, L.J., and Smallcomb, C., 2019, A scale to characterize the strength and impacts of atmospheric rivers: Bulletin of the American Meteorological Society, February, p. 269–289, https://doi.org/10.1175/BAMS-D-18-0023.1.

Ralph, F.M., Dettinger, M.D., Cairns, M.M., Galarneau, T.J., and Eylander, J., 2018, Defining "atmospheric river": How the Glossary of Meteorology helped resolve a debate: Bulletin of the American Meteorological Society, v. 99, no. 4, p. 837–839, https://doi.org/10.1175/BAMS-D-17-0157.1.

Ray, M.C., Kulongoski, J.T., and Belitz, K., 2009, Ground-water quality data in the San Francisco Bay study unit, 2007—Results from the California GAMA Program: U.S. Geological Survey Data Series 396, 92 p., https://doi.org/10.3133/ds396.

Ray, M.C., Kulongoski, J.T., and Belitz, K., 2013, Groundwater quality in the San Francisco Bay groundwater basins, California: U.S. Geological Survey Fact Sheet 2012-3111, 4 p.

Riis, C.E., Christensen, A.G., Hansen, M.H., and Husum, H., 2010, Vapor intrusion through sewer systems: Migration pathways of chlorinated solvents from groundwater to indoor air: Seventh Battelle International Conference on Remediation of Chlorinated and Recalcitrant Compounds, Monterey, California.

Rivett, M.O., Shepherd, K.A., Keeys, L., and Brennan, A.E., 2005, Chlorinated solvents in the Birmingham aquifer, UK: 1986–2001: Quarterly Journal of Engineering Geology and Hydrogeology, v. 38, p. 337–350, https://doi.org/10.1144/1470-9236/05-039.

Robinson, C., Li, L., and Barry, D.A., 2007, Effect of tidal forcing on a subterranean estuary: Advances in Water Resources, v. 30, no. 4, p. 851–865, https://doi.org/10.1016/j.advwatres.2006.07.006.

Roghani, M., Jacobs, O.P., Miller, A., Willett, E.J., Jacobs, J.A., Viteri, R.C., Shirazi, E., and Pennell, K.G., 2018, Occurrence of chlorinated volatile organic compounds (VOCs) in a sanitary sewer system: Implications for assessing vapor intrusion alternative pathways: Science of the Total Environment, v. 616–617, p. 1149–1162, https://doi.org/10.1016/j.scitotenv.2017.10.205.

Rosen, L., 1994, A study of the DRASTIC methodology with emphasis on Swedish conditions: Ground Water, v. 32, no. 2, p. 278–285, https://doi.org/10.1111/j.1745-6584.1994.tb00532.x.

Rotzoll, K., and Fletcher, C.H., 2012, Assessment of groundwater inundation as a consequence of sea-level rise: Nature Climate Change, v. 3, no. 5, p. 477–481, https://doi.org/10.1038/nclimate1725.

Rotzoll, K., and Fletcher, C.H., 2013, Assessment of groundwater inundation as a consequence of sea-level rise: Nature Climate Change, v. 3, p. 477–481, https://doi.org/10.1038/nclimate1725.

Rozell, D.J., 2020, Coastal resiliency groundwater considerations: Groundwater, v. 58, no. 6, p. 877–881, https://doi.org/10.1111/gwat.13043.

Rozell, D.J., 2021, Overestimating coastal urban resilience: The groundwater problem: Cities, v. 118, 103369, https://doi.org/10.1016/j.cities.2021.103369.

Rupert, M.G., 2001, Calibration of the DRASTIC ground water vulnerability mapping method: Ground Water, v. 39, no. 4, p. 625–630, https://doi.org/10.1111/j.1745-6584.2001.tb02350.x.

SFEI (San Francisco Estuary Institute), 2021, Sediment for survival: A strategy for the resilience of Bay wetlands in Lower San Francisco Estuary: April, 150 p.

SFEI (San Francisco Estuary Institute), 2019, SF Bay shoreline adaptation atlas, version 1.0: April, 262 p.

SFEI (San Francisco Estuary Institute), 2022, Depth to groundwater: Pathways Climate Institute & San Francisco Estuary Institute, retrieved April 1, 2025.

SFEI (San Francisco Estuary Institute), and SPUR, 2018, Operational landscape units for San Francisco Bay: Approach document: SWRCB Grant #16-051-120, 15 p.

Samara, T., and Yoxas, G., 2017, Drastic method to map groundwater vulnerability to pollution using nitrate measurements in agricultural areas: Bulletin of the Geological Society of Greece, v. 47, p. 981–991, https://doi.org/10.12681/bgsg.11138.

Schaumburg, F.D., 1990, Banning trichloroethylene: Responsible reaction or overkill?: Environmental Science & Technology, v. 24, no. 1, p. 17–22, https://doi.org/10.1021/es00071a002.

Schwarzenbach, R.P., Gschwend, P.M., and Imboden, D.M., 2016, Environmental organic chemistry (3rd ed.): Hoboken, New Jersey, John Wiley & Sons, 1024 p., https://doi.org/10.1002/0471649643.

Sener, E., and Davraz, A., 2013, Assessment of groundwater vulnerability based on a modified DRASTIC model, GIS and an analytic hierarchy process (AHP) method: The case of Egirdir Lake basin (Isparta, Turkey): Hydrogeology Journal, v. 21, p. 701–714, https://doi.org/10.1007/s10040-012-0947-y.

Senior, M.J., Shepley, J.G., Scheckenberger, R.B., and Schmidt, N., 2016, Lisgar District basement water infiltration investigation: Resilient Infrastructure, Canadian Society for Civil Engineering meeting, June 1–4, 2016, 11 p.

Sharp, J.M., Jr., Hansen, J.B., and Garcia-Fresca, B., 2010, Urban hydrology and the effects of anthropogenic activities in urban areas, in Ragone, S., ed., Groundwater in the urban environment: IAH International Contributions to Hydrogeology, Taylor and Francis, p. 295–308.

Shirazi, S.M., Imran, H.M., Akib, S., Yusop, Z., and Harun, Z.B., 2013, Groundwater vulnerability assessment in the Melaka State of Malaysia using DRASTIC and GIS techniques: Environmental Earth Sciences, v. 70, p. 2293–2304, https://doi.org/10.1007/s12665-013-2360-9.

Shirzaei, M., and Bürgmann, R., 2018, Global climate change and local land subsidence exacerbate inundation risk to the San Francisco Bay Area: Science Advances, v. 4, no. 3, eaap9234, https://doi.org/10.1126/sciadv.aap9234.

Singh, A., Srivastav, S.K., Kumar, S., and Chakrapani, G.J., 2015, A modified-DRASTIC model (DRASTICA) for assessment of groundwater vulnerability to pollution in an urbanized environment in Lucknow, India: Environmental Earth Sciences, v. 74, p. 5475–5490, https://doi.org/10.1007/s12665-015-4558-5.

Sloan, D., 1992, The Yerba Buena mud: Record of the last-interglacial predecessor of San Francisco Bay, California: Geological Society of America Bulletin, v. 104, no. 6, p. 716–727, https://doi.org/10.1130/0016-7606(1992)104

Sloan, D., 2006, Geology of the San Francisco Bay region: Berkeley, California, University of California Press, v. 79, 360 p.

Solinst Canada Ltd., 2022, 3001-User guide Levelogger series: April 18, 92 p.

Soylu, M., Bozdoganlio, U., and Dadaser-Celik, F., 2022, The use of modified Drastic method (DRASTIC-LU) for assessment of groundwater vulnerability to pollution at the Palas Basin/Turkey, in Gökçekuş, H., and Kassem, Y., eds., Climate change, natural resources and sustainable environmental management: Cham, Switzerland, Springer International Publishing, Environmental Earth Sciences, p. 330–338, https://doi.org/10.1007/978-3-031-04375-8_37.

Stevens, P.L., and Fort, C.L., 1996, The myth of measuring ground water, in WEFTEC '96, 69th annual conference and exposition: Dallas, Texas, Water Environment Federation, v. 2, 8 p.

Stoffer, P.W., and Gordon, L.C., eds., 2001, Geology and natural history of the San Francisco Bay Area: A field-trip guidebook: U.S. Geological Survey Bulletin 2188, 194 p., https://doi.org/10.3133/b2188.

Stoffer, P.W., 2002, Rocks and geology in the San Francisco Bay region: U.S. Geological Survey Bulletin 2195, 64 p., https://doi.org/10.3133/b2195.

Stuyfzand, P.J., 2008, Base exchange indices as indicators of salinization or freshening of (coastal) aquifers: 20th Salt Water Intrusion Meeting, p. 23–27.

Sweet, W.V., Hamlington, B.D., Kopp, R.E., Weaver, C.P., Barnard, P.L., Bekaert, D., Brooks, W., Craghan, M., Dusek, G., Frederikse, T., Garner, G., Genz, A.S., Krasting, J.P., Larour, E., Marcy, D., Marra, J.J., Obeysekera, J., Osler, M., Pendleton, M., Roman, D., Schmied, L., Veatch, W., White, K.D., and Zuzak, C., 2022, Global and regional sea level rise scenarios for the United States: Updated mean projections and extreme water level probabilities along U.S. coastlines: Silver Spring, Maryland, National Ocean Service, NOAA Technical Report NOS 01, 111 p.

Sweet, W.V., Kopp, R.E., Weaver, C.P., Obeysekera, J., Horton, R.M., Thieler, E.R., and Zervas, C., 2017, Global and regional sea level rise scenarios for the United States: NOAA Technical Report NOS CO-OPS 083, NOAA/NOS Center for Operational Oceanographic Products and Services, 75 p.

Taghavi, N., Niven, R.K., Paull, D.J., and Kramer, M., 2022, Groundwater vulnerability assessment: A review including new statistical and hybrid methods: Science of the Total Environment, v. 822, 153486, https://doi.org/10.1016/j.scitotenv.2022.153486.

Taherkhani, M., Vitousek, S., Barnard, P.L., Frazer, N., Anderson, T.R., and Fletcher, C.H., 2020, Sea-level rise exponentially increases flood frequency: Scientific Reports, v. 10, 6466, 17 p., https://doi.org/10.1038/s41598-020-63464-z.

Thompson, P.R., Widlansky, M.J., Leuliette, E., Chambers, D.P., Beckley, B., Sweet, W., Hamlington, B.D., Jevrejeva, S., Merrifield, M.A., Mitchum, G.T., and Nerem, R.S., 2024, Sea level variability and change [in "State of the Climate in 2023"]: Bulletin of the American Meteorological Society, v. 105, no. 8, p. S183–S186, https://doi.org/10.1175/2024BAMSStateoftheClimate.1.

Tien, I., Lozano, J-M., and Chavan, A., 2023, Locating real-time water level sensors in coastal communities to assess flood risk by optimizing across multiple objectives: Communications Earth & Environment, v. 4, 96, 12 p., https://doi.org/10.1038/s43247-023-00751-3.

Todd Engineers, and Kennedy/Jenks Consultants, 2010, Revised final groundwater vulnerability study; Santa Clara County, California: Santa Clara Valley Water District, 186 p.

Todd, D.K., and Mays, L.W., 2005, Groundwater hydrology (3rd ed.): New York, John Wiley, 656 p.

Todd, D.K., 1980, Groundwater hydrology (2nd ed.): New York, John Wiley, 535 p.

Trask, P.D., and Rolston, J.W., 1951, Engineering geology of San Francisco Bay, California: Bulletin of the Geological Society of America, v. 62, p. 1079–1110, https://doi.org/10.1130/0016-7606(1951)62[1079:EGOSFB]2.0.CO;2.

US EPA, 2019, Assessing and remediating low permeability geologic materials contaminated by petroleum hydrocarbons from leaking underground storage tanks: A literature review: Washington, D.C., Office of Underground Storage Tanks, 79 p.

US EPA, 2004, Hydraulic conductivity/transmissivity database for ground water flow and transport modeling: EPA/600/R-04/027, 80 p.

USACE (United States Army Corps of Engineers), 1984, San Francisco Bay tidal stage vs. frequency study: San Francisco, USACE, 58 p.

USACE (United States Army Corps of Engineers), 2024, San Francisco waterfront coastal flood study, CA, draft integrated feasibility report and environmental impact statement: USACE Tulsa District, The Port of San Francisco, P2:3499856, January, 252 p.

USGS, 2018, Saline water and salinity: Water Science School, June 11, 5 p.

Vengosh, A., Kloppmann, W., Marei, A., Livshitz, Y., Gutierrez, A., Banna, M., and Raanan, H., 2005, Sources of salinity and boron in the Gaza strip: Natural contaminant flow in the southern Mediterranean coastal aquifer: Water Resources Research, v. 41, no. 1, W01013, https://doi.org/10.1029/2004WR003344.

Volpe, A., Del Moro, G., Rossetti, S., Tandoi, V., and Lopez, A., 2007, Remediation of PCE-contaminated groundwater from an industrial site in southern Italy: A laboratory-scale study: Process Biochemistry, v. 42, p. 1498–1505, https://doi.org/10.1016/j.procbio.2007.07.017.

Voudouris, K., Kazakis, N., Polemio, M., and Kareklas, N., 2010, Assessment of intrinsic vulnerability using DRASTIC model and GIS in Kiti aquifer, Cyprus: European Water, v. 30, p. 13–24.

Wang, J., He, J., and Chen, H., 2012, Assessment of groundwater contamination risk using hazard quantification, a modified DRASTIC model and groundwater value, Beijing Plain, China: Science of the Total Environment, v. 432, p. 216–226, https://doi.org/10.1016/j.scitotenv.2012.06.005.

Wang, Z., Leung, M., Mukhopadhyay, S., Sunkara, S.V., Steinschneider, S., Herman, J., Abellera, M., Kucharski, and Ruggiero, P., 2025, Compound coastal flooding in San Francisco Bay under climate change: NPJ Nature Hazards, v. 2, 3, https://doi.org/10.1038/s44201-023-00003-8.

Weatherington-Rice, J., Christy, A.D., Angle, M.P., Gehring, R., and Aller, L., 2006b, DRASTIC hydrogeologic settings modified for fractured till: Part 2. Field observations: Ohio Journal of Science, v. 106, no. 2, p. 51–63.

Weatherington-Rice, J., Christy, A.D., Angle, M.P., and Aller, L., 2006a, DRASTIC hydrogeologic settings modified for fractured till: Part 1. Theory: Ohio Journal of Science, v. 106, no. 2, p. 45–50.

Werner, A.D., Bakker, M., Post, V.E., Vandenbohede, A., Lu, C., Ataie-Ashtiani, B., and Barry, D.A., 2013, Seawater intrusion processes, investigation and management: Recent advances and future challenges: Advances in Water Resources, v. 51, p. 3–26, https://doi.org/10.1016/j.advwatres.2012.03.004.

Werner, A.D., and Simmons, C.T., 2009, Impact of sea-level rise on sea water intrusion in coastal aquifers: Ground Water, v. 47, p. 197–204, https://doi.org/10.1111/j.1745-6584.2008.00535.x.

Yu, X., Yang, J., Graf, T., Koneshloo, M., O'Neal, M.A., and Michael, H.A., 2018, Impact of topography on groundwater salinization due to ocean surge inundation: Water Resources Research, v. 54, no. 10, p. 8121–8136, https://doi.org/10.1029/2018WR023322.hout, F.A., Henry, H.R., and Glover, R.E., 1964, Sea water in coastal aquifers: U.S. Government Printing Office, Water Supply Paper 1613-C, 84 p.